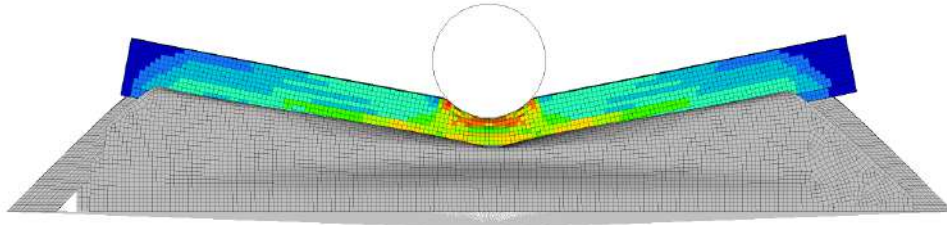




TÉCNICO
LISBOA



Preliminary design and analysis of a chassis side beam for stiffness and crashworthiness of an electric vehicle

José Luís Serra Pereira

Thesis to obtain the Master of Science Degree in

Aerospace Engineering

Supervisors: Prof. André Calado Marta
Eng. Luís Miguel Ouro Colaço

Examination Committee

Chairperson: Prof. Filipe Szolnoky Ramos Pinto Cunha
Supervisor: Prof. André Calado Marta
Member of the Committee: Aurélio Lima Araújo

November 2018

Acknowledgments

First, I want to thank my supervisors, engineer Luís Colaço and the professor André Marta. I am very grateful for all the knowledge they have shared with me, as well as the precious time they had spent to help me overcome these obstacles.

Thanks to CEiiA for this fantastic opportunity to be integrated into a work team with a challenging atmosphere, full of people always willing to help and share their knowledge.

To Técnico Lisboa, the school where I understood the meaning of hard work and the importance of excellency. But above all, thank you for giving me the opportunity to meet fantastic friends.

To my internship colleagues Pedro Santana, Rui Vilaça, Jorge Ramos and Henrique Oliveira for all help and motivation. I wish you the best.

To my friend Américo Fernandes, from the first day I started my university career, he always helped me.

To my best friends Samuel Cardoso, João Louro, Diogo Sanches and Luís Louro. They have always been there for me and bring out the best in me.

To my family, they support me in all the choices I make. To them, I owe everything.

Finally, to my girlfriend Ana Fernandes, her support and her friendship last for all these years. She gave me the strength and the happiness I needed overcome this challenge. Thank you for believing in me more than I do!

Resumo

Preocupações ambientais devido a carros de combustão interna estão a incentivar os construtores a construí-los elétricos. A maioria das baterias neste tipo de veículos são de ião-lítio, que em caso de derrame, pode causar ferimentos graves no passageiro. Considerando colisões laterais, que representam 15% a 40% de todos os acidentes com lesões, se apenas forem consideradas lesões graves e fatais, estes valores são aumentados em 50%.

Para proteger passageiros e baterias e também desenvolver um componente capaz de integrar um chassis, este trabalho foca-se no projeto preliminar e análise de uma viga lateral do chassis para rigidez e resistência ao impacto. Tendo em conta a função da viga, foi realizada uma escolha criteriosa da liga de alumínio que irá integrá-la. Dois modelos robustos de Análise de Elementos Finitos são construídos, um que testa o desempenho à colisão, e outro certifica se a viga tem a resistência e rigidez necessárias para integrar o chassis. Esses modelos são inseridos num programa otimizador multi-objectivo baseado em algoritmo genético. Este programa sujeito a restrições não-lineares, procura o melhor desempenho ao impacto com postes e a viga mais leve. Esta ferramenta permitirá obter a viga otimizada, sem perdas de tempo no processo iterativo de desenho e cálculo.

Neste programa adaptável a novas estruturas e aplicações, várias vigas com diferentes estratégias foram testadas. No final, uma viga multi-espessura com a secção transversal quadricular desalinhada foi escolhida. Esta solução supera vários requerimentos de projeto e apresenta o melhor compromisso entre peso e desempenho ao impacto com postes.

Palavras-chave: otimização multi-objectivo, algoritmo genético, desempenho ao impacto com postes, rigidez.

Abstract

Environmental concerns about internal combustion engine cars are pulling constructors to build them electric. The majority of the electric car power cells are lithium-ion batteries. In the event of battery leakage, lithium can cause serious injuries on the passengers' body. Regarding side collisions, that represent 15% to 40% from all injury accidents, if only serious and fatal injuries are considered these values are increased by 50%.

To protect passengers and batteries and also develop a component capable of integrating a chassis, this work focuses in the preliminary design and analysis of a chassis side beam for stiffness and crashworthiness. Taking into account the beam's function, a judicious choice of the aluminum alloy that will integrate it, was carried out. Two robust Finite Element Analysis (FEA) models are constructed, one that test the crash performance and another that certifies that the beam has the strength and stiffness enough to integrate the chassis. These models are inserted in a multi-objective optimization program based on a genetic algorithm. This program searches for the best pole crash performance and the lightest beam, subjected to non-linear constraints. This tool will allow to obtain the optimized beam without losing engineering time in the iterative process of design and calculate.

In this program, adaptive to new structures and purposes, several beams with different strategies were tested. Finally, a multi-thickness beam with a quadricular misaligned cross-sectional shape was chosen. This solution overcomes several project requirements and has the best commitment between pole crash performance and weight.

Keywords: multi-objective optimization, genetic algorithm, pole crash performance, stiffness.

Contents

Acknowledgments	iii
Resumo	v
Abstract	vii
List of Tables	xi
List of Figures	xiii
Nomenclature	xv
Glossary	xvii
1 Introduction	1
1.1 Motivation	1
1.2 CEiiA	2
1.3 Be2.0	2
1.4 Objectives	4
1.5 Thesis Outline	4
2 Background	7
2.1 Materials	7
2.2 Structural Principles	10
2.3 Crashworthiness Principles	10
2.4 Regulations	12
2.5 Material Model	15
2.5.1 Elastic Behavior	15
2.5.2 Plastic Behavior	16
2.6 Dynamic and Static Studies	17
2.7 Analysis Methods	17
2.7.1 Explicit Method	17
2.7.2 Implicit Method	18
2.8 Optimization Algorithm	19
2.8.1 Single-Objective Genetic Algorithm	20
2.8.2 Multi-Objective Genetic Algorithm	22

3	Implementation	27
3.1	Project Requirements	27
3.2	Structural Analyses	29
3.2.1	Bending Case	29
3.2.2	Torsional Case	29
3.3	Aluminum Alloy Choice	29
3.4	Optimization Cycle	31
3.4.1	<i>MATLAB</i> [®]	32
3.4.2	<i>CATIA</i> [™] V5	33
3.4.3	<i>HYPERMESH</i> [®] - Crash	34
3.4.4	<i>RADIOSS</i> [®]	41
3.4.5	<i>HYPERGRAPH</i> [®]	42
3.4.6	<i>HYPERMESH</i> [®] - Static	43
3.4.7	<i>OptiStruct</i> [®]	47
3.4.8	Output Analysis	48
3.4.9	Optimization Cycle Schematic	50
3.5	Mesh Convergence Study	51
3.5.1	Crash Simulation	51
3.5.2	Static Simulation	53
3.6	Alignment Tests at 75° and 90°	55
3.7	Effect of Auxiliary Structures	56
4	Experimental Study and Validation	59
4.1	Material Model	59
4.2	Crash Model	60
4.3	Static Model	62
5	Results	63
5.1	Optimization 1 - Rectangular Shape	63
5.2	Optimization 2 - Aligned Quadricular Shape	66
5.3	Optimization 3 - Misaligned Quadricular Shape	68
5.4	Optimization 4 - Aligned Quadricular Shape With First Width Division Thicker	71
5.5	Optimization 5 - Misaligned Quadricular Shape With First Width Division Thicker	74
5.6	Final Results	76
6	Conclusions	79
6.1	Deliverables and Achievements	79
6.2	Future Work	80
	Bibliography	81

A 6xxx Alloy Properties	85
B Initial Populations	87
C CAD Drawings	89

List of Tables

1.1	Vehicle classes [10]	3
2.1	Aluminum alloys [22]	9
2.2	Basic tempers (adapted from [22][24])	9
2.3	Five-stars safety ranking at 2018/2019 [38].	14
2.4	Side test performance limits	15
3.1	Aluminum alloy 6110A-T6 properties	31
3.2	Aluminum alloy 6061-T6 properties	36
3.3	Results from mesh convergence study (crash).	51
3.4	Results from mesh convergence study (static).	54
5.1	Parameters of optimization 1.	64
5.2	Parameters of optimization 2.	66
5.3	List of indexes.	68
5.4	Results from optimization 2.	68
5.5	Results from optimization 3.	70
5.6	Parameters of optimization 4.	72
5.7	Results from optimization 4.	73
5.8	Results from optimization 5.	75
A.1	6xxx alloy properties [24][62]	85
B.1	Initial population for optimization 2	87
B.2	Initial population for optimization 3	87
B.3	Initial population for optimization 4	87
B.4	Initial population for optimization 5	87

List of Figures

1.1	Electric vehicle chassis [5].	1
1.2	Be [9].	2
1.3	Electric cars chassis.	3
1.4	Be2.0 chassis.	3
2.1	Aluminum alloy extrusion [21].	8
2.2	Force vs displacement graph (adapted from [33])	11
2.3	UNECE lateral test (adapted from [34])	12
2.4	Impact reference line [37]	13
2.5	Pole side impact test [36]	14
2.6	Stress-strain curve of an illustrative ductile material (adapted from [44])	17
2.7	Optimization methods (adapted from [48])	19
2.8	Elite, crossover and mutation in genetic algorithms.[49]	21
2.9	Genetic algorithm example (adapted from [49])	22
2.10	Non-dominated front (adapted from [51])	22
2.11	Schematic process of single solution choosing (adapted from [51]).	23
2.12	Ranked individuals.	24
2.13	Cuboid (adapted from [51]).	24
2.14	<i>NSGA-II</i> algorithm schematic (adapted from [51]).	25
3.1	Be2.0's chassis with the structure highlighted.	27
3.2	Ultimate resilience vs tensile and shear yield strength	30
3.3	Optimization cycle	31
3.4	Parameterized beam	34
3.5	Imported geometry	35
3.6	Midsurface	35
3.7	Meshed geometry with 20mm element size	36
3.8	Pole	37
3.9	Rigid body	37
3.10	Contact <i>TYPE2</i>	38
3.11	Rigid body imposed velocity in <i>m/s</i>	39

3.12	Boundary conditions	39
3.13	Force-displacement curve	42
3.14	Displacement-time curve, from the rear end of the structure	42
3.15	Displacement-time curve 2, from the rear end of the beam	42
3.16	Filtered and unfiltered force-time curves	43
3.17	Imported beam geometry	44
3.18	Midsurface and mesh.	44
3.19	Rigid body.	45
3.20	Pressure applied to the beam.	46
3.21	Single point constrain with the applied moment.	46
3.22	Force-displacement curve	49
3.23	Optimization cycle schematic.	50
3.24	Structure front view	51
3.25	Curves from mesh convergence study (crash).	52
3.26	Time-element size curve.	52
3.27	Force-displacement curves for every element size.	53
3.28	Results from mesh convergence study.	53
3.29	Curves from mesh convergence study (static).	54
3.30	Result from 75° alignment test.	55
3.31	Result from 90° alignment test.	55
3.32	Force-displacement curves from the alignment test	56
3.33	Model without auxiliary structures.	56
3.34	Model with auxiliary structures.	56
3.35	Force-displacement curves for effect of auxiliary structures	57
4.1	Typical tensile specimen.	59
4.2	Universal hydraulic testing machine [60].	60
4.3	Render of the structure with the components outlined.	61
4.4	Experimental crash test layout.	61
5.1	Structure front view with a rectangular shape	63
5.2	Optimization 1 individuals and force - displacement curves.	64
5.3	Objective functions results.	65
5.4	Average distance between individuals at each generation.	65
5.5	Structure front view with 4 divisions in height and width.	66
5.6	Optimization 2 individuals and force - displacement curves.	67
5.7	Objective functions results from optimization 2.	67
5.8	Force-displacement curves from optimization 2 pareto front individuals.	68
5.9	Structure front view with 2 divisions in height and width.	69
5.10	Optimization 3 Individuals and force-displacement curves.	69

5.11 Objective functions results from optimization 3.	70
5.12 Force-displacement curves from optimization 3 pareto front individuals.	70
5.13 Quadricular shape beam with the thickness in the first width division different from the rest of the beam.	72
5.14 Force-displacement curves from optimization 4.	73
5.15 Objective functions results from optimization 4.	73
5.16 Force-displacement curves from optimization 4 pareto front individuals.	74
5.17 Force-displacement curves from optimization 5.	75
5.18 Objective functions results from optimization 5.	75
5.19 Force-displacement curves from optimization 5 pareto front individuals.	76
5.20 Final pareto front.	76
5.21 Displacements in Z direction - static test.	77
5.22 Force-displacement curve from the chosen beam.	78
5.23 Pole test results on the chosen beam.	78
5.24 Plastic strain with just the beam visible, in its traction zone.	78

Nomenclature

Greek symbols

Δt	Time step.
δ	Deformation.
$\dot{\epsilon}^{pl}$	Plastic strain rate.
$\dot{\epsilon}_0$	Reference plastic strain rate.
ϵ	Strain.
ϵ^{pl}	Plastic strain.
γ	Distortion.
ν	Poisson ratio.
Π	Potential energy.
ρ	Density.
σ	Stress.
σ_{eq}	Equivalent stress.
σ_y	Yield stress.

Roman symbols

a	Acceleration.
c	Material sound speed.
D	Rib deflection.
E	Elastic modulus.
F_{avg}	Average crash force.
F_{ext}	External forces.
F_{int}	Internal forces.

F_{max}	Crashing force.
G	Shear modulus.
g	Gravity acceleration.
I	Moment of inertia.
J	Torsional constant.
K_T	Tangent stiffness matrix.
L	Beam length.
l_c	Element critical length.
$m_{aux. components}$	Auxiliary components mass.
m_{beam}	Beam mass.
P	Pressure.
P_t	Current population.
Q_t	Child population.
r	Rank.
R_t	Extended population.
T	Temperature.
t	Time.
T_{melt}	Melt temperature.
T_{room}	Room temperature.
UTS	Ultimate tensile stress.
v	Velocity.
w	Beam width.

Glossary

AOP	Adult Occupant Protection.
CEN	Comité Européen de Normalisation.
CEiiA	Centre of Engineering and Product Development
CFC	Channel Frequency Class.
CFE	Crash Force Efficiency.
COP	Child Occupant Protection.
CPU	Central Processing Unit.
EA	Energy Absorption.
Euro NCAP	European New Car Assessment Programme
FEA	Finite Element Analysis
FEM	Finite Element Method
GA	Genetic Algorithm.
HIC	Head Injury Criterion.
HPC	Head Performance Criterion.
MOO	Multi-Objective Optimization.
RESS	Energy Storage Systems.
R&D	Research and Development
SA	Safety Assist.
SC	Single Point Constraint.
SEA	Specific Energy Absorption.
UNECE	United Nations Economic Commission for Europe.
VC	Viscous Criterion.
VRUP	Vulnerable Road User Protection.

Chapter 1

Introduction

1.1 Motivation

Internal combustion engine cars have been dominating for more than a century. However, environmental concerns about emissions are pulling traditional constructors and bringing new ones to build hybrid and electric cars. VOLVO announced that will only make electric and hybrid cars from 2019 onwards, becoming the first among the principal constructors [1]. Some countries have declared the banning of combustion car sales, like France where the prohibition will take place in 2040, or the bold Norway where this prohibition will be in 2025 [2].

With electric cars, new structural challenges will appear due to the batteries location or the new motor or motors locations. But, the chassis will continue to be the integrating part of the vehicle frame that supports internal and external loads [3].

The majority of the electric car power cells are lithium-ion batteries. Their protection is of the utmost importance because, like all alkali metals, lithium is highly reactive and flammable and can cause side effects on the passengers' body like skin lesions and others [4]. For batteries protection and occupants safety, the efforts are focused on crashworthiness with the inclusion of parts strategically placed to absorb the maximum energy from an impact. One of these parts is the side beam chassis where this work have their center of attention. The side beam chassis can be observed in the electric vehicle chassis from the figure 1.1.



Figure 1.1: Electric vehicle chassis [5].

The tests on the modeled beam will be based on Finite Element Method (FEM), a method that overcomes the traditional variational methods [6]. For implementing the FEM, in load and lateral crash situations, computational power is needed and the numerical software to do it was provided by CEiiA.

This thesis was conducted to obtain the Master of Science in Aerospace Engineering. Despite the study being focused in an electric vehicle, the work developed is of interest to both aeronautics and automotive areas. The development of energy absorbing structures, as light as possible to fulfill structural requirements, is a reality in the aeronautical industry, particularly in helicopters. Several aircraft and helicopters are already equipped with crash management systems and interesting studies in this field have been published [7][8]. The multi-optimization program developed in this work can be applied in the design and optimization of these aeronautical structures.

1.2 CEiiA

Created in 1999 with the objective of supporting the Portuguese automotive industry, CEiiA (Centre of Engineering and Product Development) is one of the 10 largest Research and Development (R&D) investors in Portugal. The current facilities in Matosinhos (Portugal) are prepared to operate in aeronautics, mobility, naval/offshore and automotive. CEiiA is present in 7 countries and employs more than 200 engineers. CEiiA works in connection with other organizations and people, with the goal of implementing technological solutions alongside its partners to push innovation forward [9].

1.3 Be2.0

This work is part of a larger project called Be2.0, a second version of the project Be as illustrated in figure 1.2. This is an on-demand vehicle for share use that can be driven by a human operator or autonomously. Powered 100% electric this car will be a M1 class vehicle with Portuguese engineering from universities and several other partner entities.



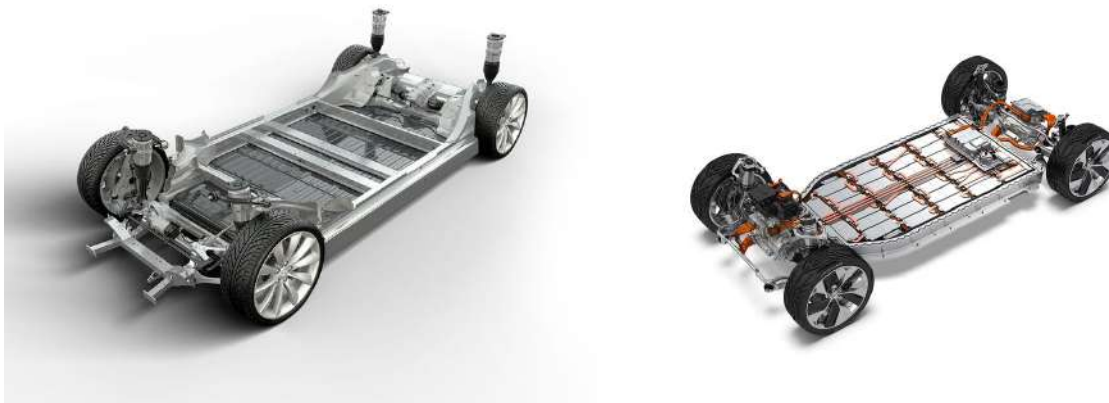
Figure 1.2: Be [9].

Based in United Nations Economic Commission for Europe (UNECE) standards, the vehicle classes are classified according to table 1.1. M1 class is a subdivision from the M class vehicles. This subdivision includes vehicles with no more than eight seats in addition to the driver seat.

Table 1.1: Vehicle classes [10]

Class	Description
M	Used for passengers carriage
N	Used for goods carriage
L	Motor vehicles with less than four wheels and some lightweight four-wheelers

The Be 2.0 follows the current strategy adopted by practically all electric car manufacturers of placing the batteries between axles and under the cabin, as exemplified in figure 1.3



(a) Tesla Model 3 chassis [11]

(b) Jaguar I-Pace chassis [12]

Figure 1.3: Electric cars chassis.

This strategy makes the side beam chassis a component with high requirements at structural level, because not only does it need to meet stiffness requirements but also to connect the rear and front modules of the car. Besides the structural requirements, this component must protect the batteries and occupants in case of lateral impact.

The current render of the Be2.0 chassis can be seen in figure 1.4.



Figure 1.4: Be2.0 chassis.

This type of chassis typology is recent and the studies related with the side beam chassis, in particular, are few and inaccessible, so it is an area where there is room for development.

1.4 Objectives

The goal of this work is to study a chassis element for a M1 class car vehicle that not only has the necessary characteristics for overall chassis performance (stiffness and resistance criteria), but also provides the necessary resistance in the event of a lateral pole impact, to protect battery and occupants.

This work focuses on the preliminary design and analysis of a chassis side beam to be applied in the Be2.0, an electric vehicle designed and engineered by CEiiA. This project will meet the following objectives:

- Due to the early stage development of this car, where several design constraints are assumed, it is important to create a design process that is suitable for future changes in project requirements or even for application in other vehicles;
- A numerical model to simulate as close as possible the European New Car Assessment Programme (Euro NCAP) pole test will be created. There are several project requirements related to the preparations, procedures and limits of this test;
- The aluminum alloy used in this project is another variable to be studied. The alloy must have the necessary characteristics to fulfill the projects requirements. In addition, it must have best structural and crash performance characteristics;
- This designed side beam must give its contribution to the performance of the overall torsional and bending stiffness of the chassis. In addition, it must fulfill its function by a safety margin even in the most demanding scenarios;
- To improve fuel consumption and safety of passengers and batteries, the designed beam should be the lightest and have the best performance in crash possible. Therefore, the optimization process must be multi-objective, in an effort to achieve a compromise between weight and crash pole performance.

1.5 Thesis Outline

In this first chapter the motivation behind the development of this optimization cycle and the main objectives of this thesis are explained. It is also approached the project and company in which this work is inserted.

Chapter 2 introduces some important studies to this work. Begins with a brief summary of aluminum and its alloys, then the structural and crashworthiness principles are explained as well as regulations and safety procedures regarding with cars side impact. Finally, a material model, dynamic and static studies, numerical methods and optimization algorithms are clarified.

Chapter 3 makes a detailed analysis of the project requirements, explains the structure analyze approach and perform the aluminum alloy choice. Then, makes a detailed explanation of the optimization cycle, contains the mesh convergence study and compares the differences between performing the test

with 90 or 75 degrees of alignment. Finally, a test with and without auxiliary structures is made to demonstrate the influence of these structures.

Chapter 4 discusses how the experimental tests should be performed to validate the material, crash and static models.

Chapter 5 demonstrates all the results of the multi-objective optimizations performed with the developed method. It compares and discusses the results and inputs of the method.

Finally, Chapter 6 summarizes the main achievements and deliverables of this thesis. Some suggestions for completing this work and for future developments in this area are explained here.

Chapter 2

Background

To start working on a solution for this project, it is fundamental to perform an intensive research about studies carried out in this area. First, a small introduction to the materials that could integrate the beam is made. Taking into account that the beam will be made of aluminum, a more detailed description about its characteristics and classification is made. The structural principles, used to evaluate if the beam has the necessary characteristics to integrate the chassis and the crashworthiness principles to evaluate the beams in crash performance are explained. Then, regulations related to side crash safety tests are clarified and the material model used is described. A brief summary about static and dynamic studies, implicit and explicit methods is performed. Finally a detail explanation regarding the genetic algorithms is covered in this chapter.

2.1 Materials

In this section we will make a small overview about potential materials that could integrate the side beam chassis. But, according to the project requirements, the beam will be made of an aluminum alloy. A more detailed explanation about this material will be given.

Traditionally, if the objective is to design a chassis component, the most common material for body structures is steel. However, nowadays aluminum, magnesium alloys, plastics and polymer composites need to be considered in automotive industry.

Steel has a lot of advantages: versatility, low cost, stable supply, high formability, high impact resistance, wide hardening ability, assembling simplicity, well-developed repair and maintenance technology. On other hand, corrosion susceptibility and its low strength-to-weight ratio represent the main disadvantages of steel body construction [13][14].

The production of a magnesium structure of a target stiffness requires less 60% and 20% of mass when compared to a steel or aluminum structure respectively. Despite its high strength-to-weight ratio, the magnesium major problem lies on the difficulty to produce extrusions or sheet plates, which makes them unattractive for mass production. This is why manufactures only use around 5kg of magnesium in a normal modern vehicle. This mass is usually applied in thin-walled cast parts [13][14].

In a modern vehicle, 50% of its volume is composed by plastic and polymer composites, however it only represents 8% of the vehicle's mass. It is unusual for thermoplastics to incorporate chassis components due to its low elastic modulus (3GPa) and low strength. Carbon fiber reinforced polymer composites can integrate a car chassis, but due to their high cost, they are only used in luxury cars or in car competition. In addition, carbon fiber is not easily recyclable and composites have a long production cycle time. Besides these disadvantages, composite materials present another problem related with crash safety, namely the prediction of fragment distribution and retaining of segregated parts after impact [13][14].

Over the 19th century, aluminum was rarer and more valuable than gold, extracting it from ore was very difficult and until half of the 20th century, it was rarely used in automotive industries. Since 1975, its application in this industry has been growing at an annual rate of 4% [13][14][15]. Today, an average of 10% of all cars weight is composed by aluminum, however 80% is used in the cast parts. Due to environmental issues and weight saving, the automotive structural components market is moving from steel to aluminum alloys. This does not sacrifice vehicle safety or performance and reduces the car's body weight by about 40 to 47% [16][17][18][19].

Due to aluminum alloy's strength-to-weight ratio the body car can be almost 2 times lighter than a regular steel one, but normally ends up with thicker panels. Recycling is not a problem, and thanks to its inert aluminum oxide film over the surface, aluminum performs a high corrosion resistance, a characteristic that normal steel does not present [20] [13].



Figure 2.1: Aluminum alloy extrusion [21].

The aluminum resistance to electrical current increases the difficulty of spot weld, therefore, fastened and riveted joints are the normal solution in aluminum structures. But the major problem is the cost per unit mass that can be twice the price of steel. When it comes to an aluminum-intensive vehicle, it can cost 1 to 4 American dollars per kilogram more [14].

Aluminum alloys give a wide range of options in mechanical properties with approximately 500 international registered wrought and cast aluminum alloys compositions [22]. With so many alloys, its classification is fundamental, and according to Comité Européen de Normalisation (CEN), the aluminum alloys are divided into two main groups: wrought alloys and cast alloys. To distinguish the two main groups, before the numerical code, appear 4 letters. The first two, EN, represent the European standard, the third letter is an A for aluminum, and the fourth can be a W or a C: W for wrought group and C for Cast group.

The wrought aluminum alloys are mainly used to produce rolled plates or extrusions. Their classifi-

cation is based on a 4 number code in which the first digit represents the series and the major alloying element, with the exception of the 1xxx series. This series designates the unalloyed composition or pure aluminum, where the percentage of aluminum represents more than 99% of all material.

The Cast alloy group is composed by the alloys produced by solidification of the molten alloy in a mold. Instead of a 4 number code, this group is classified by a 5-number code, or, as an alternative form, based on the chemical symbols [22].

Inside of each main group, the different series can be grouped in different ways, like the heat treatable and the non-heat-treatable alloys. The heat treatable ones can be strengthened by a thermal treatment like the precipitation hardening, opposed to the non-heat treatable ones, which does not allow it [23].

Some details about aluminum alloys classification can be consulted in table 2.1.

Table 2.1: Aluminum alloys [22]

	Series	Major Alloying Element	Work Hardening	Precipitation Hardening	Solution Hardening	
Wrought Alloys	1xxx	-				
	3xxx	Mn				non-heat treatable
	4xxx	Si	X		X	
	5xxx	Mg				
	2xxx	Cu				
	6xxx	Mg + Si				heat treatable
	7xxx	Zn		X	X	
	8xxx	Others				
	9xxx	unused				
Casting Alloys	4xxxx	Si			X	non-heat treatable
	5xxxx	Mg				
	2xxxx	Cu		X	X	heat treatable
	7xxxx	Zn		X		

Also the tempers have their own designation, that consists of an individual capital letter followed by digits, which indicates the temper sub-divisions. The basic tempers can be consulted in table 2.2.

Table 2.2: Basic tempers (adapted from [22][24])

Temper	Designation
F	As-Fabricated
O	Annealed
H	Strain-Hardened
W	Solution Heat-Treated
T	Thermally Treated

The appropriate selection of the aluminum alloy will be made in the section 3.3, following the project requirements.

2.2 Structural Principles

To evaluate if the beam has the necessary structural characteristics to integrate a car chassis, several indicators are used. Allowable stress, torsional and bending stiffness are the most used structural principles to evaluate a chassis component.

Being the aluminum alloys a ductile material, the Von Mises criterion interprets well the material yielding [25]. This criterion computes the equivalent stress as

$$\sigma_{eq} = \sqrt{\frac{(\sigma_1 - \sigma_2)^2 + (\sigma_2 - \sigma_3)^2 + (\sigma_1 - \sigma_3)^2}{2}}, \quad (2.1)$$

where σ_1 , σ_2 and σ_3 are the principal stresses. The yielding stress represented by σ_y is the point where the plastic deformation appears in the material. When σ_{eq} reaches the yielding stress the material starts to yield.

To maintain the structural integrity of the beam and security of the passengers, a 1.5 safety factor is normally used. This means, that in the worst load condition, the equivalent stress should not exceed $2/3$ of the yield stress [26],

$$\sigma_{eq} \leq \frac{\sigma_y}{1.5}. \quad (2.2)$$

A chassis beam can be sufficiently strong but not sufficiently rigid. Limits of deflection and twist of the side beam chassis are very important to prevent problems in the response performance. The simple operation of closing and opening the door can be compromised if the side beam chassis is not rigid enough, or even can cause passenger insecurity if the car's floor is deflecting [26].

The rigidity of a beam is evaluated by the bending and torsional stiffness. The beam bending stiffness, or flexural rigidity, is the resistance against bending and can be evaluated by the product of the elastic modulus E by the moment of inertia I [6]. Torsional stiffness is the resistance to twist and can be evaluated by the product of the shear modulus G by the torsional constant J [27]. The relation between bending and twisting are computed by the Timoshenko beam theory, that can be consulted in Hughes et al. [28].

2.3 Crashworthiness Principles

To compare different beams and evaluate their crashworthiness performance, some indicators are used. The most common principles to evaluate crashworthiness are the energy absorption (EA), the average crash force (F_{avg}), the specific energy absorption (SEA), the peak crashing force (F_{max}) and the crash force efficiency (CFE) [29] [30] [31] [32].

The energy absorption is defined by

$$EA = \int_0^{\delta} F(x)dx, \quad (2.3)$$

where $F(x)$ is the crash force and δ is the deformation. From which the average crash force can be found as

$$F_{avg} = \frac{EA}{\delta}, \quad (2.4)$$

and the specific energy absorption as

$$SEA = \frac{EA}{m}, \quad (2.5)$$

where m represent the mass of the beam. On the other hand, the peak crashing force is found from

$$F_{max} = Max(F(x)) \quad (2.6)$$

and the crash force efficiency is defined as

$$CFE = \frac{F_{avg}}{F_{max}}. \quad (2.7)$$

In crashworthiness performance, a high value of energy absorption with a low peak of force is desired, in other words, the goal is to absorb the maximum kinetic energy while maintaining a constant acceleration. High accelerations are registered in the peaks of force and this can be dangerous to the vehicle's passengers.

A major concern regarding electric vehicles is their weight. Therefore, saving mass in all parts is an objective. Taking into account the goal of having structures capable of absorbing as much energy as possible, what we really want is to maximize the specific energy absorption. To maintain high values of SEA, dealing with high forces of impact is inevitable, but as mentioned before, dealing with peaks of force can be harmful. Therefore, the stability of all crash events needs to be guaranteed. This is evaluated by the CFE that needs to be as close to unit as possible.

In figure 2.2, the blue curve represents a bad energy absorption component, with a high peak force, instability and low energy absorption. On the other hand, the red curve represents the goal in crashworthiness performance, force in all crash event close to the peak and the area below the curve maximized, representing the energy absorption.

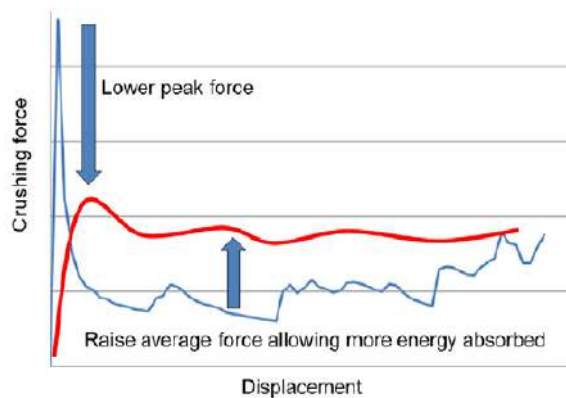


Figure 2.2: Force vs displacement graph (adapted from [33])

2.4 Regulations

The side beam chassis is the focus of this work, as such the lateral impact is approached in this section with more detail. Despite side collisions represent 15% to 40% from all injury accidents, if only serious and fatal injuries are considered, these values are increased by 50% [26].

Before putting a car on the road, the car manufactures need to fulfill the government's impact testing requirements, to get the vehicle's homologation. UNECE is the regulation entity responsible for these tests in Europe.

The lateral test consists in a forced collision between the car, initially immobilized, and a mobile deformable barrier with $950 \pm 20\text{kg}$ as can be observed in figure 2.3. It is mandatory that the mobile deformable barrier collide with the car at speed of $50 \pm 1\text{km/h}$. The barrier shall not impact with the vehicle a second time. The importance of this test is to evaluate if the passenger compartment has rigidity enough to protect the occupants from intrusion and if the lateral under floor cross member, plus the passenger compartment, absorb sufficient energy to fulfill the safety requirements.

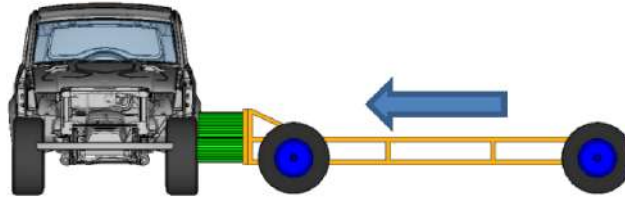


Figure 2.3: UNECE lateral test (adapted from [34])

The majority of the requirements are based on the protection of the more sensible human body parts like head, thorax, pelvis and abdomen. However, structural requirements are also imposed, and if we are dealing with an electric car, which is the case, additional ones related with the battery protection are analyzed.

The head performance criterion (HPC) is obtained by calculating the maximum value of

$$HPC = (t_2 - t_1) \left(\frac{1}{t_2 - t_1} \int_{t_1}^{t_2} (a) dt \right)^{2.5}, \quad (2.8)$$

where t_1 and t_2 are any two times between the initial and the final contact and a the resultant acceleration expressed as a multiple of g . The value of HPC to fulfill the requirements must not exceed 1000. The thorax performance criterion can be divided in two, the chest deflection that measures the maximum deflection on any rib, and the viscous criterion (VC) that evaluate the peak viscoses response. The viscous criterion can be calculated as

$$VC = \max \left(\frac{D}{0.14} \frac{dD}{dt} \right) \quad (2.9)$$

where D represents the rib deflection. When it comes to abdomen safety, the abdomen protection criterion imposes an abdominal peak force less or equal to 2.5kN. Looking at pelvis protection the maximum

peak force shall not overcome 6kN. Other requirements related with the structure are examined during the side impact test. Extracting the dummy from the protective system and from the vehicle shall be possible without using tools. As well as, after the impact, a minimum number of doors shall continue to operate for a normal entry and exit of the occupants. It is imperative that the doors during the test remain closed. If the car is electrical, the vehicle needs to fulfill additional requirements, one of the most important is the protection against electrical shock. In the event of an electrolyte spillage during a period of 30 minutes, just 7% of the electrolyte from the rechargeable energy storage systems (RESS) can be spilled, but never into the passenger's compartment. During the impact test, any part of the RESS shall not entry into the passenger's compartment and if it is located inside of the passenger's compartment, it shall remain in the same position. More details about all the procedure of the lateral impact test can be found in the ECE-R95 regulation [35].

Like UNECE, Euro NCAP performs crash tests, not to achieve vehicle's homologation but to help customers identifying the safest choice. The Euro NCAP is an independent association that performs more demanding tests like the side impact pole test. This test allows to simulate the event of the vehicle's lost control by the driver, followed by impact sideways into rigid roadside objects such as trees or poles [36]. This severe test consists of a sideways projected car against a rigid pole with a dummy placed in the driver's seat. Due to the localized impact, the pole intrusion in the car can be high and can cause serious injuries to the driver.

This test is carried out with great precision and the mass transported by the vehicle is controlled, so the car should impact the pole with:

- All the fluids must be at is maximum level;
- A luggage equal to 68 kg times the rated number of occupants on the luggage compartment;
- Sparing wheel and tools (if not compromised the crash performance of the car);
- A 75kg dummy placed in the drivers seat.

The car must impact the pole in the Impact Reference Line, that results from the intersection of the vehicle's exterior surface and a vertical plane, constructed by the passage through the head's dummy center of gravity and the intersection at 75° with the vehicle's longitudinal centerline, as illustrated in figure2.4.

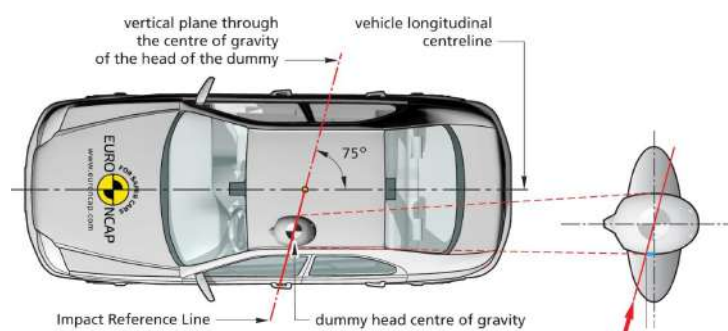


Figure 2.4: Impact reference line [37]

The pole is a circular metallic rigid structure with $254\pm 3\text{mm}$ in diameter. It begins at a maximum of 102mm above the lowest point of the tires, and it ends at least 100mm above the highest point of the vehicle. The carrier that transports the car is a flat plate that must have sufficient area to permit the rotation and a longitudinal displacement of 1000mm, unobstructed. To prevent friction between tires and carrier, a sheet of polychlorotrifluoroethylene is placed under the tires. An example is shown in figure 2.5



Figure 2.5: Pole side impact test [36]

The impact must occur with a target speed of $32\pm 0.5\text{km/h}$, that must be reached 10m before the contact and achieved with an acceleration lower than 1.5m/s^2 . The alignment of the car when the contact occurs must be such that:

- The vehicle motion forms an angle of $75\pm 3^\circ$ with the vehicle longitudinal centerline;
- The impact reference line shall be aligned with the centerline of the rigid pole surface.

The 75kg dummy must be a WorldSID 50th percentile male test dummy placed and highly instrumented according to the Euro NCAP Oblique Pole Side Impact Testing Protocol [37], where more detailed information about the whole test protocol can be found.

The five-stars safety ranking was created by Euro NCAP where 5 stars represent overall very good performance in crash protection and 1 star represent marginal crash protection [38]. The five-stars safety ranking at 2018/2019 is computed as explained in table 2.3.

Table 2.3: Five-stars safety ranking at 2018/2019 [38].

	AOP	COP	VRUP	SA	Overall
For five stars, at least:	80%	80%	60%	70%	74%
For four stars, at least:	70%	70%	50%	60%	64%
For three stars, at least:	60%	60%	40%	50%	54%
For two stars, at least:	50%	50%	30%	40%	44%
For one star, at least:	40%	40%	20%	30%	34%
Weight	40%	20%	20%	20%	

In 2018, according to the Euro NCAP Rating Review [38], in the 5 star ranking, all tests are rated by summing 148 points divided in 4 categories:

- 38 points to Adult Occupant Protection (AOP);
- 49 points to Child Occupant Protection (COP);
- 48 points to Vulnerable Road User Protection (VRUP);
- 13 points to Safety Assist (SA).

The side pole test is included in the 38 points of Adult Occupant Protection. This test represents 8 points that are divided into 4 individual body regions, head, chest, abdomen and pelvis, as summarized in table 2.4, where HIC_{15} is the Head Injury Criterion that is calculated in the same way as HPC but just in 15ms. The Peak Resultant Acc is the acceleration measured in multiples of the gravity acceleration. Exceeding a capping limit leads to loss of all points related to the tests.

Table 2.4: Side test performance limits

	Higher Performance limit	Lower Performance Limit	Capping Limit
Head	-	-	$HIC_{15} < 700$ Peak Resultant Acc $< 80G$ No direct head contact whit the pole
Chest	Rib Lateral Compression 28mm	Rib Lateral Compression 50mm	Rib Lateral Compression 55mm
Abdomen	Lateral Compression 47mm	Lateral Compression 65mm	-
Pelvis	Pubic Symphysis Force 1.7kN	Pubic Symphysis Force 2.8kN	-

Other special limits are applied, like on the shoulder, where the lateral force applied cannot be higher than 3kN or no points will be awarded for the chest assessment. The same approach is done for chest and abdomen, where if the viscous criterion is higher than 1.0m/s no points will be awarded. A door opening during the test scores -1 point for every door that opens. If the car is not equipped with head protection systems, the pole test is not performed and gets zero points [39].

2.5 Material Model

As mentioned before, the side beam chassis needs to overcome not only structural but also crashworthiness requirements. In the structural analysis, the material elastic behavior is sufficient to design and test it. In the crash analysis, the plastic behavior is fundamental because only with high deformations can we reach high absorbed energies from the impact.

2.5.1 Elastic Behavior

According to Beer et al. [40], the elastic behavior of a material can be described by the Hook' Law,

$$\sigma = E\epsilon, \quad (2.10)$$

where σ is the stress, E is the elastic modulus and ϵ is the strain. This law is represented by the stress-strain linear zone in figure 2.6. For 3D problems, homogeneous and isotropic materials the 3D

generalized Hook's Law describes the elastic material behavior as

$$\begin{bmatrix} \varepsilon_{xx} \\ \varepsilon_{yy} \\ \varepsilon_{zz} \\ \gamma_{xy} \\ \gamma_{yz} \\ \gamma_{xz} \end{bmatrix} = \begin{bmatrix} \frac{1}{E} & -\frac{\nu}{E} & -\frac{\nu}{E} & 0 & 0 & 0 \\ -\frac{\nu}{E} & \frac{1}{E} & -\frac{\nu}{E} & 0 & 0 & 0 \\ -\frac{\nu}{E} & -\frac{\nu}{E} & \frac{1}{E} & 0 & 0 & 0 \\ 0 & 0 & 0 & \frac{1}{G} & 0 & 0 \\ 0 & 0 & 0 & 0 & \frac{1}{G} & 0 \\ 0 & 0 & 0 & 0 & 0 & \frac{1}{G} \end{bmatrix} \begin{bmatrix} \sigma_{xx} \\ \sigma_{yy} \\ \sigma_{zz} \\ \sigma_{xy} \\ \sigma_{yz} \\ \sigma_{xz} \end{bmatrix}, \quad (2.11)$$

where γ is the distortion. The Poisson ratio ν and the shear modulus G can be related as

$$G = \frac{E}{2(1 + \nu)}. \quad (2.12)$$

2.5.2 Plastic Behavior

The Johnson-Cook equation is a validated and very popular constitutive model to describe the material behavior under a high rate deformation processes,

$$\sigma = \left[A + B (\epsilon^{pl})^n \right] \left[1 + C \ln \left(\frac{\dot{\epsilon}^{pl}}{\dot{\epsilon}_0} \right) \right] \left[1 - \left(\frac{T - T_{room}}{T_{melt} - T_{room}} \right)^m \right], \quad (2.13)$$

where σ and ϵ^{pl} are the stress and plastic strain respectively; A , B , C , n and m are constants that are characteristics of the material; T , T_{room} and T_{melt} stands for the current, room and melt temperature respectively. The ratio $\frac{\dot{\epsilon}^{pl}}{\dot{\epsilon}_0}$ is the normalized plastic strain rate, where $\dot{\epsilon}^{pl}$ is the plastic strain rate and $\dot{\epsilon}_0$ is the reference plastic strain rate usually equal to $1s^{-1}$ [41][42][43].

The Johnson-Cook equation (2.13) contains three terms. The relationship between the stress and the plastic strain in the first term, the relationship between the stress and the plastic strain rate in the second term, and the third term connects the stress with temperature during the plastic deformation.

For crash situations, this model can be simplified. The relationship between the stress and the plastic strain rate as well as the temperature influence on the materials behavior can be neglected. The influence of the relationship between stress and the plastic strain rate is only significant in deformations that are only observed in ballistic impacts, which is not the case. The temperature during the crash situation will be much smaller than the melting temperature, therefore the temperature dependence can be neglected [32]. In conclusion, the model can be expressed in a simpler form,

$$\sigma = A + B (\epsilon^{pl})^n. \quad (2.14)$$

Figure 2.6 represent an illustrative ductile material where the curve until the yield stress (elastic region) can be plotted according the Hook's Law and after it according to the Johnson-Cook equation (2.13).

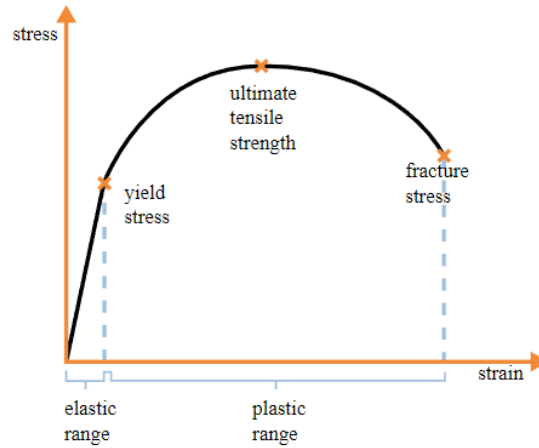


Figure 2.6: Stress-strain curve of an illustrative ductile material (adapted from [44])

2.6 Dynamic and Static Studies

Dynamic and static analyses will be both considered in this work, but in different contexts. Static analysis is applied when the structure is in equilibrium of moments and forces, or when the load is applied slowly (quasi-static) where the inertial effect can be neglected [45]. Dynamic analysis is applied when the inertial effect can't be neglected or it is excited by dynamic loads to produce time varying responses such as: displacements, accelerations and velocities.

It is obvious that in the crashworthiness analysis just the dynamic study is applicable, because involves high velocities where the inertia of the vehicle cannot be neglected.

At first glance, like for crashworthiness, what would make sense would be perform a dynamic structural analysis. A car is subject to higher loads not when it is immobilized (static), but when it is subject to dynamic loads during its operation, like passing through a road hole, climbing a side-walk, etc. But this dynamic study can be simplified into a static one by means of dynamic factors, explained in detail in section 3.2.

2.7 Analysis Methods

Explicit and implicit methods are different solvers that are applied according to the type of analysis being performed.

2.7.1 Explicit Method

An explicit algorithm is suitable to compute dynamic simulations. But for static or quasi-static ones, it cannot solve it as easily because the solution is obtained by integrating directly the equation of motion in a step by step method. Explicit solvers are suitable to solve problems with short events (milliseconds),

large deformations or with a complex number of contacts [46].

When it comes to short events, like crash, the explicit method is computationally inexpensive because it does not require any matrix inversion as happens with the implicit method. According to Atair University [47] and Nunes [32], the explicit method can be explained as follows:

It starts from the second law of Newton to compute the acceleration as

$$\ddot{x}_n = \frac{F_{ext}(t_n) - F_{int}(t_n)}{m}, \quad (2.15)$$

where F_{ext} and F_{int} are external and internal forces respectively. And integrates once to obtain the velocity

$$\dot{x}_{n+\frac{1}{2}} = \dot{x}_{n-\frac{1}{2}} + \ddot{x}_n \Delta t, \quad (2.16)$$

and twice to obtain and the displacement,

$$x_{n+1} = x_n + \dot{x}_{n+\frac{1}{2}} \Delta t, \quad (2.17)$$

and restarts the process in the new position $n + 1$. This cycle is applied to all nodes of the model.

To guaranty the stability of the method, the time step must be small enough to excite all frequencies in the finite element mesh,

$$\Delta t \leq \frac{l_c}{c}, \quad (2.18)$$

where l_c is the critical length of the element and c is the speed of sound in the material [47]. This condition imposes that the smaller the element size, smaller the time-step. Therefore, a compromise between computation time and precision of the results must be found. If the elements are very large, the results may not be viable. However, having very small elements means having more elements to be calculated with a smaller time step and this leads to a higher computational time. This can be a problem when we are dealing with large models.

2.7.2 Implicit Method

For static or quasi-static problems like sheet metal forming , gravity loading, initial or before/after dynamic simulations, the implicit method is the advisable. Although having a relatively high cost per loading step, due to stiffness matrix inversion, this method is always stable.

Opposite to the explicit algorithm that obtain the next value knowing the previous one, the implicit algorithm assumes the solution and solve the equations simultaneously.

Minimizing the potential energy Π and viewing the problem for stable equilibrium we have,

$$\delta\Pi = \Pi_n(X + \delta X) - \Pi_0(X) = 0, \quad (2.19)$$

where X represent the displacement and n and 0 are the initial and final configurations respectively. The

truncated Taylor series implies

$$K_T \delta X = F_{ext}(X) - F_{int}(X). \quad (2.20)$$

For stability the tangent stiffness matrix K_T should be positive definite.

Despite of not advisable, this method can handle non-linear problems, but the solution needs to be corrected and incremented by the Newton-Raphson method or a modified variant of it [46].

2.8 Optimization Algorithm

There are several optimization methods as demonstrated in figure 2.7. All of them can be divided into two major branches, the deterministic and heuristic ones. The most commonly used methods are the genetic algorithms and the gradient-based ones [48].

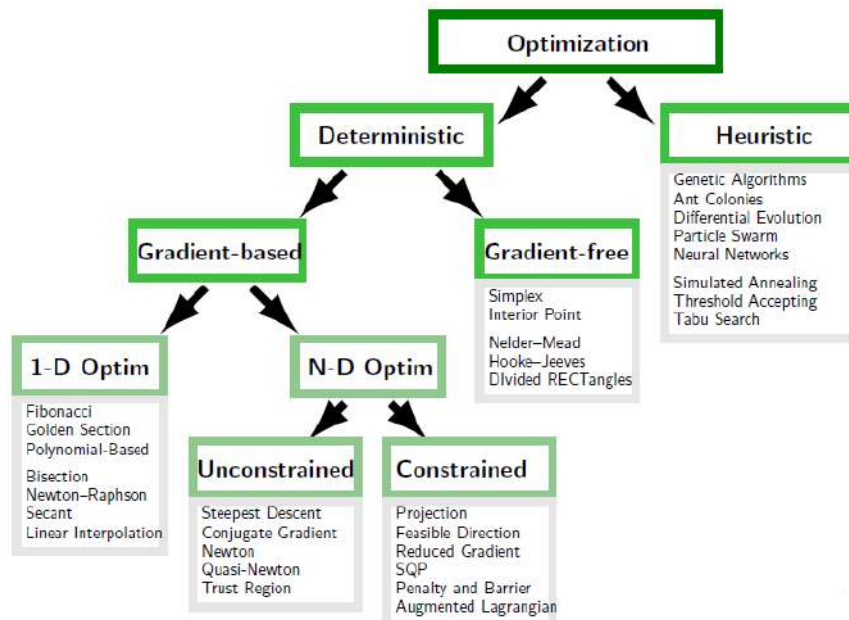


Figure 2.7: Optimization methods (adapted from [48])

The gradient-based optimization algorithms are the most suitable for a large number of design variables. Practically all gradient-based optimizers use finite difference for the gradient calculation. Along with the Hessian matrix, the gradient defines the optimum point. The necessary conditions for a local minimum are the Hessian matrix be positive semi-definite, and the gradient be equal to zero. This is very important because in a non-convex problem with multiple local minima, the solution obtained by gradient methods will be the local minimum nearest to the starting point. This problem of being "stuck" in local minima and not reach the global one can be overcome by giving several starting points along the search area, but doing so, it is necessary to make as many optimizations as starting points. This strategy is not feasible for situations where the computing time of each iteration is large, as in this work.

Another problem related to these algorithms is the assumption that the objective and constraints are smooth functions, which might not be the case [48].

Based on the theory of biological natural selection, the Genetic Algorithm (GA) is a method that search for a global minimum and is excellent to search in large and complex data sets. This method can solve not only constrained or unconstrained but also discontinuous, non-differentiable, stochastic or highly non-linear optimization problems [49][48].

All things considered, in this work the optimization is based on the genetic algorithm.

2.8.1 Single-Objective Genetic Algorithm

The GA starts with a random initial group of candidates called individuals normally distributed throughout the domain, this group is called initial population. For each step of the method a new population of individuals is created, or usually called, a new generation. In each generation, all individuals are tested against the objective function evaluating their fitness. Following the evolutionary biology, the next generation is made based on elitism, mutation and crossover. This process is repeated creating successive generations until the stopping criterion is satisfied [49].

The genetic operators (elitism, mutation and crossover) create the new generation from the individuals that have better fitness values from the current population:

- Elitism: the individual or individuals with the best fitness values remain to the next generation. This process ensures that the best characteristics of the previous population remain in the next generation;
- Mutation: creates a new individual for the next generation mutating randomly its characteristics. This process prevents getting stuck in local solutions and search in a broader space. The percentage of individuals in the next generation created by mutation should be set low to prevent a random search for the solution;
- Crossover: creates another individual for the next generation combining randomly characteristics from two individuals with good fitness values. This process along with the elite selection ensure the algorithm convergence [49].

A graphically simplification of these operators is presented in figure 2.8.

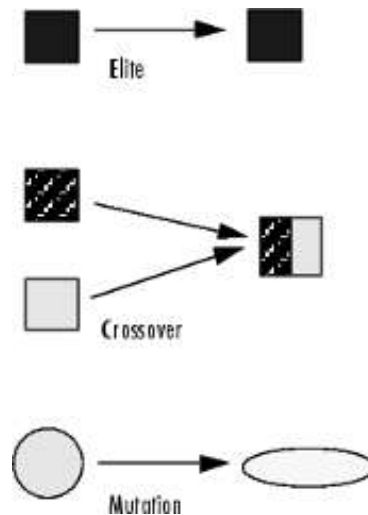


Figure 2.8: Elite, crossover and mutation in genetic algorithms.[49]

The selection of the individuals that have the best characteristics is made by a stochastic uniform process that is based on the scaled value of each individual. Although there are other ways for the selection, this process is a robust and the most used way to do the selection in the GA. This process creates a line in which each individual corresponds to a section of it, with proportional length to its scaled value. After that, the algorithm goes along the created line in equal spacings, and allocates in each step, one individual for the pair that will form another to the next generation [50].

Before the selection, only for the single objective optimization problem, the individuals are scaled. This is very important when it comes to distinguish fitness values of 1 and 2 compared with 101 and 102, for example. The easiest way is scaling proportionally, but the most used is the scaling by rank. This method is based on fitness value rank instead of their raw fitness values. It starts by creating a row with positions beginning in the most fitness value with the rank 1, the next with 2 and so one. In the end, the scaled value of each individual with rank r is proportional to $1/\sqrt{r}$. One of the advantages of this method is that it puts the low ranked individuals nearly in the scaling, by meaning of the square root [50][49].

When it comes to stopping the GA incrementation, there are several stopping criteria but the most used are:

- Maximum number of generations, so algorithm spots when it reaches this number of iterations;
- Function tolerance and a number of stall generations, making the algorithm stop if the average relative change in the fitness value of the best individual, over these stall generations, is less than or equal to the function tolerance [49].

Being the first stopping criteria simpler, the second is suitable to problems with high computing times because it stops when the desired convergence is reached.

Figure 2.9 is a simple example that demonstrates how the genetic algorithm works, where the blue circles represent the global minimum and the green and red ones are local minimums.

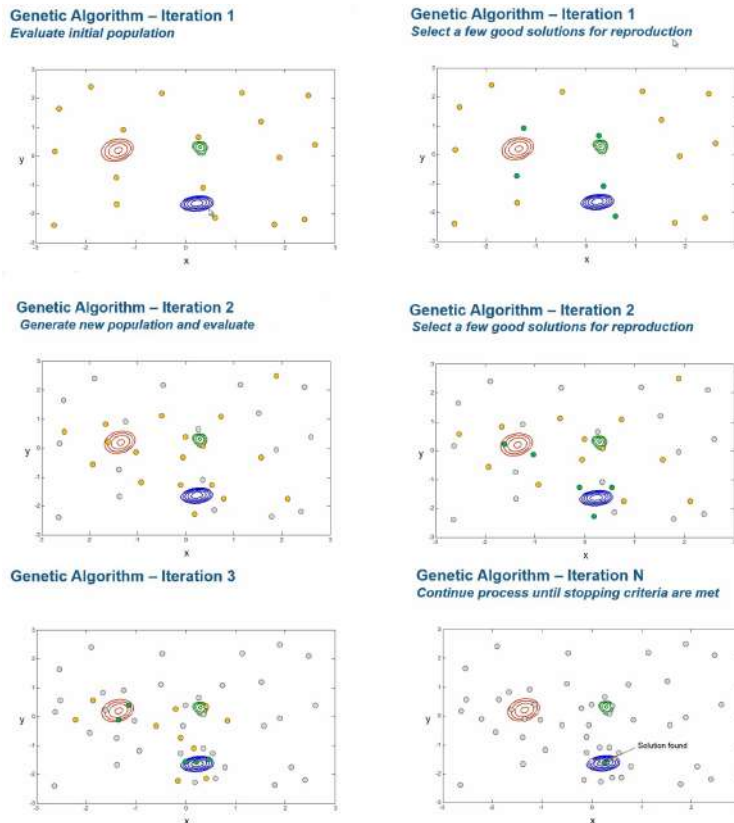


Figure 2.9: Genetic algorithm example (adapted from [49])

2.8.2 Multi-Objective Genetic Algorithm

To formulate a multi-objective optimization problem (MOO), two or more objective functions are required that must be traded off in some way. If the objective functions are competing, there is no unique solution to the optimization, therefore, there are several optimal solutions that lie on the pareto front. The pareto front is constructed by non-dominated solutions as shown in figure 2.10.

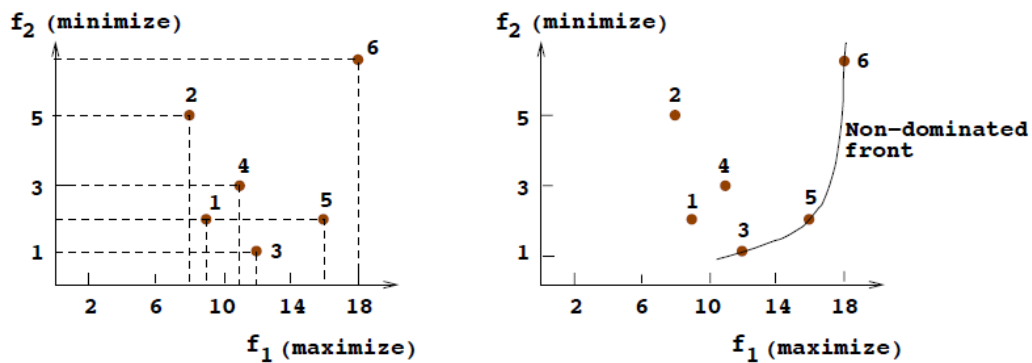


Figure 2.10: Non-dominated front (adapted from [51])

A point x dominates a point y if:

- The solution x is better than y in all objectives;
- The solution x is strictly better than y in at least one objective [51].

The solutions are compared based on their objective function values in the feasible space defined by the constraints of the MOO. The non-dominated solution is the one in which an improvement in one objective implies a degradation of another [51][49].

When the results do not converge into a single solution, the evolutionary algorithm tries to find a set of solutions which lie on the pareto-optimal front and are diverse enough to represent the entire range of the pareto-optimal. The pareto-optimal front is the final pareto that the algorithm gives in the output when it reaches the stopping criteria. After the pareto-optimal front is found, choosing a single solution involves a higher-level information. The user needs to choose the best trade-off solution based on qualitative information. Figure 2.11 shows the schematic of this process [51].

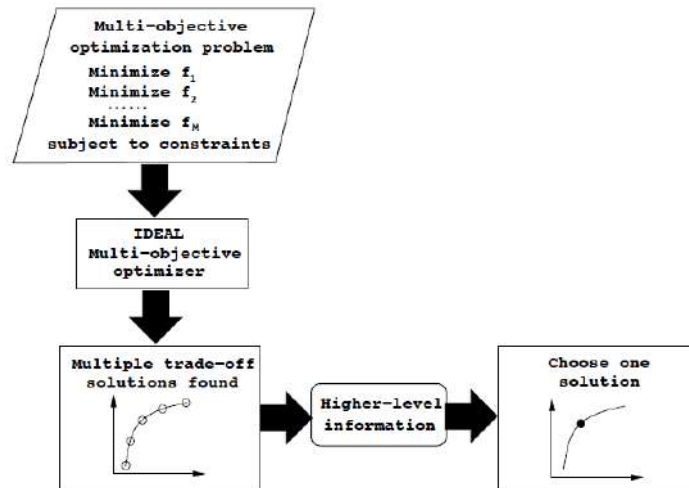


Figure 2.11: Schematic process of single solution choosing (adapted from [51]).

In the present work, the *gamultiobj* a *MATLAB*[®] function that is based in the *NSGA-II* algorithm is used to find the pareto-optimal front. This function can be divided in five steps:

1. Select each parent by a tournament of at least two individuals randomly chosen from the current population. The individual with the best fitness values is the winner of the tournament and is the chosen one. Normally the number of individuals for the tournament is set to four;
2. Create the child population from the selected parents by mutation and crossover, processes explained in the previous section;
3. Combine the current and the child population into an extended population;
4. Compute the rank and crowding distance for feasible individuals in the extended population. Essentially the individuals placed in the rank 1, are the ones that are not dominated by any other, in

the rank 2 are the ones dominated by the rank 1 individuals and dominate the rank 3 ones and so on, as exemplified in figure 2.12. The infeasible individuals are ordered by a sorted infeasibility measure, plus the highest rank in the feasible individuals, therefore, all infeasible ones have a worse rank than any feasible individual.

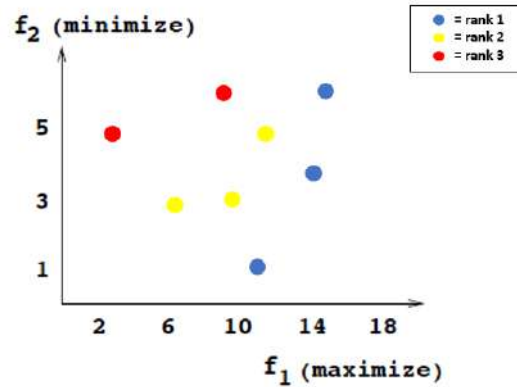


Figure 2.12: Ranked individuals.

The crowding distance is a measure of the closeness of an individual to its nearest neighbors. This measure sorts the individuals inside of each rank by the largest to the smallest crowding distance, therefore, higher distance is better. This distance of the individual i to its nearest neighbors is extracted by calculating the perimeter of the cuboid [51], as illustrated in figure 2.13;

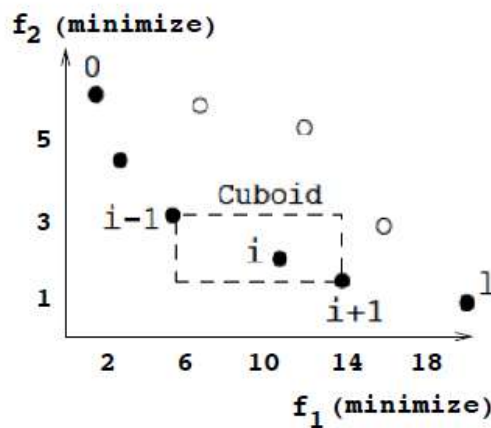


Figure 2.13: Cuboid (adapted from [51]).

- Trim the extended population into the population size, that will be the next generation. This method guaranties the elitism of the process, the parents with best scores remain to the next generation [49].

The *NSGA-II* algorithm can be summarized in figure 2.14 where P_t represents the current population, Q_t the child population, R_t the extended population and the F_i the ranks.

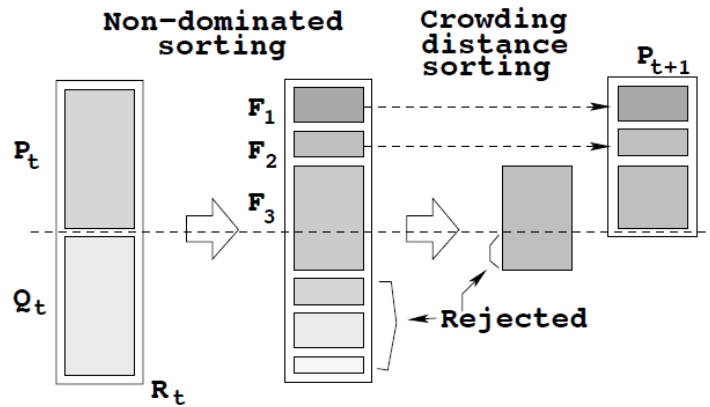


Figure 2.14: NSGA-II algorithm schematic (adapted from [51]).

In order to stop the algorithm, several stopping criteria can be used, but the most common are:

- Maximum number of generations, so algorithm stops when it reaches this number of iterations;
- Function tolerance and a number of stall generations. The algorithm stops if the average relative change of the spread over the stall generations is less than the function tolerance, and the final spread is less than the mean spread in these stall generations [49].

The spread measures the movement of the local pareto front in each generation. Based on the standard deviation of the crowding distance and the difference in the sum of the distances between the minimum fitness values for each objective function between generations. Therefore, the spread is smaller when the solutions on the pareto front are spread evenly and when there are no significant changes between generations in the minimum fitness values. The minimum fitness values are considered because the *gamultiobj* is constructed to minimize all objective functions.

Chapter 3

Implementation

In this chapter the whole process from the project requirements, material choice until the way the structure is analyzed in crash and statically is discussed and explained. The structure studied is highlighted in figure 3.1 where its position in relation to the Be2.0's chassis can be seen.

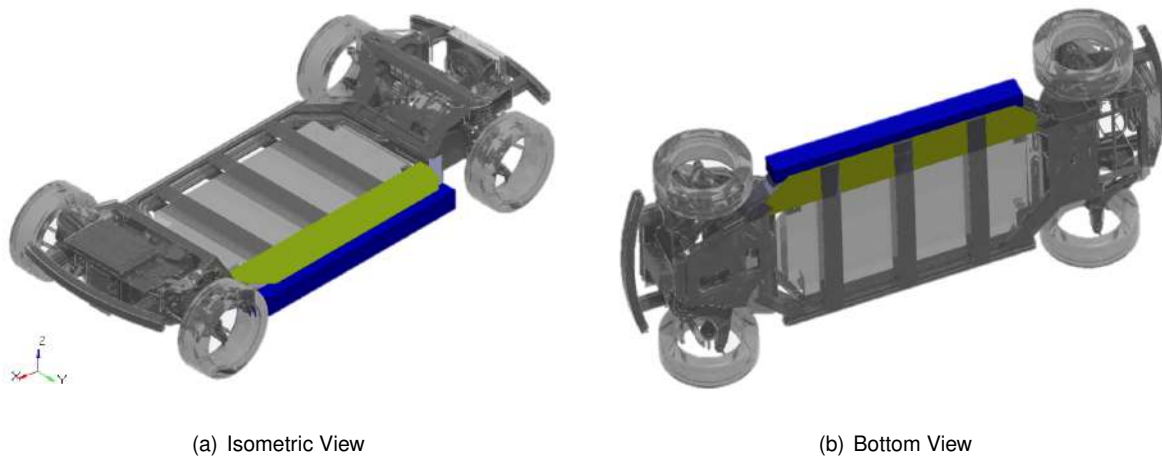


Figure 3.1: Be2.0's chassis with the structure highlighted.

The axis system used in this project is shown in figure 3.1, X is the longitudinal, Y is the lateral and Z is the vertical direction.

3.1 Project Requirements

The design of the side beam chassis for the Be2.0 is a rigorous process that has to meet dimensional, structural, crashworthiness, material and fabrication requirements, applied to the project by CEiiA.

The structural requirements are basically related with rigidity and stress:

- The maximum deflection in Z direction of the beam must be less than or equal to 1mm, bearing 600kg uniformly distributed, doubly supported at its tips in static and dynamic situation;

- The maximum torsional deflection must be less than or equal to 0.04rad, bearing 355.5Nm at its tips in static and dynamic situation;
- To simulate the worst case scenario, the two previous requirements must be computed simultaneously;
- The safety factor for the Von Mises criterion is 1.5.

The materials and fabrication requirements are:

- The material must be aluminum;
- The fabrication method must be an extrusion.

The dimensional constraints are related with the batteries' height and with the length and width of the car:

- The beam's height must be 140mm, to support the bottom and floor of the car separated by the height of the batteries;
- The beam's length must be 1660mm and supported at 1600mm to be in agreement with the Be2.0 total length;
- The beam's width can range from a minimum of 80mm to 140mm but, to meet the Be2.0's total width, the target value is 130mm.

The crashworthiness requirements are the most rigorous and difficult to overcome, because the test applied to the beam must be as close as possible to the Euro NCAP pole test:

- The structure has to withstand the impact with 800kg, the rest of the car's mass should be supported by other structures, such as the car door and roof;
- The velocity and pole's dimensions must be equal to the Euro NCAP pole test;
- The maximum acceleration during the contact beam-pole is 80G, in order to simulate Euro NCAP pole test;
- The maximum HIC_{15} is 700, to simulate Euro NCAP pole test;
- The maximum intrusion of the beam inside the Be2.0 is 150mm to protect not only the driver but also the batteries;
- The vehicle's motion forms an angle of 90° with the vehicle's longitudinal centerline, to perform a more demanding test than the Euro NCAP pole test on the analyzed values, as explained in section 3.6.

3.2 Structural Analyses

During operation, the vehicle's chassis is subjected various loading cases:

- Bending case, due to components' distributed weight along the car;
- Torsion case, due to different loads at each axle;
- Combined bending and torsion;
- Lateral loading, due to the curve maneuver or kerb bumping;
- Fore and aft loading, due to acceleration and braking [26].

The bending, torsion and the superposition of the two are the most important cases for the chassis analysis. The lateral, fore and aft loading are very important to other studies like suspension performance.

3.2.1 Bending Case

Depending on the position and weight of the main components and possible payload, the load distribution can be approximated and the reactions on axles can be calculated by mean of equilibrium of forces and moments.

The dynamic bending loading that appears during the car operation must be considered, not only due to force peaks, but also due to fatigue failure. Experience in car construction allows a simplification of the dynamic analysis, consisting of just increasing the static loads by 2.5 times and make the study in static behavior. These multipliers are called dynamic factors [26].

3.2.2 Torsional Case

In the car operation, pure torsion of the chassis is very unlikely to happen, it appears always combined with vertical load. The maximum torsion moment takes place when one wheel from the less loaded axle is raised until the opposite wheel leaves the ground. Again, to simulate the dynamic effect a dynamic factor of 1.3 is used [26].

3.3 Aluminum Alloy Choice

To choose the aluminum alloy that meets all requirements it is imperative to analyze various aspects. The strategy is to first select the alloys that fulfill the restricted requirements like corrosion resistance, weldability and extrusion, and then among the selects ones, choose the one that has the best structural and crashworthiness performance.

One of the main objectives is to produce the side beam with low weight. Being the density of all aluminum alloys around $2.7 - 2.9g/cm^3$ does not make sense to analyse low strength alloys (maximize

strength-to-weight ratio). The medium-high strength alloys can be found in the 2xxx, 5xxx, 6xxx and 7xxx series.

Comparing the corrosion resistance of the 4 series alloys selected so far, the 2xxx and 7xxx alloys are the least corrosion resistance, presenting a bad performance in this field. To use them in industrial application, they have to be sheltered with an additional corrosion protection [24][52].

The weldability does not constitute a problem in 5xxx and 6xxx series. They are weldable by overall commercial procedures and methods, in rare exceptions they need to be welded by special techniques [52][53].

The extrudability in the alloy's selection is very important, because not only establishes a minimum thickness but also, considerably influences the cost. The 6xxx series are the predominant alloy in extrusion allowing thinner sections, high extrusions rates and low cost of production [54].

The 6xxx are the selected alloys so far, and again, the same strategy of eliminating the lower strength alloys was implemented. The ones with less than 200MPa tensile yield strength were not analyzed in structural and crashworthiness performance. The characteristic from the selected ones can be found in table A.1 in appendix A.

The contribution from the material in bending stiffness (EI) corresponds to the elastic modulus E . The moment of inertia I is mainly dependent on the shape. The variation of E is small, presenting values from 68 to 70GPa among the selected ones until here. Analyzing the torsional stiffness (GJ) where the torsional constant J depends mainly on the shape, the contribution from the material corresponds to the shear modulus G . Analyzing selected alloys so far, the G presents no variation, taking the value of 26GPa in all cases.

The values that present a considerable variance are the ultimate resilience (that measures the amount of energy absorbed by the material until its failure, one of the most important parameters in crashworthiness performance), the shear and yield strength. Therefore, the choice is going to be based in the best commitment of these 3 parameters. Graphically, this comparative can be observed in figure 3.2.

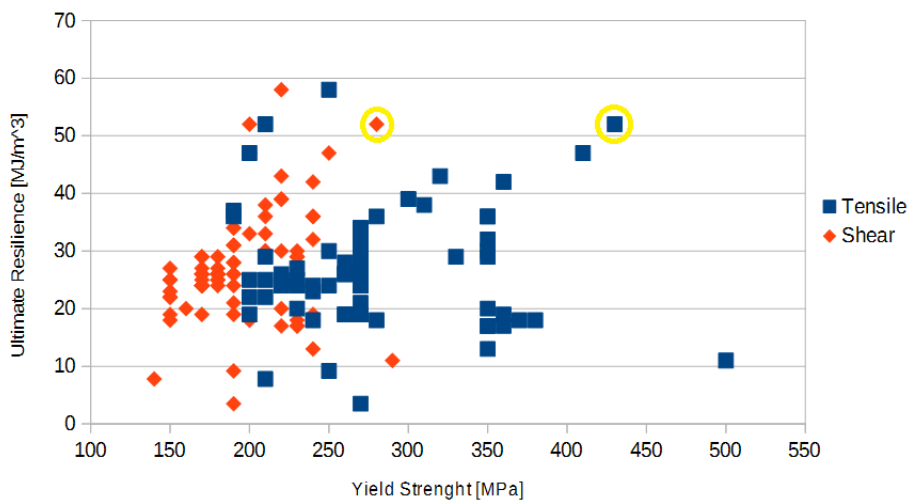


Figure 3.2: Ultimate resilience vs tensile and shear yield strength

The alloy marked with yellow circles in figure 3.2 is the 6110A-T6 alloy. This alloy maximizes the relation between ultimate resilience, tensile and shear yield strength. It is normally used in bumper systems, crash management systems and side sills [21]. The properties of the 6110A-T6 alloy are summarized in table 3.1.

Table 3.1: Aluminum alloy 6110A-T6 properties

Property	Value	Units
Young Modulus E	70	GPA
Shear Modulus G	26	GPA
Density ρ	2.8	g/cm^3
Tensile Yield Stress	280	MPA
Ultimate Tensile Stress UTS	470	MPA
Shear Yield Stress	430	MPA
Failure Strain	11	$\%$
Ultimate Resilience	52	MJ/m^3

3.4 Optimization Cycle

To design the beam an optimization cycle fully controlled by a *MATLAB*[®] program was created. This way, it allows not only to find the best shape for it, but also, save time and resources. This cycle can be applied to projects with similar approaches, it is only necessary changing the inputs of the program allowing to size the beam for various applications. For the project Be2.0, this cycle can be important because larger cars or mini-buses will be designed using the same chassis but reinforced. This cycle can be outlined according to figure 3.3, where the different points of the cycle are explained in the following subsections. A detailed schematic can be found in section 3.4.9.

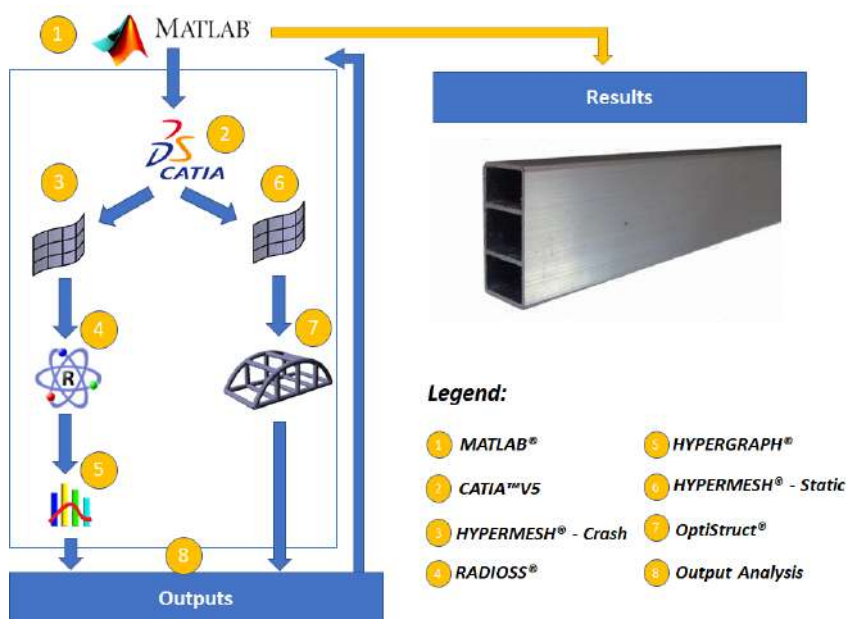


Figure 3.3: Optimization cycle

3.4.1 MATLAB®

Represented in figure 3.3 with the number 1, a *MATLAB*® program controls the overall process giving the inputs to the cycle, and then, receiving and analyzing the outputs. Cycle inputs are the variables to be optimized in the beam which can be for example width, thickness, reinforcements or even the material. Everything that is parameterizable in *CATIA*™ V5 or even parameters in the *HYPERMESH*® can be variables of the cycle giving a huge freedom to the user to choose what to optimize.

The *MATLAB*® program is where the genetic algorithm is implemented. This algorithm is found in functions from the *MATLAB*® library, in which, for multi-objective problems, the *gamultiobj* function is used in this work. The *gamultiobj* finds a local pareto front for multiple objective functions. This function receives several parameters such as, functions to be optimized, variables and their range, linear equality and inequality constraints, non-linear equality and inequality constraints, and options.

The parameter options it is a function called *optimoptions* from the Global Optimization Toolbox from *MATLAB*® library. The *optimoptions* function is where the programmer can control how the *gamultiobjective* will work. In this function it can be defined the size of the population, the stopping criteria defined by the function tolerance and the *MaxStallGenerations* or a limit of generations, the percentage of the next generation individuals created by crossover or mutation and the plots like the pareto front or the distance between the individuals in each generation.

These are the simplest options to control the genetic algorithm, but if necessary, this option allows to receive an initial population, a mutation or crossover function created by the programmer, maximum simulation time, and others. In this optimization cycle the *crossoverarithmetic* is the crossover function used, this function creates children that are the weighted arithmetic mean of two parents. This function has a great advantage, the children are always feasible with respect to linear constraints and bounds. To mutate the parents the function *mutationgaussian* is used, this creates the mutated children using the Gaussian distribution. In order to produce the mutation children feasible with respect to the bounds, the output of this function goes through another function that forces it to comply with these constraints. The *mutationgaussian* function does not satisfy linear constraints, however, as this problem does not contemplate these constraints, there is no incompatibility [49].

Since the objective of this project is to increase the performance of the beam in crash, as well as to reduce its mass, as explained with detail in section 3.4.8, the objective functions are 1/CFE and the beam's mass. It was chosen to minimize the mass instead of maximizing SEA. It would make sense to maximize SEA, however for this particular study it does not. Since the structure energy absorption will always be equal to its kinetic energy, the SEA is given as

$$SEA = \frac{EA}{m_{beam}} = \frac{0.5(\sum M)v^2}{m_{beam}}, \quad (3.1)$$

substituting the velocity, applying the distributive rule and substituting the mass of auxiliary components,

$$SEA = \frac{0.5(800 + m_{aux. components} + m_{beam})8.89^2}{m_{beam}} = \frac{0.5(800 + 9.33)8.89^2}{m_{beam}} + 0.5 * 8.89^2. \quad (3.2)$$

Everything is constant except for the beam's mass. Therefore, for this specific case minimizing the beam mass is equivalent to maximizing SEA. This coefficient is important for comparing different structures in distinct application cases.

The results from the objective functions depend on the realized simulations in this cycle, as well as the constraints HIC_{15} , acceleration, intrusion, torsional deflection, displacement in Z direction and Von Mises equivalent stress. These constraints are depended of the computational simulation, therefore they are considered non-linear. All these constraints need to be below certain values, as explained in section 3.4.8. All this cycle is inserted into a single function that is invoked by the genetic algorithm. This drags an associated problem, both the objective functions and the non-linear constraints depend on the same function.

The time consumed at each iteration is the main problem of this cycle and, to avoid the cycle being invoked twice in a single iteration, it was created an embed function in nested function. These functions keep recent values to calculate the constraints and the objective functions just once. This function, once called the cycle function to calculate the objectives or the non-linear constraints, calculates both and saves the results. When it is called again only returns the results previously calculated [49].

The same strategy is used to avoid recalculate the individuals previously calculated in the same or previous generations. The results of all individuals are saved in a matrix inside the cycle function. The elite individuals that go into the next generation, or even repeated individuals formed by crossover or mutation, are calculated just once allowing a large time savings.

The control of the other programs is also done by the *MATLAB* script. All programs run with their respective macros from the *Windows* command line. This is possible with the help of the *dos* function that executes the specified *Microsoft*[®] Disk Operating System (MS-DOS) command for *Windows* platforms. The *dos* function waits until the process is executed and return 1 or 0 for success and failure respectively. This *MATLAB*[®] script performs more work, explained in detail throughout the description of this cycle.

3.4.2 *CATIA*[™] V5

The 3D design program used in this project, represented in figure 3.3 with number 2, is *CATIA*[™] V5. Developed by *Dassault Systèmes*, a French company, this program allows to read macros, to be executed in batch mode and is parameterizable [55].

The first step before placing the CAD3D beam in the cycle, is to design it and parameterize the desired variables. Attached to the beam are the structures that support it to better simulate its joint performance, connections, or even how the forces propagate. Then it is necessary to create a macro that opens the pre-designed beam, change these parameters and save it again. This macro is a *.catvbs* file that can be written with *MATLAB*[®] functions. Finally, *MATLAB*[®] changes the desired parameters and from the *Windows* command line it runs the macro in window batch mode. This mode start *CATIA*[™] V5 without any user interface which makes it run considerably faster.

Summing up, this part of the cycle receives the variables to be optimized, redesigns the CAD3D

model of the beam and saves a *.CATPart* file that can be read by the *HYPERMESH*[®] program.

Figure 3.4 exemplifies some parameters that can be parameterized in a beam (in blue).

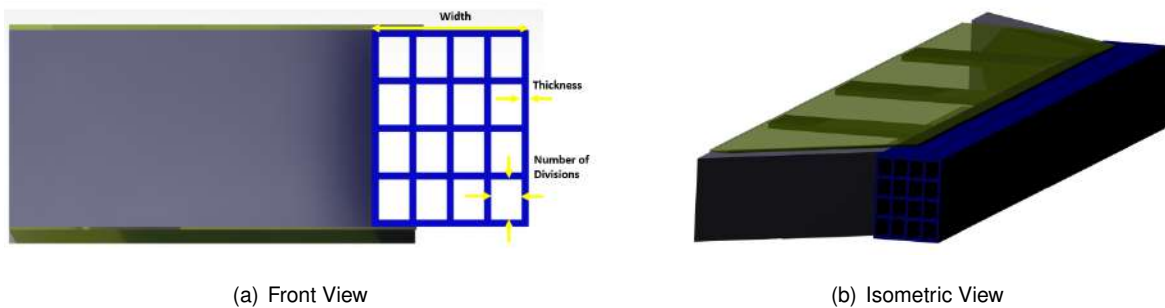


Figure 3.4: Parameterized beam

3.4.3 *HYPERMESH*[®] - Crash

HYPERMESH[®] is one of the programs that the Computer-Aided Engineering suite of *HYPERWORKS*[®] has to offer. Developed by the Americans *Altair Engineering* the *HYPERMESH*[®] software is market-leading, multi-disciplinary finite element pre-processor [56].

Represented the figure 3.3 with the number 3, the *HYPERMESH*[®] software is responsible for the finite element pre-processing of the crash simulation using the user profile *RADIOSS*.

A macro is created to run this part of the cycle, as a *.tcl* file, that can be written by *MATLAB*[®] functions, which allows to rewriting parameters at each iteration. The creation of the macro is described in the following subsections. After its creation, the *.tcl* file can be run from the *Windows* command line as described in section 3.4.1.

Node Creation

The first step is to create three nodes that will be the basis for the rigid node, the rigid wall and the third one is where the intrusion can be measured, explored in detail later. Creating these nodes at the beginning of the macro is a strategy to know their ID. When a mesh is made, *HYPERMESH*[®] assigns ID's to the nodes and elements automatically without the user having control over it. Creating these nodes at the beginning guarantees that they have ID 1, 2 and 3 following the creation order of each node.

CAD3D Importing

After the creation of the nodes, the *.CATPart* file is imported, *HYPERMESH*[®] maintains the original axis system from the CAD3D of *CATIA*[™] V5, maintaining the orientation of the part as seen in figure 3.5. This is very important to select nodes, orientation of the imposed velocity, direction of the boundary conditions and many other operations, as will be further analyzed.

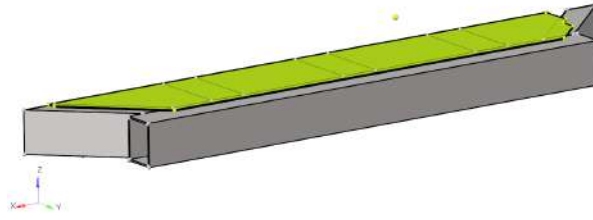


Figure 3.5: Imported geometry

Midsurface

The names of the components created in *CATIA™ V5* as well as the orientation are maintained when the file is imported into *HYPERMESH®*. This allows to select each one of the eleven components using their name and, then extract the midsurface of each one of them, as shown in figure 3.6. To every midsurface is attributed the same name of the component that gave rise to it. Subsequently, all the source components are deleted, and from this point onwards, only the midsurfaces are used. The midsurface is an extracted surface from the center plane of the thin-walls. Thin-walled components are parts that have thickness considerably smaller compared with its width and length. Working with the midsurfaces allow to use 2D shell elements instead of 3D solid ones. Using this approach makes the analysis simpler and the computation time faster. The color of the components are changed in order to easily differentiate them.

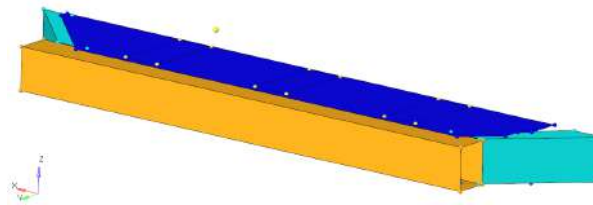


Figure 3.6: Midsurface

Mesh

The creation of the 2D mesh in the midsurfaces is done with the help of another program, the *BATCHMESHER®*, which can be directly called from *HYPERMESH®*. This tool automatically recognize the geometry and perform a cleanup in batch mode. With this strategy it is possible to create a high quality mesh for the size and type of element, as shown in figure 3.7.

The control of the mesh creation, the size of the element, recognition and cleaning of the geometry is made according to two files, the criteria and parameter file. The element size is defined according to the mesh convergence study presented in section 3.5.

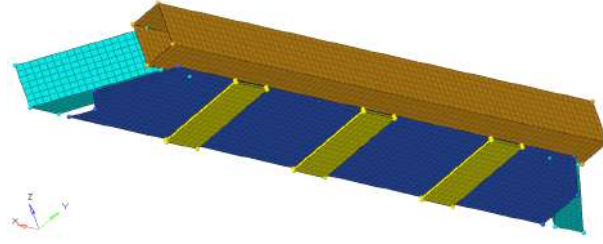


Figure 3.7: Meshed geometry with 20mm element size

Materials

The next step is the materials' creation. Two different materials are needed, one for the auxiliary structures and the other for the beam itself. The beam's material has the characteristics presented in the aluminum alloy choice detailed in section 3.3. The auxiliary structures already had their material defined from the Be2.0 project, it is the aluminum alloy 6061-T6 with the following characteristics:

Table 3.2: Aluminum alloy 6061-T6 properties

Property	Value	Units
Young Modulus E	69	GPA
Shear Modulus G	26	GPA
Density ρ	2.7	g/cm^3
Tensile Yield Stress	270	MPA
Ultimate Tensile Stress UTS	310	MPA
Shear Yield Stress	210	MPA
Failure Strain	10	%
Ultimate Resilience	30	MJ/m^3

In both materials the inputs for *HYPERMESH*[®] are density, young modulus, Poisson coefficient, tensile yield stress, ultimate tensile stress and strain at ultimate tensile stress.

Then *HYPERMESH*[®] will calculate the Johnson-Cook constants that can be found in the starter output file. The simpler form of the Johnson-Cook equation explained in section 2.5 is approximated by setting the strain rate coefficient value to 0 as well as the melting temperature to 10^{30} . With this strategy, the relationship between the stress and the plastic strain rate is eliminated, as well as its temperature dependence [46].

Properties

Just the material alone does not define the component, its card image need to be set as *Part* and a property must to be assigned to it. The card image defines a specific entity. As many properties as different thicknesses present in the eleven components are created, therefore four are created. The components are being treated as surfaces, so the four different properties must be defined as *SHELL*, the appropriated property to use 3 or 4 node shell elements. To inhibit hourglass modes (zero-energy modes of deformation that produce zero strain and no stress), the property formulation need to be set as *QEPHShell* with five integration points, because hourglass modes occur in under-integrated elements [57].

Rigid Pole

The creation of the pole is the next step. In order to simulate the Euro NCAP pole test, a rigid pole with the same dimensions of the pole from this test is created. The pole is created using a *rigid wall*, a non deformable surface with the shape of a cylinder as seen in figure 3.8. This surface has its center in the node that was already created (ID1), with a radius of 127mm. The location of this node is always calculated according to the width of the beam. The rigid pole is always placed as close as possible to the beam, in an effort to avoid wasting computation time.

For the contact to happen between the beam and the pole, it is necessary to set the pole surface as master and the structures as slaves. This is important because slave nodes are constrained not to penetrate the master surface.

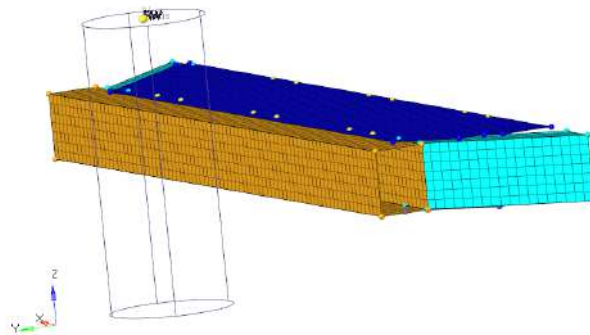


Figure 3.8: Pole

Rigid Body

Behind the structure, a rigid body is placed for a simple and computationally lightweight simulation of the car's inertia. Rigid bodies are rigid link elements with one independent node and variable dependent nodes. The user can choose which degrees of freedom it can have. The independent node and the dependent nodes are usually called the master node and slave nodes, respectively. The master node is set to be the node already created (ID2) at the beginning of the macro and the slaves nodes are all those from the rear end of the structure.

In this rigid body, 800kg mass is added, which, according to the project requirements, is the fraction of the all car's mass that the structure will have to stand, absorbing its kinetic energy.

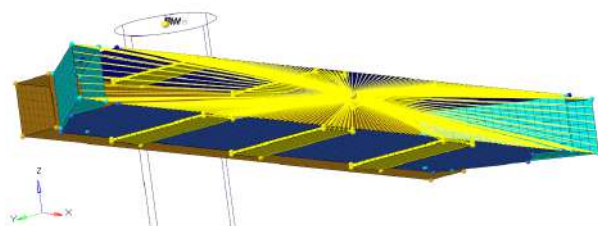


Figure 3.9: Rigid body

Another rigid body is created that will serve as the basis to measure the intrusion of the beam. The previously created ID3 node is used as master and the nearest node of the beam as slave.

Contacts

To prevent penetration during the simulation, it is very important to create contacts between the different surfaces of the components and component's surfaces themselves. These contacts can be made using the *interfaces* command.

Contact *TYPE24* is chosen for being improved and updated in the latest version of the program. This contact can replace the most used contacts in crash like *TYPE7* or *TYPE5*. *TYPE24* is a general surface-to-surface contact interface with a great advantage, when working with shell elements, the gap is calculated automatically. This is important when the different components have different thickness. To simulate the contact with each other and the contact itself, all eleven components are defined as masters and slaves. With this strategy, all possible contacts during the simulation will happen in a stable way preventing penetration.

Connections

To simulate the connections between the components we use the *interfaces* command. The contact *TYPE2* can simulate model spot-welds or rivets, connecting slave nodes to a master surface. To connect the auxiliary components to the beam, ten connections of this type are made, where the components' nodes in the connection area are defined as the slaves and the beam as master.

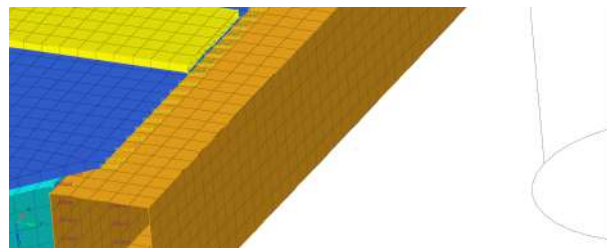


Figure 3.10: Contact *TYPE2*

Velocity

To be as faithful as possible to the Euro NCAP pole test, a speed of 32 km/h is applied to the eleven components, to the 800kg rigid body and also to the rigid body where intrusion is measured. Using the command *BC's Manager*, an imposed velocity or a boundary condition can be created. Each time this command is used, a new load collector is created. In this case, three imposed velocities are created, one for the components and the others for the rigid bodies as illustrated in figure 3.11. The velocity is created with the direction *Y* to force the impact with the pole.

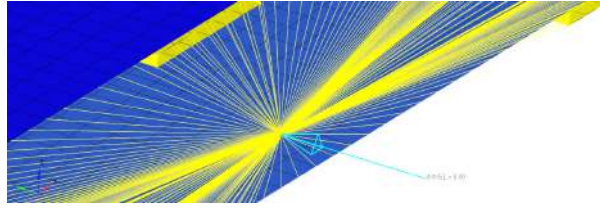


Figure 3.11: Rigid body imposed velocity in m/s

Boundary Conditions

The creation of boundary conditions is very important on pre-processing the model. The boundary conditions are created with the *BC's Manager* command. Similar to what happens with the imposed velocity, a new load collector is created.

A boundary condition is created for the rigid node, as well as, for all nodes from the rear end of the structure as seen in figure 3.12. All degrees of freedom of rotation and translation, with except of the translation movement in the Y axis, are locked. This boundary condition is called SPC, single point constraint, were the user can lock one or more degree of freedom for a given node.

This key process in the pre-processing of the model makes the simulation stable for any beam that the structure receives during the optimization. The structure is not symmetrical with respect to any of its axes, therefore, without these boundary conditions the structure would have an unrealistic rotational and translational movements. These movements do not appear during the Euro NCAP pole test due to inertia of the car or even due to the ground. An example of these movements is the rotation on the X axis that can reach 180° without these boundary conditions, which is not realistic in this type of test.

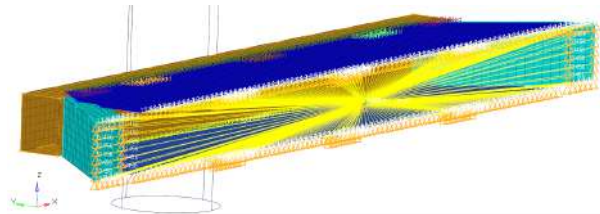


Figure 3.12: Boundary conditions

Control Cards

The control cards contain information on how the simulation should be solved. The desired general outputs must also be requested with this command. The nine different control cards defined in this macro are:

- *TITLE*, the first and the simple control card, defines a title for the output file of the *HYPERMESH*[®] and the input of the *RADIOSS*[®];
- *RUN*, defines how much time the simulation will run. Rigid structures contact the pole for less time than more ductile structures. Ductile structures have higher deformations therefore take longer

to deform. Due to the transformation of the elastic energy into kinetic energy, the structure, after colliding with the pole, presents a displacement in the negative direction of the Y-axis. All the time that the structure is no longer in contact with the pole does not have interest in this work. Defining a high value for simulation time could be a strategy but all the time that the structure is not in contact with the pole is a waste in computing time. Beforehand, a very ductile structure was tested, and it was concluded that 80 ms is a value that will cover all the simulations carried out, maintaining a low computation time;

- *VERS*, defines the version number. 2017 is the version number defined in this compulsory control card that must be coherent with the *RADIOSS*[®] version number;
- *PARITH*, is set to "on" to allow parallel arithmetic in case of multiple *RADIOSS*[®] engine runs. This allows to do more than one optimization at the same time despite not being advised;
- *PRINT*, sets the printout frequency to the output file and it is defined as -10000. The output file is where the error can be observed during and after the simulation. Smaller values (in module) in this frequency, means, printing more values in the output file and make the simulation slower;
- *TFILE*, defines the frequency of printing the time history file (T-file). The frequency is set to be 0.05 and the writing format is left as default to *HYPERGRAPH*[®] be able to read it. Smaller values of this frequency represents more data printed in time history file and a slower simulation;
- *ANIM/DT*, defines when the animation file begins to be written, as well as, its writing frequency. The animation file starts to be written at the beginning of the simulation. The writing frequency is set to be 0.05, smaller values of this frequency make the simulation slower and increase the record memory on the computer;
- *ANIM/VECT*, generates vectorial data from specific variables for the animation file. The chosen variables are *DISP* (displacements), *CONT* (contact forces), and *FOPT* (forces and moments in rigid bodies);
- *ANIM/ELEM*, similar to the *ANIM/VECT* control card, generates data from specific variables for the animation file. The chosen variables are *ENERGY* (specific energy), *VONM* (Von Mises stress), *EPSP* (plastic stain) and *HOURG* (hourglass energy).

Output Blocks

Since outputs from the control cards are not enough for the realization of this project, more specific outputs are required. The output blocks are created for this purpose. Additional data is written in the time history file with three output blocks:

- *RWALL*, this output block applied to the rigid pole writes the contact forces on the pole in all directions. Which is necessary to create the force-displacement curve;

- *NODE*, this output block applied to the master nodes of the two rigid bodies writes results such as velocity, acceleration, displacements, etc. For this work, the most important ones are the displacements, necessary to create the force-displacement curve and to know the maximum intrusion of the beam;
- *PART*, this output block applied to the beam writes many results like mass and moments of inertia. The thickness is changed by *MATLAB*[®] in the component's property, therefore, the beam's mass changes in every cycle. This output block is important because it estimates the mass of the beam in a simple and exact way.

Export

The creation of the macro is almost completed after the steps described previously are done. The final step is to export the created model to a *.rad* file format.

Summing up, this part of the cycle imports the CAD3D model from the output of *CATIA*[™] V5, applies all the steps listed above in this section, and exports a *.rad* file to be read by the *RADIOSS*[®] solver.

3.4.4 *RADIOSS*[®]

The solver used to solve this model is *RADIOSS*[®]. This is a structural analysis solver for highly non-linear problems under dynamic loads. Leader in automotive crash and impact analysis is worldwide used to improve crashworthiness [56].

Represented in figure 3.3 with number 4, this solver runs the *.rad* file output by *HYPERMESH*[®], solves the model and returns the following files:

- The output file, a *.out* file, with errors, CPU user times and used memory;
- The animation file, a *.h3d* file, with the animation of the solution that can be consulted by the post-processing and visualization environment *HYPERVIEW*[®] program;
- The time history file, a *.1T01* file. This is the most important output of the solver for this cycle because it contains the data from the important variables for post-processing of each cycle iteration. As described in the previous section, this information was requested by the output blocks contained in the *HYPERMESH*[®] macro. This file can not be read with *MATLAB*[®] functions, therefore, to get the information contained on it, help from *HYPERGRAPH*[®] program is needed, as analyzed in the next section;
- And others files with no interest in this work.

Running this solver with no intervention of the user is possible because the *dos MATLAB*[®] function executes the specified MS-DOS command for this action in the *Windows* command line. The cycle does not advance until the simulation of the model is completed.

Summing up, this part of the cycle receives the *.rad* file from the output of the *HYPERMESH*[®], runs the simulation, and exports the time history file *.1T01* to be read by the *HYPERGRAPH*[®] program.

3.4.5 *HYPERGRAPH*[®]

Since the library functions of the *MATLAB*[®] cannot read the time history file (*.1T01*), another program is necessary to read this file and export another that can be read by *MATLAB*[®].

The program used is *HYPERGRAPH*[®], represented in figure 3.3 with the number 5. This program is a powerful data analysis and a plotting tool capable of dealing with complex mathematical expressions or filters and always presents a high-quality presentation output [56].

A session file was created previously. This session based on the time history file creates the following curves:

- Force-displacement curve (see figure 3.13). This curve needs to be filtered, as explained in section 3.4.5, and is extracted from the pole-beam contact;

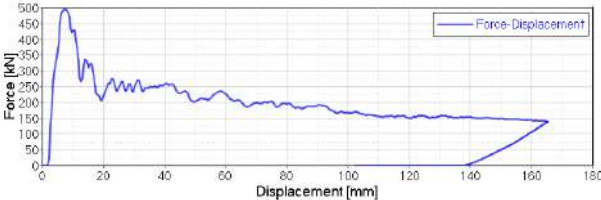


Figure 3.13: Force-displacement curve

- Displacement-time curve (see figure 3.14), extracted from the ID2 node (rear end of the structure);

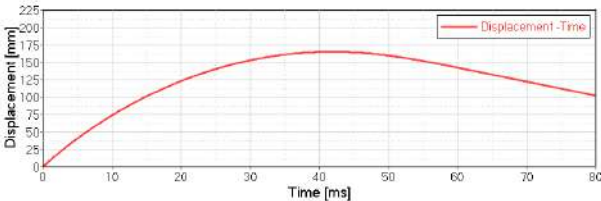


Figure 3.14: Displacement-time curve, from the rear end of the structure

- Displacement-time curve 2 (see figure 3.15), extracted from the ID3 node (rear end of the beam);

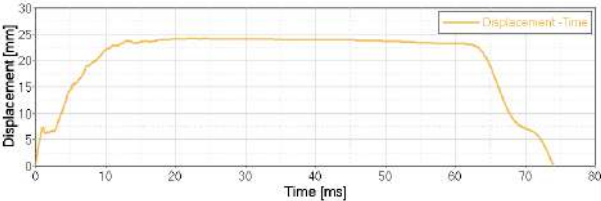


Figure 3.15: Displacement-time curve 2, from the rear end of the beam

- Mass-time curve, a constant curve extracted from the beam.

Direct results or calculated ones from these curves are analyzed further ahead in section 3.4.8, but first, it is necessary to export the curves to a .csv format file. This type of file allows reading by *MATLAB*[®] but, to create it, it is necessary to write a macro in a .tcl format file. Therefore, at each iteration of the cycle, a new macro written by *MATLAB*[®] is recorded, that executes the *HYPERGRAPH*[®] program, applies the session already created (apply filters and creates the curves) and exports the .csv format file with the curves.

Running this macro with no intervention of the user is possible because the *dos MATLAB*[®] function executes the specified MS-DOS command for this action in the *Windows* command line.

Filter

Based on the Euro NCAP [37], the data need to be filtered according SAE J211. According to the certificate of this filter, accelerations must be filtered with a Channel Frequency Class (CFC) of 1000. The application of this filter eliminates noise and vibrations from the results [58].

HYPERGRAPH[®] has a filter option with many filters including this one. Therefore, to obtain the force-displacement curve represented in figure 3.13, first the force-time curve must be filtered.

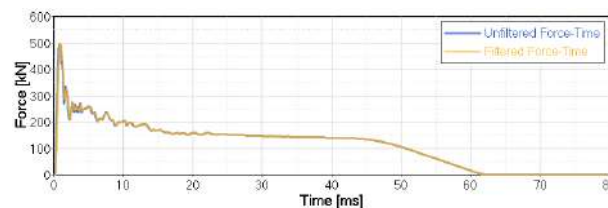


Figure 3.16: Filtered and unfiltered force-time curves

Only after filtering it, and using the *HYPERGRAPH*[®] options, the filtered force-time curve is fused with the displacement-time curve to finally obtain the force-displacement curve.

3.4.6 HYPERMESH[®] - Static

As explained in section 3.4.3, *HYPERMESH*[®] software represented in figure 3.3 with the number 7 is responsible for the finite element pre-processing of the static simulation, using the user profile *OptiStruct*. A macro was created to run this part of the cycle, the macro is a .tcl file that can be written by *MATLAB*[®] functions, which allows to rewrite parameters in the macro at each iteration. The creation of the macro is described later in this section. After its creation, the .tcl file can be run from the *Windows* command line, as described in section 3.4.1.

Node Creation

Two nodes are created at the beginning of the macro that will be the basis for the rigid bodies. Again, the creation of these nodes at the beginning of the macro is a strategy to get to know your ID as explained with more detail in section 3.4.3.

CAD3D Importing

After the creation of the nodes, the *.CATPart* file is imported. Only the beam is studied in this static analysis, therefore the CAD3D model only contains the beam itself as seen in figure 3.17. Details about the CAD3D importing can be found in section 3.4.3.

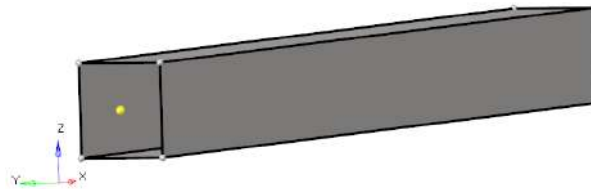


Figure 3.17: Imported beam geometry

Midsurface and Mesh

The next step is to extract the midsurface from the beam and delete the source component. More details about extracting the midsurface from a component can be found in section 3.4.3.

The creation of the 2D mesh in the midsurface is done with help of another program, the *BATCHMESHER*[®], which can be directly called from *HYPERMESH*[®], resulting in the meshed beam shown in figure 3.18. This procedure is also explained in section 3.4.3. The element size is defined according to the mesh convergence study section.

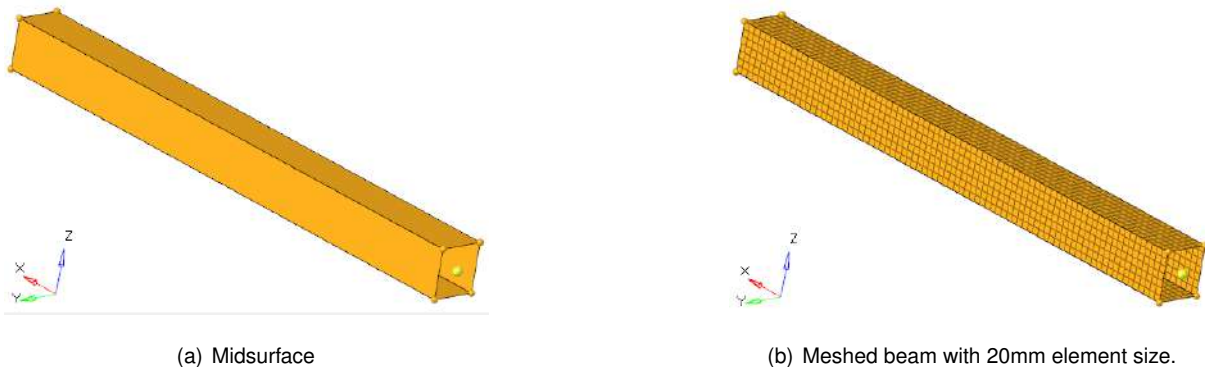


Figure 3.18: Midsurface and mesh.

Material

The next step is the material creation. The beam's material characteristics can be consulted in the aluminum alloy choice in section 3.3.

For this static analysis, the beam is always tested in an elastic regime and if it reaches the plastic regime it is discarded as we will analyze later in this project. Therefore, the material is defined with a card image *MAT1* which defines the material's properties for linear, temperature-independent and isotropic materials. In this case, the inputs for *HYPERMESH*[®] are just density, Young modulus and Poisson coefficient. The simulation with this type of card image is governed by the equations of section 2.5.1.

Property

Just the material alone does not define the component, it is necessary to assign it a property. The beam is modeled as shell, therefore the property must be defined with the card image *PSHELL*, appropriate to use 3 or 4 nodes 2D shell elements.

The thickness of the beam is defined by the property, therefore, if the thickness is one of the variables to be optimized, it must be changed in this part of the macro at each optimization iteration.

Rigid Bodies

Two rigid bodies are placed at the tips of the beam as exemplified in figure 3.9. Details about rigid bodies can be found in section 3.4.3.

The master nodes are set to be the nodes (ID1 and ID2) already created at the beginning of the macro, the slaves nodes are all those from the tip end of the beam. These rigid bodies are very important because they are where the moments and the boundary conditions are placed as explained later.

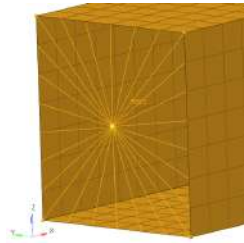


Figure 3.19: Rigid body.

Bending

According to the project requirements, it is necessary to test the beam with a uniformly distributed load of 600 kg applied along the Z-axis. The beam must be supported at its tips to perform this simulation. The maximum deflection in Z direction of the beam must be less than or equal to 1mm, according to the project requirements expressed in section 3.1.

Following the bibliography and as explained in section 3.2, experience in car manufacturing permits a simplification of the dynamic analysis. Increasing the static loads by a factor of 2.5 and making the study just in static behavior allows the engineer, only with a static simulation, to encompass all the dynamic situations that the chassis may be subject in the bending situation, such as peaks of force or fatigue failure.

To apply this force in the beam, first it is necessary to create a load collector. After it, to simulate the uniform distributed load, a pressure is created in the entire area of the upper surface of the beam, calculated as,

$$P = 2.5 \frac{600g}{Lw} \quad (3.3)$$

where L and w is the length and width of the beam respectively and g is the gravity. This pressure surface is illustrated in figure 3.20.

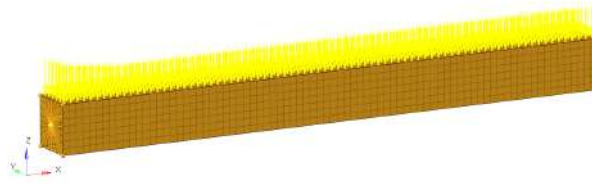


Figure 3.20: Pressure applied to the beam.

Torsion

According to the project requirements, it is necessary to test the beam with a moment of 355.5Nm applied along the X-axis. The maximum torsional deflection must be less than or equal to 0.04rad in the static and dynamic simulation, according to the project requirements expressed in section 3.1..

Following the bibliography and as explained in section 3.2, experience in car manufacturing allows a simplification of the dynamic analysis. To encompass all the dynamic situations that the chassis may be subject in the torsion situation, a dynamic factor of 1.3 is used on the static maximum moment.

As explained in section 3.2, pure torsion on the chassis is very unlikely to happen in the car operation, it always appears combined with vertical load. Therefore, the moment is applied in the same load collector of the previous bending section 3.4.6. To apply this load in the beam, the moment is applied in the rigid body which transmits the torque to all nodes of the beam's tip, as observed in figure 3.21.

Boundary Conditions

To maintain the equilibrium, it is necessary to support the beam at its tips. Taking advantage of the characteristics that defines the rigid body, this boundary condition is placed in its master node.

First a new load collector is created, after it, two SPC are created in each rigid body. In the ID2 node all degrees of freedom are locked, in ID1 node the rotation along X-axis is set free, so that, the torque applied at this node does not suffer any change. With these constraints, the beam is in equilibrium, a necessary condition to perform this simulation.

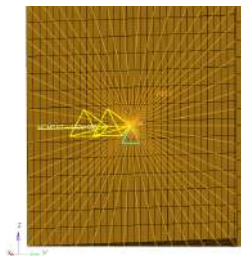


Figure 3.21: Single point constrain with the applied moment.

Load Step

A Load Step entity is created to define and store load cases for a given analysis. This is a key process in the pre-processing of the model. Here, the user chooses what type of analysis and load collectors

he wants to use in the analysis. The type of analysis must be defined as linear static. In the Load Step entity, the load collectors must be defined to put in options *LOAD* and *SPC*. The *LOAD* selects the static loading information and the *SPC* selects the single point constraints. Therefore, the load collector that has the pressures and the moments must be defined as the *LOAD* and the load collector with the boundary conditions must be defined as the *SPC*.

Control Cards

The control cards contain information on how the simulation should be solved. The desired general outputs must be requested with this command. The two defined control cards in this work are:

- *FORMAT*, controls the format of results output. The *HM* and *H3D* options are the selected;
 - The *HM* option gives the information to *OptiStruct*[®] that the *.res* format file must be in the output, the *HYPERMESH*[®] binary results file;
 - The *H3D* option gives the information to *OptiStruct*[®] that the *.h3d* format file must be in the output, the animation file.
- *GLOBAL OUTPUT REQUEST*, controls the outputs that can be requested to the solver. The *DISPLACEMENT* and *STRESS* options are the selected.
 - The *DISPLACEMENT* option controls the output of nodal displacement (and rotation) results;
 - The *STRESS* option controls the output of elemental stress results.

These results are requested in a *.pch* format file.

Export

After these steps above are completed, the creation of the macro is almost finish. The final step is to export the created model in a *.fem* file format.

Summing up, this part of the cycle imports the CAD3D beam from the output of *CATIA*[™] V5, applies all the steps listed above in this section, and exports a *.fem* file to be read by the *OptiStruct*[®] solver.

3.4.7 *OptiStruct*[®]

The solver used to solve this static analysis is the *OptiStruct*[®]. This solver is a structural analysis solver for linear and non-linear problems under static and dynamic loads [56].

Represented in figure 3.3 with number 7, this solver runs the output of *HYPERMESH*[®], the *.fem* file, solves the model and returns the following files:

- The output file, a *.out* file, with errors, CPU user times and memory used;
- The animation file, a *.h3d* file, with the animation of the solution that can be consulted using the post-processing and visualization environment *HYPERVIEW*[®] program;

- The PUNCH file, a *.pch* file. The most important output of the solver for this part of cycle, because it contains the data from the important variables for post-processing of each cycle iteration. As described in the previous section, this information was requested by the control card *GLOBAL OUTPUT REQUEST*. This file can be read with *MATLAB*[®] functions.
- And others files with no interest in this work.

Running this solver with no intervention of the user is possible because the *dos MATLAB*[®] function executes the specified MS-DOS command for this action in the *Windows* command line. The cycle does not advance until the simulation of the model is completed.

Summing up, this part of the cycle receives the *.fem* file from the output of the *HYPERMESH*[®], runs the simulation, and exports the *.pch* format file to be read by *MATLAB*[®], as described in the section 3.4.8.

3.4.8 Output Analysis

Represented in figure 3.3 with number 8, this part of the cycle has the objective of post-processing the data from the output of the static and crash analyses. Here, *MATLAB*[®] evaluates the non-linear constraints, as well as the values of the objective functions, to give as input to the genetic algorithm. This evaluation “close” one iteration of the cycle, which is repeated until the genetic algorithm converges.

The outputs of the static and crash analyses, the *.cvs* and *.pch* files, are read by *MATLAB*[®] and saved into matrices, just after it, the data is analyzed. This strategy permits to save computational time and it does not incur into memory problems, because analyzing data directly in the files takes longer and the two saved matrices are deleted after each iteration.

From the crash analysis output, the *.cvs* file, the values of the objective functions and three non-linear constraints are computed. As explained in section 3.4.1, the objective functions are 1/CFE and the beam’s mass. The *gamultiobj* function minimize the two objective functions and finds a local pareto front, therefore, if the goal is maximize the CFE and minimize the mass, the objective functions must be the beam’s mass and 1/CFE. This strategy guarantees the minimization and the maximization of the mass and CFE respectively.

The beam’s mass is a direct result from the mass-time curve. The calculation of the CFE is an indirect result from the force-displacement curve. According to equation (2.7), the CFE is the result from peak force divided by the mean force, these values are extracted from this curve. All data from the moment that the structure is no longer in contact with the pole are discarded, therefore, this data do not count towards the mean force. If this zone (highlighted in red in the fig 3.22) was considered, the CFE would be affected and we could not compare structures with different displacements.

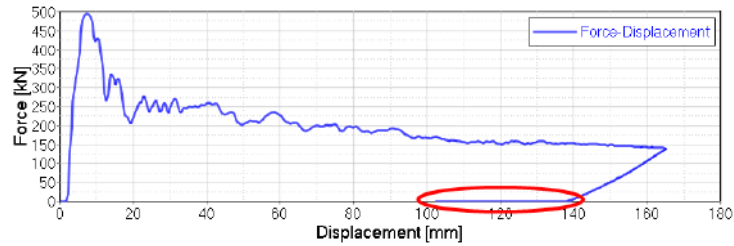


Figure 3.22: Force-displacement curve

The non-linear constraints from the *.cvs* file are the maximum HIC_{15} , maximum acceleration during the beam-pole contact and the maximum intrusion:

- The maximum HIC_{15} is computed according to equation (2.4) but just for 15ms. It is calculated by joining data from the force-displacement and displacement-time curves. In accordance with the project requirements in section 3.1 the HIC_{15} must be less than or equal to 700;
- The maximum acceleration during the contact beam-pole. It is calculated just by dividing the peak force over the sum of 800kg with the all structures' mass. It is computed by joining data from the force-displacement and mass-time curves. In accordance with the project requirements in section 3.1, this acceleration must be less than or equal to 80G;
- The maximum intrusion is computed by subtracting the displacement-time curve 2 from the displacement-time curve and extracting its maximum. The intrusion of the beam into the structure can be exactly measured by calculating this relative displacement and consequently, knowing if the batteries are affected or not. In accordance with the project requirements in section 3.1, this intrusion must be less than or equal to 150mm.

From the *.pch* file, the output from the static analysis, the values for three non-linear constraints, maximum deflection in z direction, maximum torsional deflection and the Von Mises criterion, are computed:

- The maximum deflection in Z direction. The *.pch* file contains the displacements of all beam's nodes. It is evaluated the one with the largest displacement in Z direction. In accordance to project requirements in section 3.1, this deflection must be less than or equal to 1mm;
- The maximum torsional deflection. The *.pch* file contains the displacements of all nodes of the beam ordered by their ID. The maximum torsional deflection is always in the node with the ID1 (the node ID where the moment is applied). For this reason, just this node is evaluated and its maximum torsion in X direction is properly saved. In accordance with the project requirements in section 3.1, this deflection must be less than or equal to 0.04rad;
- Von Mises criterion. The *.pch* file contains the stresses of all beam's elements including the equivalent stress of the Von Mises criterion. It is evaluated the one with the largest equivalent stress and multiplied by the safety factor of 1.5, in accordance with the project requirements in section

3.1 this value must be less than or equal to the tensile yield stress of the material that can be found in table 3.1.

Summing up, with the non-linear constraints and the objective functions calculated, the data post-processing of one iteration of the cycle is concluded. The values are returned to the genetic algorithm function which iterates until convergence.

3.4.9 Optimization Cycle Schematic

The several steps that comprise the beam design optimization cycle described in the previous sections are summarized into a detailed schematic from the optimization cycle in figure 3.23.

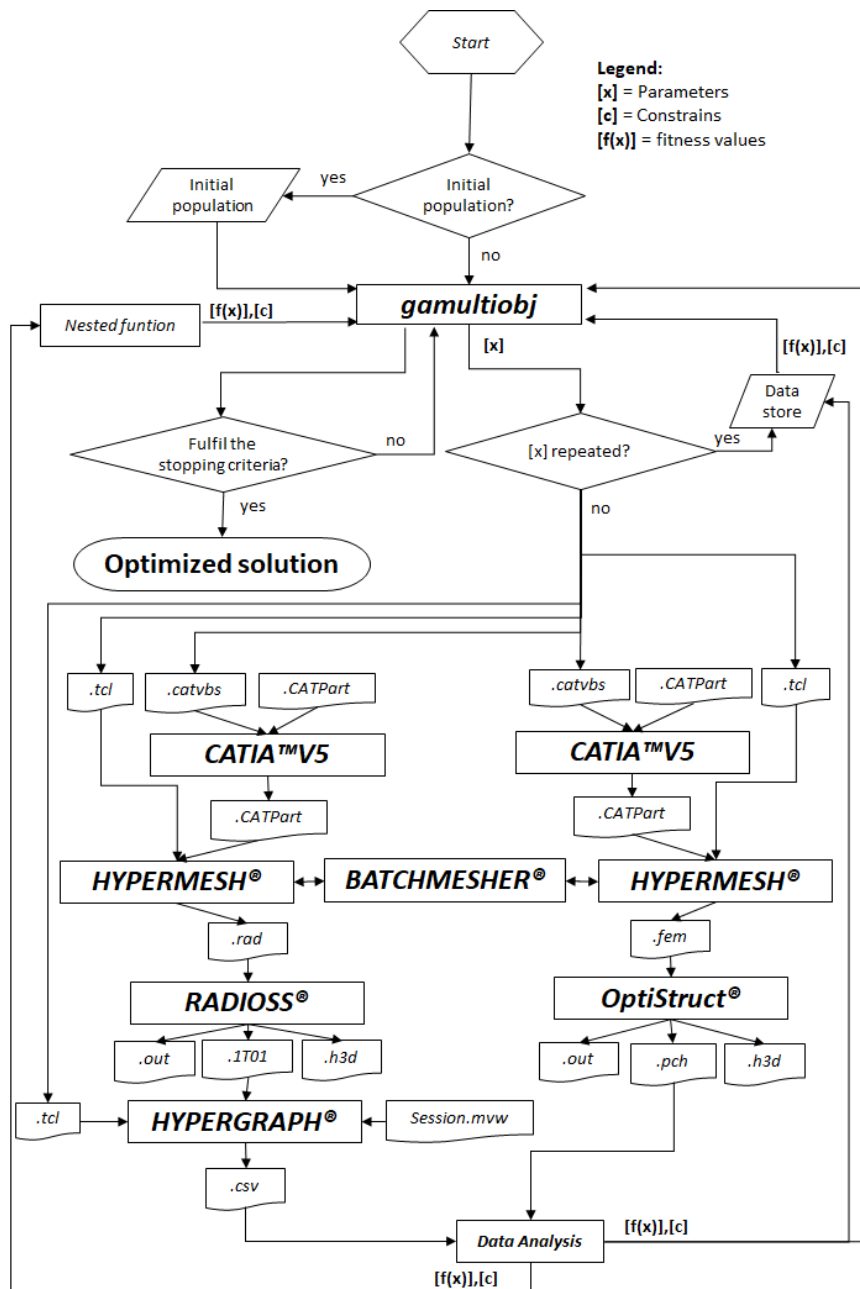


Figure 3.23: Optimization cycle schematic.

3.5 Mesh Convergence Study

To obtain accurate results, a mesh convergence study is needed. The analyses are repeated decreasing the element size until the results are not affected by the additional mesh refinement. When this happens, the mesh convergence study is concluded and the model converges to a solution.

It is important to note that all computing times presented in this section were obtained from the computer provided by CEiiA. This machine is equipped with 8Gb of RAM memory and a generation 5 Intel® processor with 3.6GHz of clock speed.

This study is performed for crash and static simulations.

3.5.1 Crash Simulation

The beam to perform this study has the material properties presented in table 3.1 and has the dimensions shown in figure 3.24



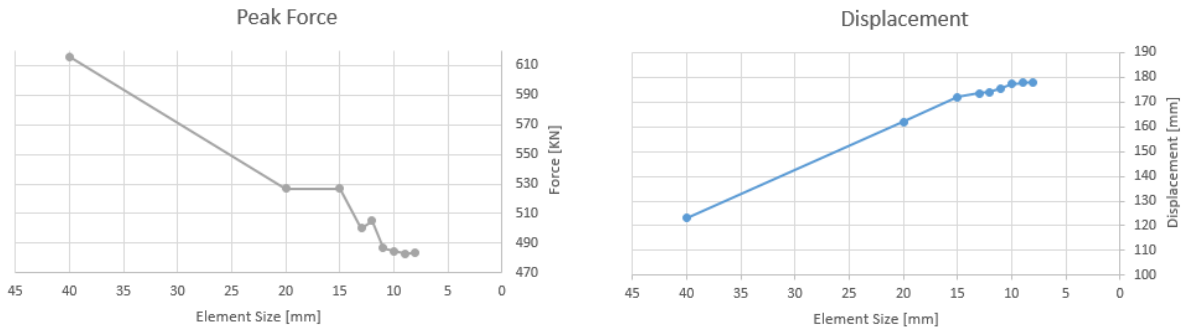
Figure 3.24: Structure front view

To make the mesh convergence study, results from the force-displacement curves are analyzed. For every element size, the computational time, peak force and maximum displacement are analyzed as described in the table 3.3.

Table 3.3: Results from mesh convergence study (crash).

Element Size [mm]	Time [s]	Peack Force [kN]	Displacemnt Maximum [mm]
40	190.2	615.9	123,0
20	649.8	526.8	162,0
15	1137.0	526.9	172,03
13	1712.0	500.4	173,55
12	2029.9	505.2	173,99
11	3388.3	486.8	175,44
10	3757.9	484.5	177,26
9	6818.6	482.8	177,86
8	16731.8	483.6	178,16

As observed in figure 3.26, decreasing the element size represents an exponential increasing in the computation time. It is important to obtain a trade-off between computation time and the accuracy of the results. As proved by figures 3.25(a) and 3.25(b), only for 10mm element size the results converge, from where more refinement of the mesh does not present a significant change of the results.



(a) Peak force-element size curve

(b) Displacement-element size curve.

Figure 3.25: Curves from mesh convergence study (crash).

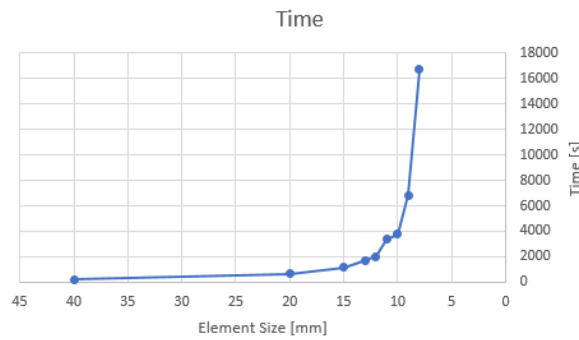


Figure 3.26: Time-element size curve.

Depending on the critical element size and the material, the time-step size control is done automatically by *RADIOSS*[®] in all explicit analyses of this work. The time-step take values to satisfy equation (2.18). The time step for the 10mm element size model is 0.0004 seconds. When compared with the 8mm element size model, this value decreases 35%. It can be verified that both values fulfill equation (2.18). As the element size decreases, which causes a greater number of elements to be calculated with an increasingly smaller time step, the exponential behavior of the computation time shown in figure 3.26 can be explained.

In figure 3.27, it can be observed the convergence of the results. This force-displacement curves were obtained according to section 3.4.5 by applying the proper filter. The difference in the energy absorption from the curve with the lowest refinement (8mm) to the curve with the selected mesh size value (10mm) varies only 2%.

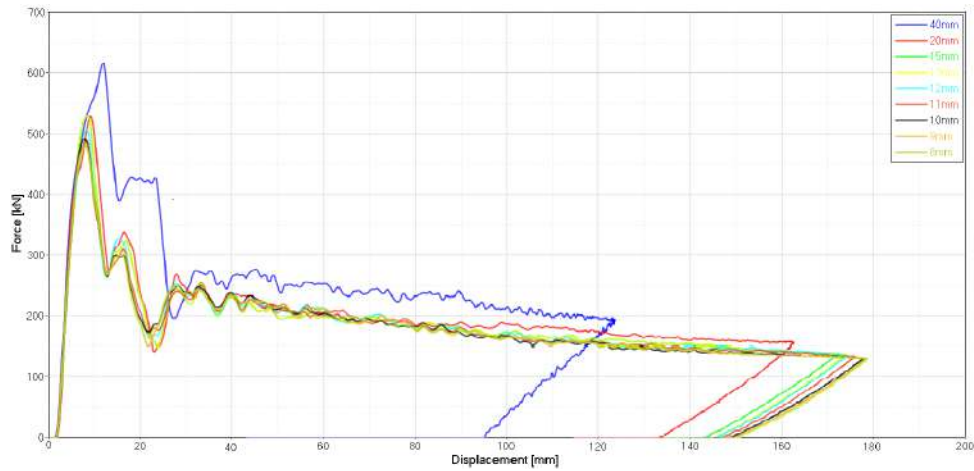


Figure 3.27: Force-displacement curves for every element size.

In figure 3.28 a large difference can be seen between the result with 40mm and 10mm element size, and the similarity between the result with 8mm and 10mm element size.

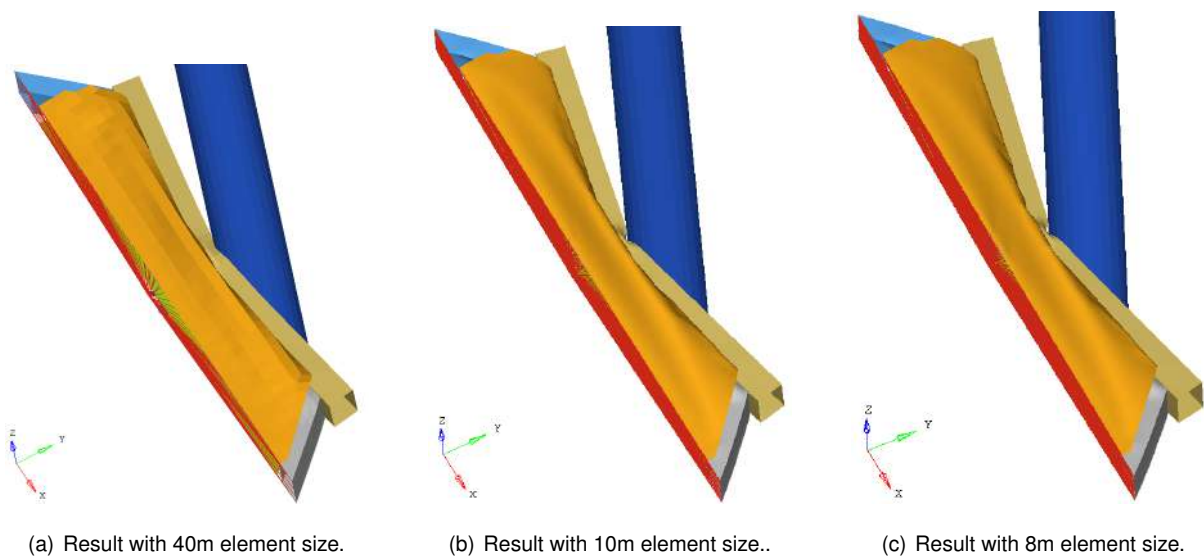


Figure 3.28: Results from mesh convergence study.

All things considered, the 10mm mesh is the largest mesh that allows accurate results and it is the chosen to perform the crash simulations.

3.5.2 Static Simulation

Static simulation is a linear analysis that is calculated by the method described in section 2.7.2. This analysis is less demanding than the explicit analysis when it comes to computational time effort as proven by figure 3.29(a).

The strategy in this mesh convergence study is the same as the one used in the previous section, refining the element size and evaluating the results convergence.

The analyzed results are maximum torsion, maximum displacement in Z and maximum Von Mises equivalent stress, as described in table 3.4.

Table 3.4: Results from mesh convergence study (static).

Element Size [mm]	Time [s]	Maximum Torsion [rad]	Maximum Displacement in Z [mm]	Von Mises [MPa]
40	21,39	0,00216	0,333	14,632
20	23,25	0,00216	0,334	17,183
15	24,25	0,00217	0,334	18,276
13	24,53	0,00217	0,334	18,950
12	24,75	0,00217	0,335	19,269
11	26,23	0,00218	0,335	19,899
10	26,9	0,00218	0,335	20,234
9	28,02	0,00218	0,335	20,318
8	30,69	0,00218	0,335	20,454

Graphically the results from table 3.4 can be observed in figure 3.29. In figures 3.29(b), 3.29(c) and 3.29(d) prove that only for 10mm element size the results converge, from where, more refinement of the mesh does not present a significant change of the results. Therefore, the 10mm mesh is the biggest mesh that allows accurate results. The smallest mesh studied, 8mm, only varies in the worst of the analyzed results 1.1% from the 10mm selected mesh. This relative error is found in the results of the maximum Von Mises equivalent stress.

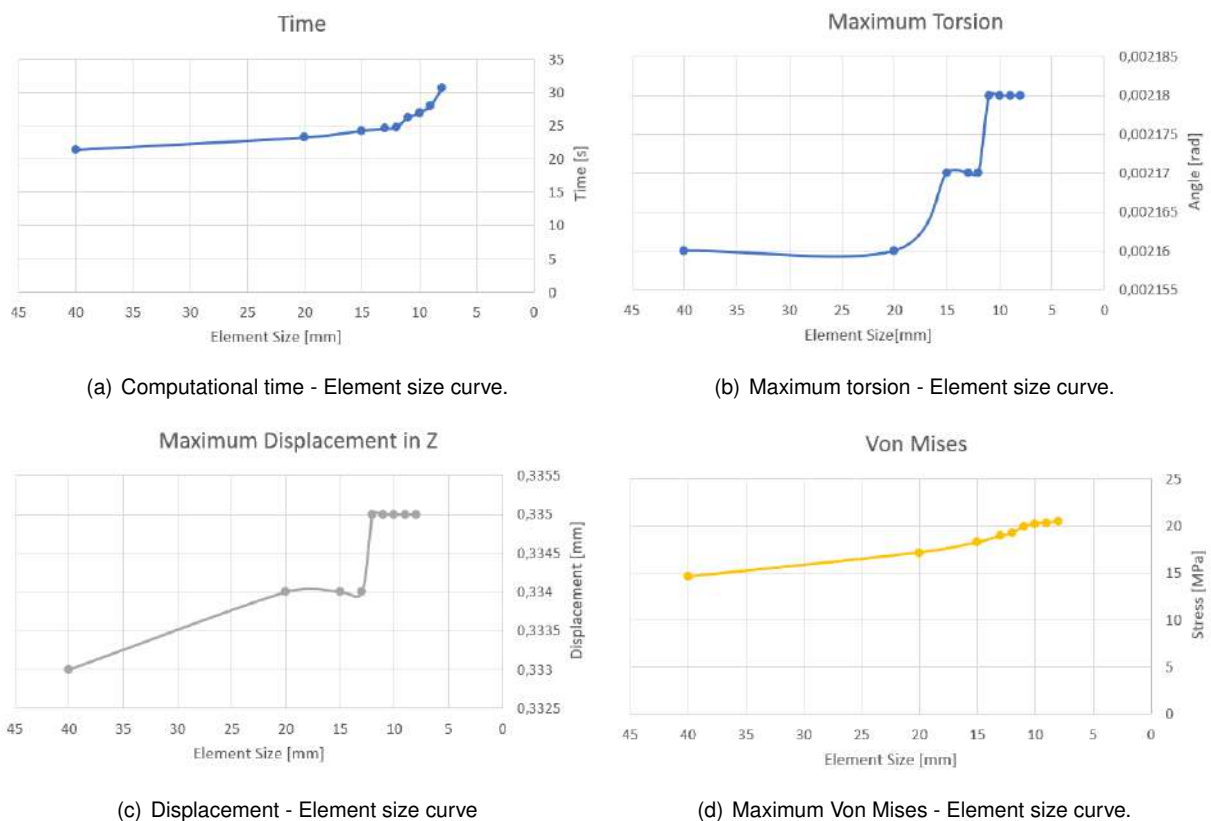


Figure 3.29: Curves from mesh convergence study (static).

3.6 Alignment Tests at 75° and 90°

The tests in this work are made with the structure motion forming an angle of 90° with the X-axis, parallel to the vehicle longitudinal centerline, to perform a more demanding test than the Euro NCAP pole test on the analyzed values.

According to Seo et al. [59], there is no significant difference between the force-time curve performing the test with the alignment at 75° or 90°. Seo et al. [59] performed the 90° alignment test with 29km/h and the 75° alignment test according to Euro NCAP pole test. It was concluded that testing the structure with the alignment according to the Euro NCAP pole test makes it more demanding at the level of abdomen and chest but less on the pubic zone measurements. The HIC_{15} does not show great differences in the two tests.

To test the influence of just the alignment in the present work, both tests were performed at 32km/h. Due to the early stage development of the Be2.0, it is still unknown where the passenger will go with certainty. Therefore, to perform the alignment according to the Euro NCAP pole test, it was considered that the head of the dummy is located at the ID1 node, the master node of the rigid body. In this test, the pole is not aligned with the structure, therefore, another consideration for this test was to apply a moment of inertia on the Z-axis, with the predicted value for the Be2.0 of 1300kg.m². The tested structure has the same shape and width than the one which was analyzed in section 3.5 but with a thickness of 6mm.

The differences between the two alignment tests can be observed in figures 3.30 and 3.31.



Figure 3.30: Result from 75° alignment test.



Figure 3.31: Result from 90° alignment test.

Comparing the two tests, it can be concluded that the test with 90 degrees of alignment is more demanding in all analyzed variables in this model, as observed in figure 3.32. This test is 7.08% more intrusive, has a HIC_{15} maximum 10.84% higher and a maximum acceleration 7.34% superior when compared with the 75° test,

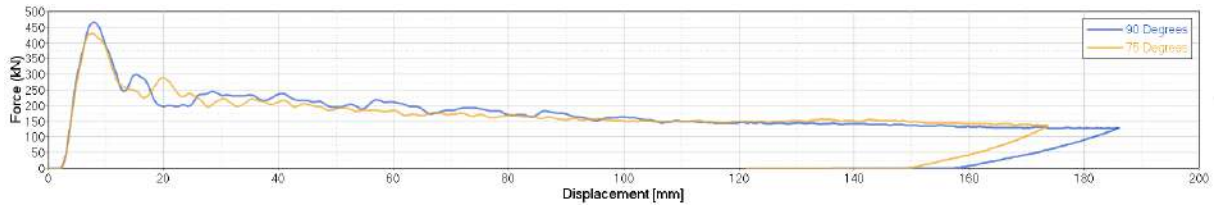


Figure 3.32: Force-displacement curves from the alignment test

Making the test more demanding is a strategy to better protect passengers and batteries in case of a crash event, as well as be one step ahead for future demanding changes in this type of tests, taking into account that Be2.0 has not yet a release date.

3.7 Effect of Auxiliary Structures

The goal of this work is the optimization of the side beam chassis, however, the crash test is performed with the auxiliary structures. To evaluate the importance of these structures, two tests were performed, one with structures and the other without, as observed in figures 3.33 and 3.34.

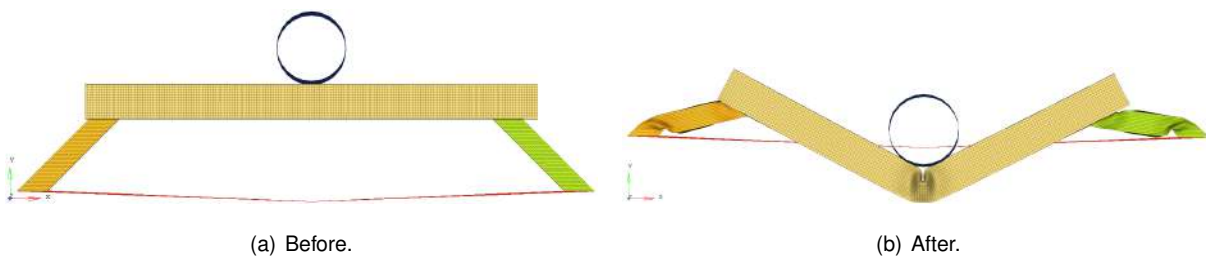


Figure 3.33: Model without auxiliary structures.

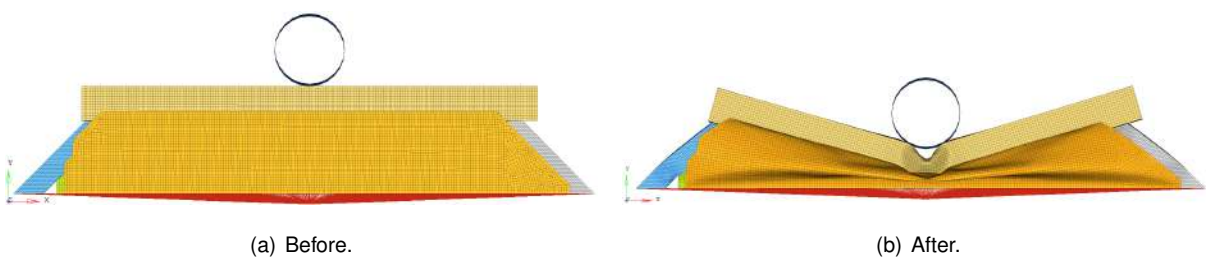


Figure 3.34: Model with auxiliary structures.



Figure 3.35: Force-displacement curves for effect of auxiliary structures

It would make sense to just study the beam, because we would decrease computational time about 54%. However, based on figure 3.35, if we optimize the beam without the auxiliary structures we would find problems. First, we would oversize the beam in order to meet the intrusion requirements. Consequently, when the beam was assembled with the car we would get a higher peak of force. It is what happens when the structures are assembled to the beam, the peak appears associated with a smaller intrusion.

All things considered, if we want to approximate the model to the real case, it only makes sense to optimize the beam with auxiliary structures.

Chapter 4

Experimental Study and Validation

Due to lack of equipment, material and resources, these experimental validations were not done. However, this chapter discusses how the experimental tests should be performed.

4.1 Material Model

Before testing the whole structure in a laboratory, it is important to make sure if the materials used in these tests have the correspondent behavior of the material modeled in the computational material model. With material samples from the same materials that will be used to construct the components of the structure, it is possible to perform tensile tests. These tests can validate if the structure is being constructed according to what was designed computationally. The two aluminum alloys used in this project must be tested in this experimental study.

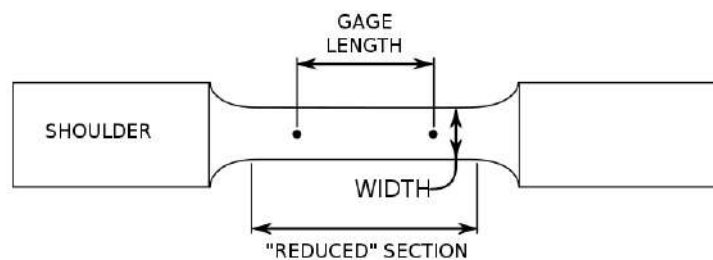


Figure 4.1: Typical tensile specimen.

These samples should be cut as shown in figure 4.1. The cross-sectional area of the gage section must be smaller than the rest of the sample, in order to the deformation and subsequent rupture to occur in this region. It is very important that the gage length be centered with the reduced section, the gage length be large relative to its width, and the distance between the end of the gage section and the shoulders be large. Otherwise, we can have a stress state more complex than simple tension. [60]

To test the samples, we need a machine. The universal testers are the machines most used to perform this type of tests. Specialized in obtaining stress-strain curves, these hydraulic machines are based on a piston that moves the crosshead up or down. This type of machine is outlined in figure 4.2.

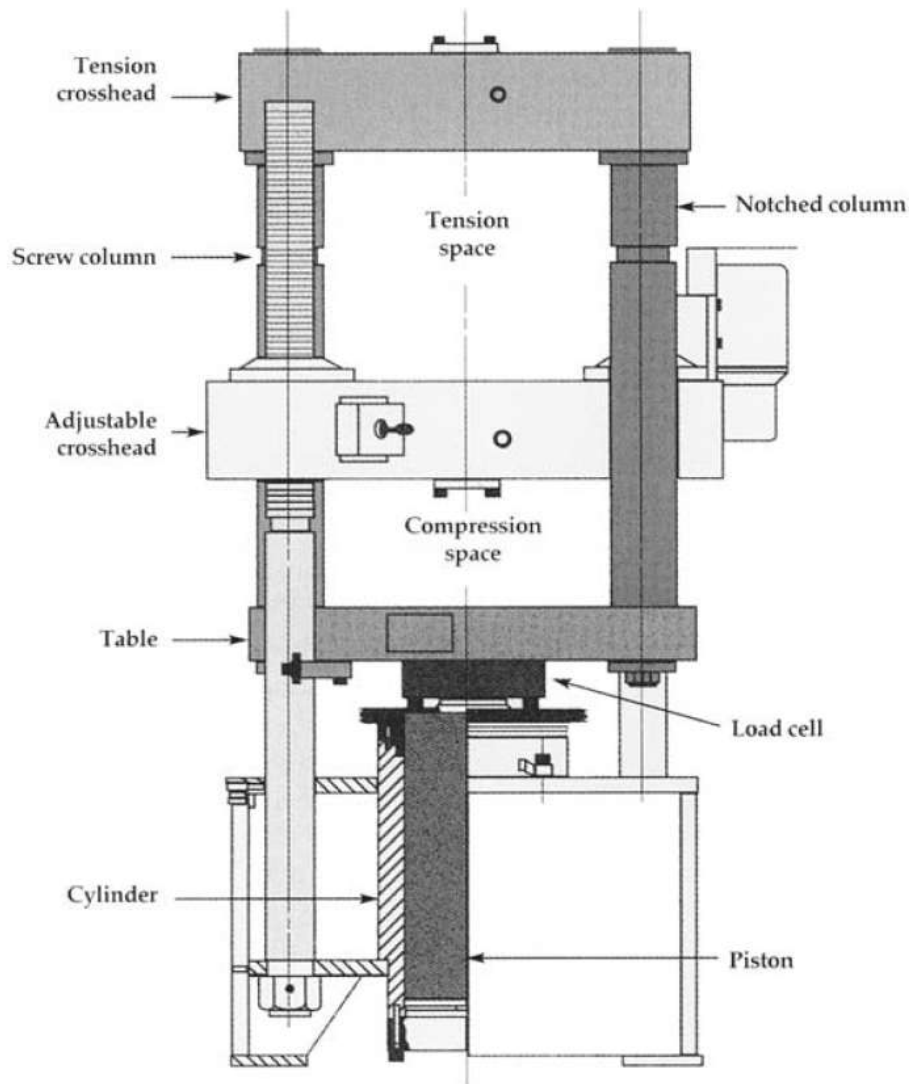


Figure 4.2: Universal hydraulic testing machine [60].

This machine reads the tensile force as a function of the increase in gage length, therefore, to obtain the stress-strain curve we must normalize the data with respect to the sample dimensions. In order to obtain more accurate results, it is important to test several samples of each material and, with these data, calculate a weighted average of all stress-strain curves for each material.

4.2 Crash Model

In order to validate the crash numerical model, first we need to construct the structure. The structure components are outlined in figure 4.3. All 2D drawing CADs, materials and manufacturing procedures from all structure components can be consulted in appendix C. The force-displacement curve from this structure can be consulted in figure 3.35 because this structure is the same as the one used in section 3.7.

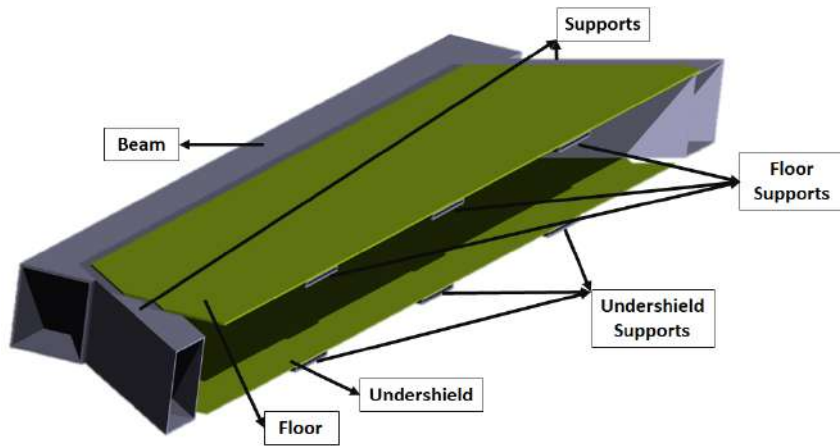
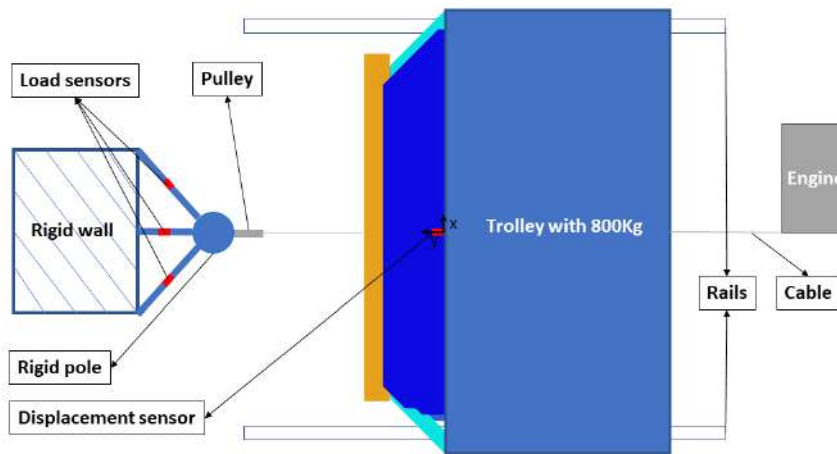


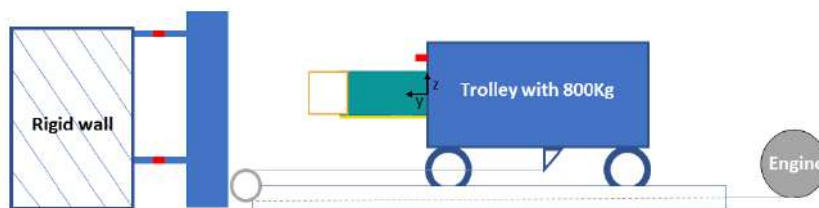
Figure 4.3: Render of the structure with the components outlined.

It is very important that the activation, the monitoring and the data collection be performed fully automatic to not have people near the structure at the impact moment and, thus, execute the laboratory test safely.

We need a trolley with a mass of 800Kg. The front of the trolley must be welded with the structure, in order to simulate the rigid body. The center of gravity of the trolley must be aligned with the plane $x = 0$, in an effort not to produce unwanted moments. The trolley moves in two rails, with this strategy, the trolley will just move in the Y direction.



(a) Top view.



(b) Side view.

Figure 4.4: Experimental crash test layout.

The traction system is composed by an electric motor, a pulley and a cable. The position layout of these components are shown in figure 4.4. The impact must occur with a target speed of $32\pm 0.5\text{km/h}$, this speed must be reached 10m before the contact and achieved with an acceleration lower than 1.5m/s^2 . Before the collision with the pole, the motor must be automatically switched off. The speed control and the engine switched off instant, must be controlled by a feedback system that the engine has attached to itself.

The pole is a circular metallic rigid structure with $354\pm 3\text{mm}$ in diameter, that begins at a maximum of 102 mm above the lowest point of the trolley's wheels, and ends at least 100mm above the highest point of the structure.

We must have 6 load sensors on the pole's supports. These sensors must have a capacity to measure forces above the peak of 320.9kN, as observed in figure 3.35. The force-time curve will be the sum of the curves from the two sensors aligned with the pole, adding the contributions of the remaining 4 sensors. Every contribution must be multiplied by the sine of the respective angle between the support and the rigid wall. This curve must be filtered according to section 3.4.5.

The displacement sensor must be placed in the plane $y = 0$, in order to be faithful with the computational model and to extract the displacement-time curve.

Finally, we can merge the force-time curve with the displacement-time curve and get the force-displacement curve. The force-displacement curve of the computational model is shown in figure 3.35. To validate the computational model, these curves must be approximately equals.

4.3 Static Model

Due to the early stage development of the Be2.0, the load application points of the cabin in the beam are not yet known. Therefore, a pressure was applied throughout the upper part of the beam to simulate the bending effect, that it would be subjected during vehicle's operation. To simulate the worst case scenario, in the previous model, the maximum moment that the beam has to support was applied, in order to contribute to the global torsional stiffness of Be2.0. However, with these combined loads such experimental test is not possible to perform in a laboratory [61].

Chapter 5

Results

The results obtained with the developed tool presented in chapter 3 are analyzed in the present chapter. In this chapter are presented the strategies used in the five different optimizations, as well as their results. At the end, an analysis based on the realized optimizations is made and a final solution to meet the objectives of this project is presented.

5.1 Optimization 1 - Rectangular Shape

This first optimization is the most simplistic approach where the goal is to optimize the rectangular shape beam. Therefore, a *CATIA™ V5* 3DCAD model with a parameterized rectangular shaped beam in width and thickness is given to the optimization cycle.



Figure 5.1: Structure front view with a rectangular shape

The main parameters given to the genetic algorithm of this optimization cycle are presented in table 5.1.

Table 5.1: Parameters of optimization 1.

Parameter		Units
Variables	Width, Thickness	mm
Upper Bound	[120 10]	mm
Lower Bound	[60 2]	mm
Function Tolerance	0.005	-
Population Size	9	-
Max Generations	50	-
Max Stall generations	3	-
Crossover Fraction	0.8	-
Plot Functions	@gaplotdistance	-

The upper and lower limits of the width are created just following the project requirements but, in the case of thickness, the programmer's sensibility and experience is fundamental. Setting upper and lower limits as close as possible is very important for computational time since the search region decreases and the algorithm will converge faster. The Plot Functions plots data computed by the algorithm, in this case, the @gaplotdistance plots the average distance between the individuals at each generation. The Crossover fraction is set to be 0.8, therefore, 80% of the child population is created by the crossover function. This leaves 20% to be formed by mutation, important to maintain the variability of the population. The Max Stall Generations, Max Generations and the Function tolerance defines the stopping criteria as explained in section 2.8.2.

This optimization stopped after about 12 days, and the results, as well as their force - displacement curves are shown in figure 5.2. Observing figure 5.2 can be concluded that the algorithm searched in all region with except of the low width and thickness zone. This is not a problem because this is a zone of infeasible solutions due to its high intrusion. It can be concluded as well, that the algorithm converged in a region where several identical individuals were calculated.

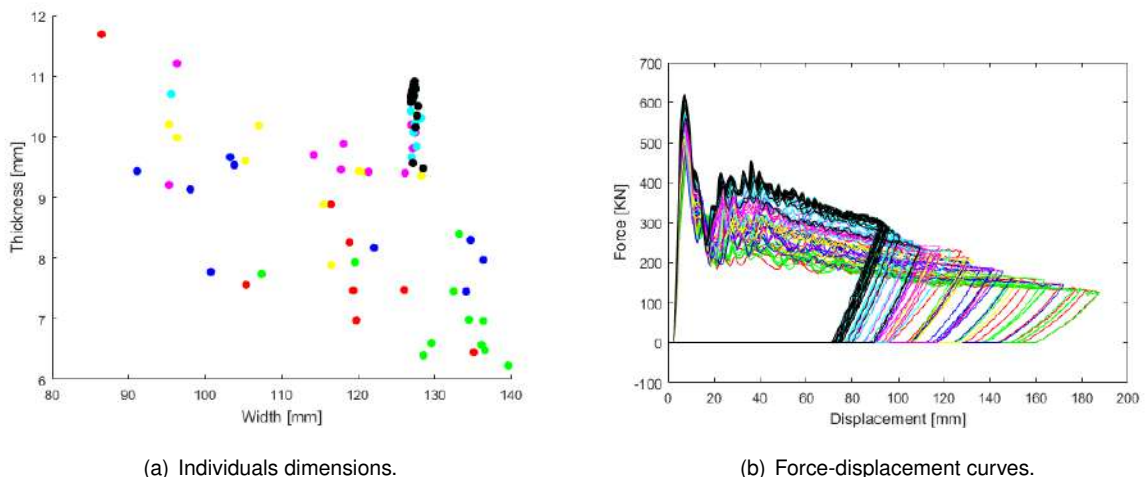


Figure 5.2: Optimization 1 individuals and force - displacement curves.

In figure 5.3, all values of the objective functions for each one of the individuals tested are presented. The individuals painted in green satisfy the constraints imposed by this project. While the individuals painted in red color do not satisfy at least one constraint.

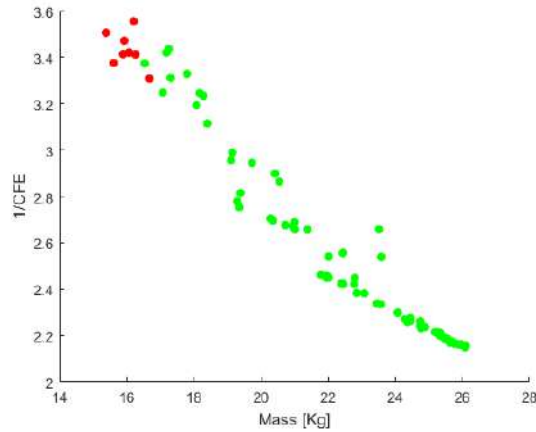


Figure 5.3: Objective functions results.

This first optimization performed was to test the method. The beam width was allowed to change to be optimized. The beams with higher widths have an advantage in relation to the narrower beams, because they allow a greater displacement with less intrusion. At the end of this optimization it was concluded that the intrusion would be the constraint that would reprove more individuals. It can also be concluded, that the CFE increase is only achieved by increasing the mass, proving the competitiveness between the objective functions. In this optimization, individuals that fulfilled all constraints were obtained, however presented mediocre crash performance. The lightest beam that was able to overcome all constraints, obtained in this optimization, has a mass of 16.54kg. On the other hand, the beam with the best crash performance has a CFE of 0.464 but presents a mass increase of 57.9%, in relation to the lightest beam.

With only 2 parameters being optimized, the method stops after 12,2 days of computation. All this time in a single optimization is not feasible to develop a component in an engineering center or to perform more simulations in the time available to execute this project.

According to figure 5.4, from generation four onwards the distance between individuals is almost zero. The individuals in these generations practically only varied by a tenth of a millimeter. Many individuals almost equal to each other were simulated, therefore computation time was wasted without adding value to the optimization.

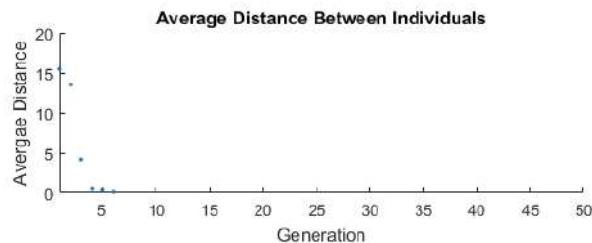


Figure 5.4: Average distance between individuals at each generation.

Conclusively, it is imperative to adopt strategies for reduction of computational time in the following optimizations.

5.2 Optimization 2 - Aligned Quadricular Shape

In this second optimization, the goal is to optimize a quadricular shape beam. Now three variables are optimized by giving a CATIA™ V5 3DCAD model with a parameterized quadricular shaped beam in the thickness, divisions in height and divisions in width to the optimization cycle. All optimizations hereafter were carried out with a beam's width of 130 mm, a target value for the maximum width of the Be2.0.



Figure 5.5: Structure front view with 4 divisions in height and width.

The change in the algorithm to only allow integer values in the variables is another major difference from optimization 1 to optimization 2. This is possible by making a small change in the outputs of the mutation and crossover function, individuals are rounded to allow only integer values. This strategy forces the search region to be greatly reduced. Another great advantage is the probability of repeated individuals formed by crossover or mutation increase drastically. As mentioned in chapter 3, repeated individuals are only calculated once by passing their previously data to the algorithm. With this strategy, the convergence of the algorithm is faster and precious computational time is saved.

The main parameters given to the genetic algorithm are presented in table 5.2.

Table 5.2: Parameters of optimization 2.

Parameter		Units
Variables	Height Divisions, With Divisions, Thickness	-, -, mm
Upper Bound	[2 2 1]	-, -, mm
Lower Bound	[9 9 5]	-, -, mm
Function Tolerance	0.005	-
Population Size	9	-
Max Generations	50	-
Max Stall generations	3	-
Crossover Fraction	0.8	-

Another change is made in this optimization, instead of the initial population being randomly created, in this optimization a function that contains it its given to the algorithm. This is another strategy to a faster convergence of the algorithm by using the sensitivity of the programmer to know where the best solutions may be found. In addition, it is important that the initial population covers the entire search region in order to ensure sufficient initial variability. The individuals that form the initial population are the ones presented in table B.1 in appendix B.

This optimization stopped after about 3 days and the results, as well as all their force - displacement curves are shown in figure 5.6.

In this optimization an initial population was given to the algorithm therefore, the initial variability was assured by the programmer. But by looking at figure 5.6, it can be concluded that rigid structures and others that allow a big intrusions were tested. However, the majority of the curves lie on the intrusion limit zone where the CFE and mass can be maximized and minimized respectively.

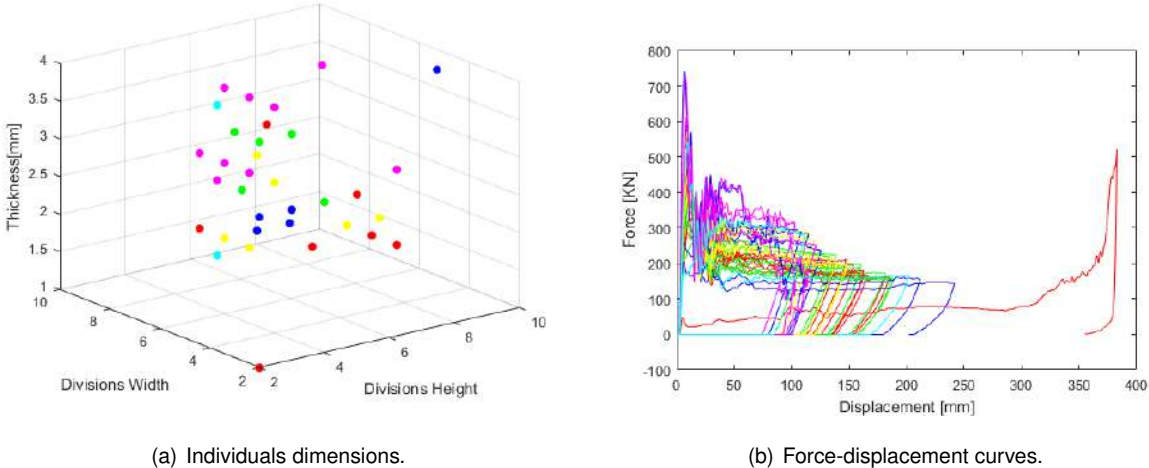


Figure 5.6: Optimization 2 individuals and force - displacement curves.

In figure 5.7, all values of the objective functions for each one of the individuals tested are presented. The individuals painted in green satisfy the constraints imposed by this project. While the individuals painted in red color do not satisfy at least one constraint.

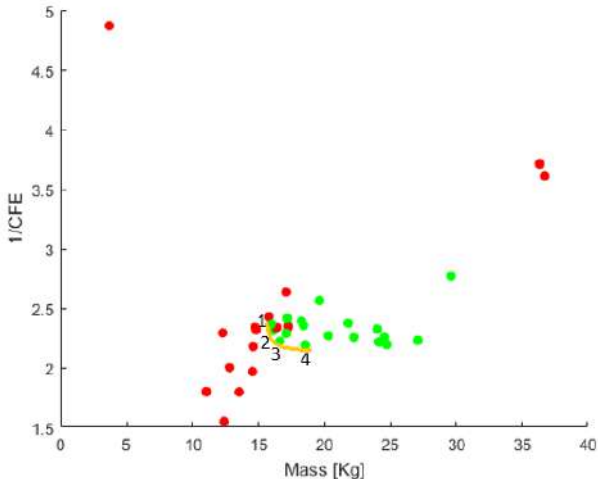


Figure 5.7: Objective functions results from optimization 2.

Analyzing these results is easily noticeable that 4 individuals lie on the pareto front, represented in figure 5.7 by a yellow line. These individuals, enumerated from 1 to 4. Their results can be seen in table 5.4, and their force-displacement curves are presented in figure 5.8. Table 5.3 helps to interpret table 5.4 relating their indexes.

Table 5.3: List of indexes.

	Divisions Height	Divisions Width	Thickness1	Thickness2	
Individual	x(1)	x(2)	x(3)	x(4)	
Dynamic	CFE	Mass	Max. HIC_{15}	Max. G's	Intrusion
	y(1)	y(2)	c(1)	c(2)	c(3)
Static	Max. Displacement Z	Max. Torsion	Max. Von Mises Equivalent Stress		
	[mm]	[rad]	[MPa]		
	c(4)	c(5)	c(6)		

Table 5.4: Results from optimization 2.

Individual	x(1)	x(2)	x(3)	y(1)	y(2)	c(1)	c(2)	c(3)	c(4)	c(5)	c(6)
1	5	6	2	0.422	16	67.81	53.84	140.54	0.28	0.0042	12.22
2	4	7	2	0.433	16.091	62.47	50.09	147.62	0.31	0.0043	14.15
3	3	4	3	0.450	16.635	58.25	45.95	149.35	0.37	0.0047	17.89
4	3	5	3	0.456	18.545	71.69	49.11	137.67	0.36	0.0043	17.01

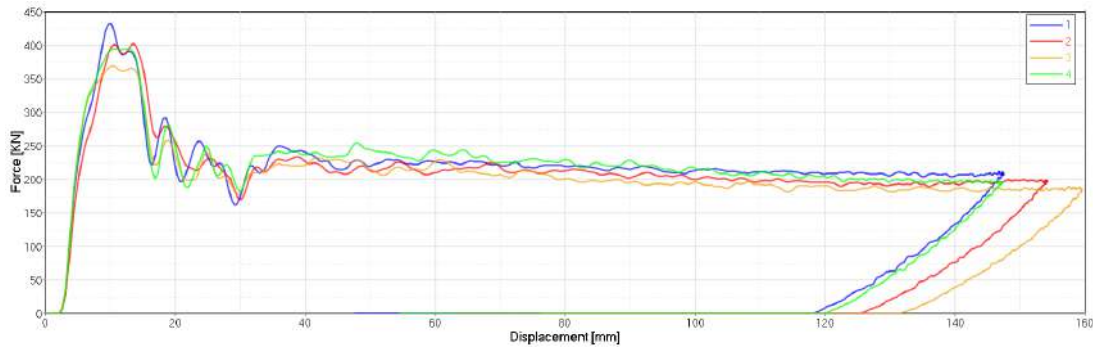


Figure 5.8: Force-displacement curves from optimization 2 pareto front individuals.

Since optimization 1 onwards, all optimizations were performed following the strategy that a higher deformation in the beam would lead to a higher energy absorption in a lower displacement. A smaller displacement will lead to less intrusion. On the other hand, a higher deformation in the beam width zone will lead to a higher displacement, without this implying a same magnitude increase in the intrusion of the beam towards the interior of the vehicle.

The implemented strategy was a success, the quadricular shaped beam lead to an increase of the CFE to any corresponding value of mass in optimization 1. Therefore, the individuals from optimization 2 dominate almost all optimization 1 individuals. However, the improvements obtained in the optimization 2 are insufficient. The pareto front individuals of this optimization still present a high peak force in relation to the average force, the individual with the best performance in crash presents only a CFE of 0.456.

5.3 Optimization 3 - Misaligned Quadricular Shape

In this third optimization, the goal is to optimize a quadricular shape beam with the squares misaligned half their size as shown in figure 5.9. This type of beam follows the strategy that more deformation, more

energy is absorbed, hence its misaligned form. It is expected that the vertical reinforcements of this type of beams deform more than those of optimization 2.

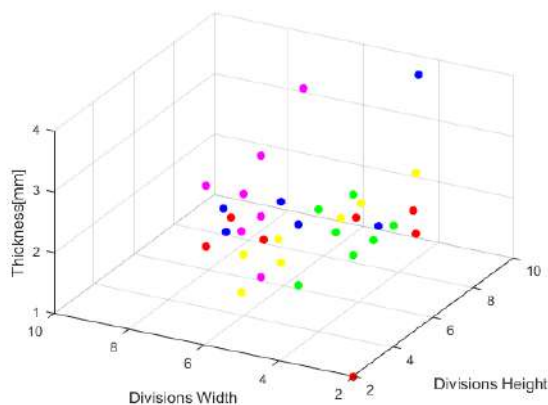


Figure 5.9: Structure front view with 2 divisions in height and width.

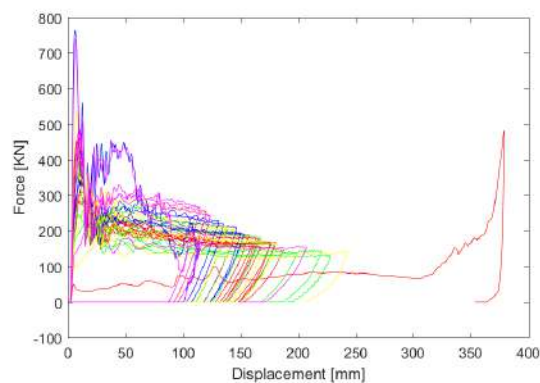
In this section, three variables are optimized, therefore a *CATIA™ V5* 3DCAD model is given to the optimization cycle with a quadricular shaped beam with the squares misaligned half their size parameterized in the thickness, divisions in height and divisions in width.

Similar to optimization 2, the same strategy of only using variables with integer values is used. The main parameters given to the genetic algorithm are the same as those in the previous optimization presented in table 5.2. One difference from the previous optimization, is the way the beam is parameterized. However, the two optimization present the same variables, divisions in height, divisions in width and thickness.

Following the strategy described before, the initial population presented in table B.2 in appendix B was provided to this optimization. This optimization stopped after 3 days and the results, as well as all their force-displacement curves are shown in figure 5.10. In this optimization an initial population was given to the algorithm therefore, the initial variability was assured by the programmer. But by looking at figure 5.10, it can be concluded that rigid structures and others that allow a big intrusions were tested. However, the majority of the curves lie on the intrusion limit zone where the CFE and mass can be maximized and minimized respectively.



(a) Individuals dimentions.



(b) Force-displacement curves.

Figure 5.10: Optimization 3 Individuals and force-displacement curves.

In figure 5.11, all values of the objective functions for each one of the individuals tested are presented.

The individuals painted in green satisfy the constraints imposed by this project. While the individuals painted in red color do not satisfy at least one constraint.



Figure 5.11: Objective functions results from optimization 3.

Analyzing these results, it is easily noticeable that three individuals dominate the others. Therefore, they lie on the pareto front, represented in figure 5.11 by a yellow line. These individuals are enumerated with 1, 2 and 3. Their results can be seen in table 5.5, and their force-displacement curves are presented in figure 5.12. Table 5.3 helps in the interpretation of table 5.5 by relating their indexes.

Table 5.5: Results from optimization 3.

Individual	x(1)	x(2)	x(3)	y(1)	y(2)	c(1)	c(2)	c(3)	c(4)	c(5)	c(6)
1	2	4	3	0.497	15.750	47.00	37.21	145.71	0.50	0.0040	23.78
2	4	7	2	0.519	16.597	52.74	38.5	140.55	0.55	0.0048	26.13
3	2	5	3	0.619	17.483	49.55	37.73	135.65	0.46	0.0038	22.13

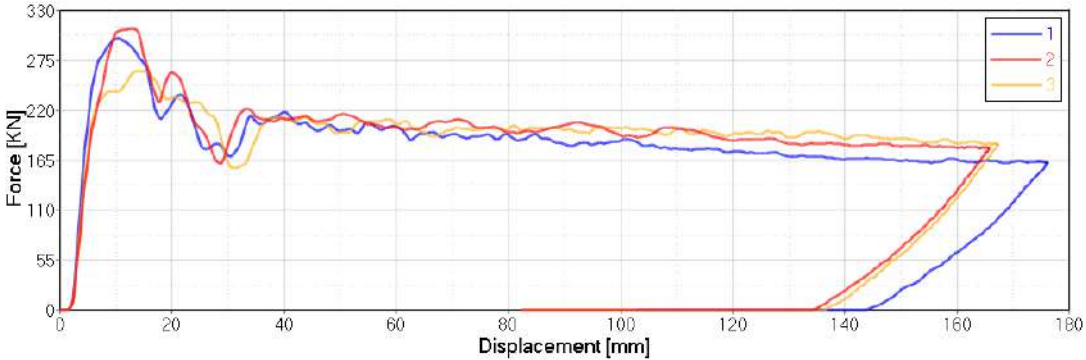


Figure 5.12: Force-displacement curves from optimization 3 pareto front individuals.

With the objective of decreasing the peak force and obtaining more deformation in the beam width zone, the strategy of having a quadricular shape beams with the squares misaligned half their size was implemented in this optimization. Here, the lightest beam that can overcome all constraints among all optimizations was obtained, its mass is 15.75kg. In addition to be the lightest, this individual has a

CFE of 0.497. Better than any CFE presented in optimization 2, therefore this individual dominates all individuals from optimization 2. The solution 3 of the pareto front from this optimization presents a CFE of 0.619 for a mass of 17,48kg. This is the best CFE found so far. Simply by increasing its mass by 11% the CFE was raised by 25%, when compared to the lightest beam.

5.4 Optimization 4 - Aligned Quadricular Shape With First Width Division Thicker

In this fourth optimization, the goal is to optimize a quadricular shape beam with the thickness in the first width division different from the rest of the beam. This type of beam follows the strategy that more deformation, more energy absorbs. Hence, the zone of the beam with smaller thickness will always crash with the pole (exterior beam zone) and never be equal to the inner thickness, as shown in table 5.6. Allowing them to be equal would only allow the program to search in the region where optimization 2 already did and consequently, waste computational time. The constraint in intrusion has been where the structures most fails until here. Therefore, this solution intends to mitigate the intrusion with a thicker division in the inside part of the beam. This larger thickness is placed in the first beam width division to increase the force after the peak, in an effort to increase the CFE. This larger thickness division acts as a "barrier" to intrusion and give the sufficient stiffness in the static test. At the same time, with the divisions of smaller thickness in contact with the pole, we can reduce the initial peak force and reach higher deformations and, consequently, a higher energy absorption with smaller intrusion.

In order to do this optimization, it was necessary to make some changes in the *HYPERMESH*[®] macros for crash and static simulation. In the *HYPERMESH*[®] macro, for the static simulation, only two changes were performed. The first one was to create a new component because we can not have two different thicknesses in the same component. Therefore, the beam was divided into two components. All the elements of the first width division of the beam now corresponds to this second component. The same material is attributed to this new component. The second change was to create a new property to allocate this new thickness. This property was created as explained in section 3.4.6 and attributed to this new beam's component.

In the *HYPERMESH*[®] macro for the crash simulation, the same changes as those in the static simulation macro were performed. The reason was the same, two different thicknesses in the same component. The new property in this case was created as explained in section 3.4.3. The connections, now in the region of the new component, are attributed to it. To simulate the contact with the others components and the contact itself, this new component is added to the general surface-to-surface contact interface group *TYPE24*, as explained in section 3.4.3. The output block that exports the mass of the beam is also changed, now starts exporting the mass of the two components of the beam. The *HYPERGRAHP*[®] session file was saved with the third curve being the sum of the two components mass curves in order to the *HYPERGRAHP*[®] macro exports the correct value of the beam's total mass into to the *.cvs* format file. The *MATLAB*[®] script also suffers some small changes to cope with these updates

in the cycle.

The red and green color of the beam in figure 5.13 represents the component with bigger thickness in the static and crash model respectively.

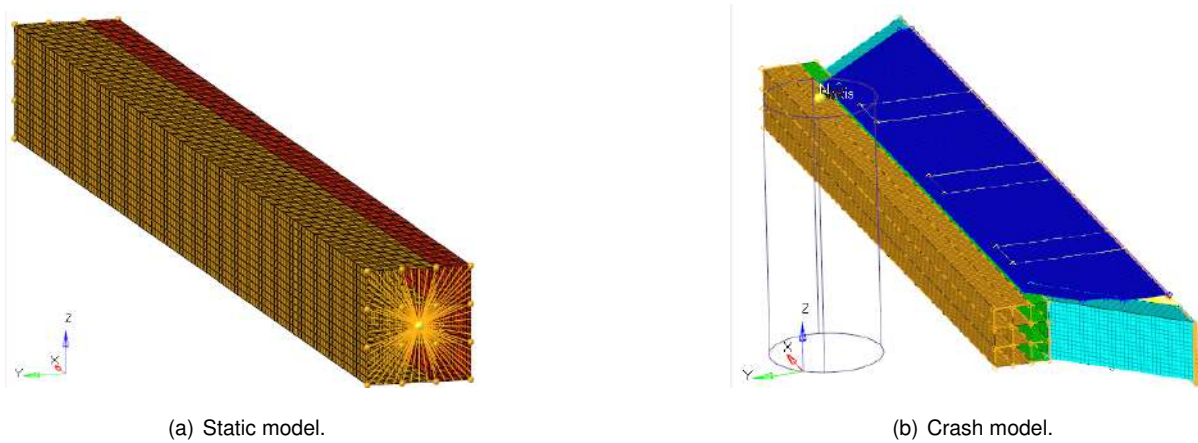


Figure 5.13: Quadricular shape beam with the thickness in the first width division different from the rest of the beam.

The beam to be optimized in this section is the same of the optimization 2, with the difference of the new thickness. The variables to be optimized are four: divisions in height, divisions in width, thickness1 and thickness2 (from the first width division).

Similar to optimization 2, the same strategy of only using variables with integer values is used. The main parameters given to the genetic algorithm are presented in table 5.6.

Table 5.6: Parameters of optimization 4.

Parameter		Units
Variables	Height Divisions, With Divisions, Thickness1, Thickness2	-, ,mm,mm
Upper Bound	[2 2 1 4]	-, ,mm,mm
Lower Bound	[9 9 3 9]	-, ,mm,mm
Function Tolerance	0.005	-
Population Size	9	-
Max Generations	50	-
Max Stall generations	3	-
Crossover Fraction	0.8	-

Following the strategy described in optimization 2, the initial population presented in table B.3 in appendix B was provided to this optimization. This optimization stopped after 4 days and the results, as well as their force-displacement curves are shown in figure 5.14.

Analyzing figure 5.14, can be concluded that rigid structures and others that allow a big intrusions were tested. However, the majority of the curves lie on the intrusion limit zone where the CFE and mass can be maximized and minimized respectively. The high density of curves in this region proves the programmer's good sensibility in the initial population and the convergence of the method.

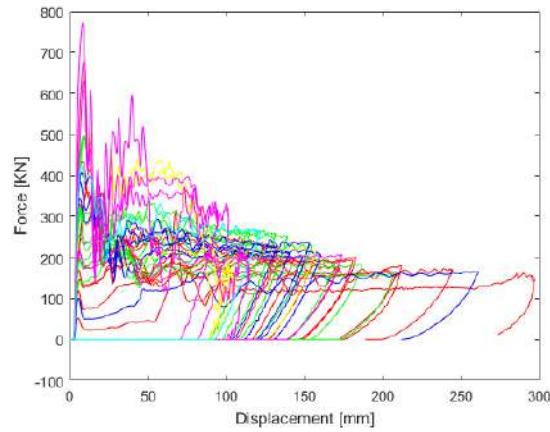


Figure 5.14: Force-displacement curves from optimization 4.

In figure 5.15, all values of the objective functions for each one of the individuals tested are presented. The individuals painted in green satisfy the constraints imposed by this project. While the individuals painted in red color do not satisfy at least one constraint.

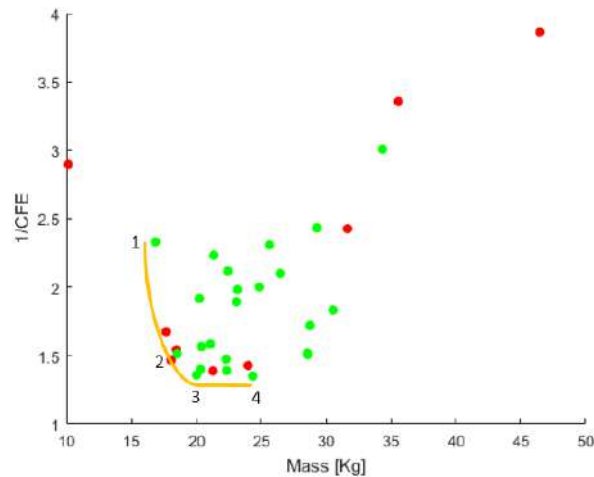


Figure 5.15: Objective functions results from optimization 4.

Analyzing these results, it is easily noticeable that four individuals dominate the others. Therefore, they lie on the pareto front, represented by a yellow line in figure 5.15. These individuals are enumerated with 1, 2, 3 and 4. Their results can be seen in table 5.7, and their force-displacement curves are presented in figure 5.16. Table 5.3 helps in the interpretation of table 5.7 relating their indexes.

Table 5.7: Results from optimization 4.

Individual	x(1)	x(2)	x(3)	x(4)	y(1)	y(2)	c(1)	c(2)	c(3)	c(4)	c(5)	c(6)
1	8	8	1	4	0.429	16.857	46.44	44.44	126.41	0.61	0.0050	20.88
2	3	4	2	6	0.661	18.546	35.18	28.08	147.85	0.47	0.0036	25.96
3	4	3	2	6	0.736	20.027	43.16	26.56	138.60	0.23	0.0033	15.38
4	4	4	2	8	0.740	24.339	31.28	65.71	122.2	0.40	0.0031	22.84

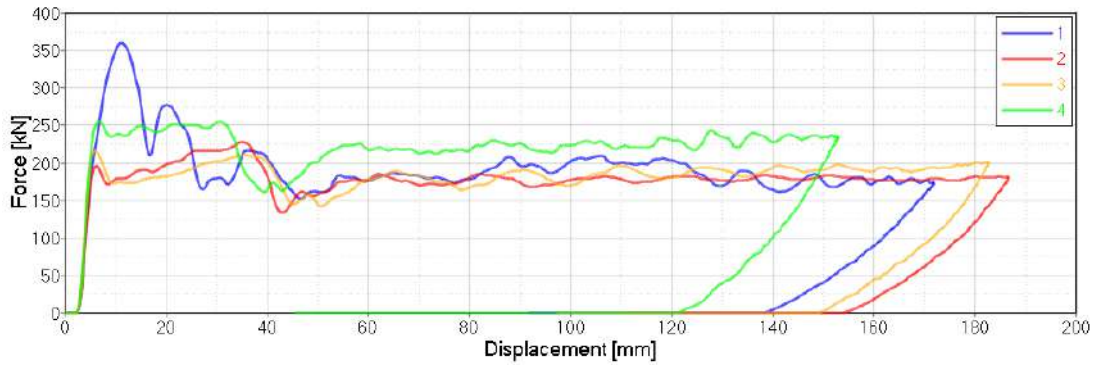


Figure 5.16: Force-displacement curves from optimization 4 pareto front individuals.

In this optimization, this multi-thickness strategy to the aligned quadricular shape beam was applied. As we can see there was an improvement in CFE in relation to the same beam without this applied strategy (optimization 2). We can observe that individuals 2, 3 and 4 practically do not present a peak of force in their curves shown in figure 5.16. This improvement was always followed by a mass increase. The lighter individual found in this optimization is dominated by the optimization 2 individuals.

5.5 Optimization 5 - Misaligned Quadricular Shape With First Width Division Thicker

In this fifth optimization, the goal is to optimize a quadricular shape beam with the squares misaligned half their size as shown in figure 5.9, but applying the strategy from the optimization 4. The thickness in the first width division is different from the rest of the beam. The variables to be optimized will be four: divisions in height, divisions in width, thickness1 and thickness2 (from the first with division).

Similar to optimization 2, the same strategy of only using variables with integer values is used. The main parameters of the genetic algorithm in this optimization are the same as previous ones, presented in table 5.6.

Following the strategy described in the optimization 2, the initial population presented in table B.4 in appendix B was provided to this optimization. This optimization stopped after 4 days and the results, as well as their force-displacement curves from the performed simulations are shown in figure 5.17.

Analyzing figure 5.17, can be concluded that rigid structures and others that allow a big intrusions were tested. However, the majority of the curves lie on the intrusion limit zone where the CFE and mass can be maximized and minimized respectively. It can be concluded as well, that this zone with more curve density appears associated to a greater displacement when compared with figure 5.14, this proves that these structures allow a bigger displacement for the same intrusion. The high curve density in this region proves as well, the programmer's good sensibility in the initial population and the convergence of the method.

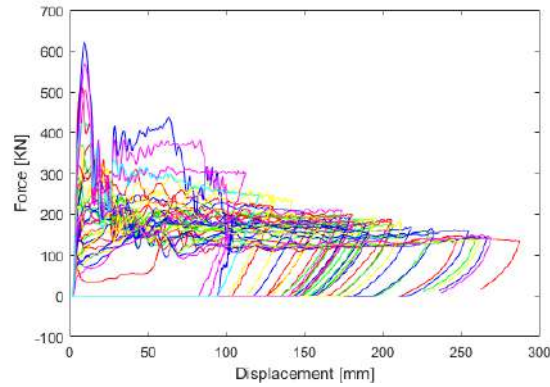


Figure 5.17: Force-displacement curves from optimization 5.

In figure 5.18, all values of the objective functions for each one of the individuals tested are presented. The individuals painted in green satisfy the constraints imposed by this project. While the individuals painted in red color do not satisfy at least one constraint.

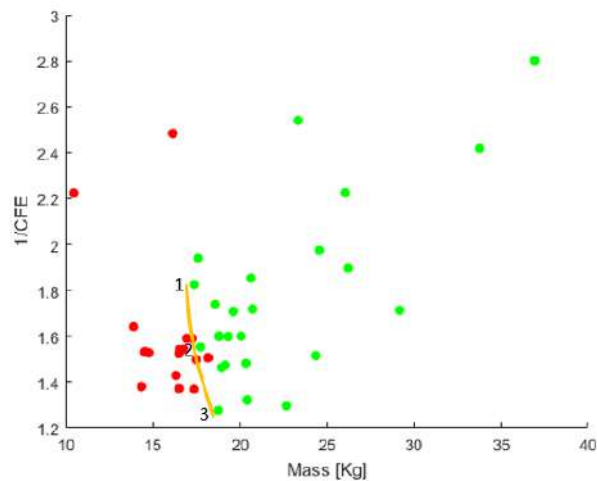


Figure 5.18: Objective functions results from optimization 5.

Analyzing these results, it is easily noticeable that three individuals dominate the others. Therefore, they lie on the pareto front, represented by a yellow line in figure 5.18. These individuals are enumerated with 1, 2 and 3. Their results can be seen in table 5.8, and their force - displacement curves are presented in figure 5.19. Table 5.3 helps in the interpretation of table 5.8 relating their indexes.

Table 5.8: Results from optimization 5.

Individual	x(1)	x(2)	x(3)	x(4)	y(1)	y(2)	c(1)	c(2)	c(3)	c(4)	c(5)	c(6)
1	3	3	3	4	0.548	17.376	50.68	37.05	148.92	0.44	0.0031	23.25
2	2	6	2	5	0.644	17.753	37.86	28.97	142.47	0.47	0.0039	23.50
3	2	2	2	7	0.784	18.748	35.14	22.63	149.58	0.45	0.0029	28.61

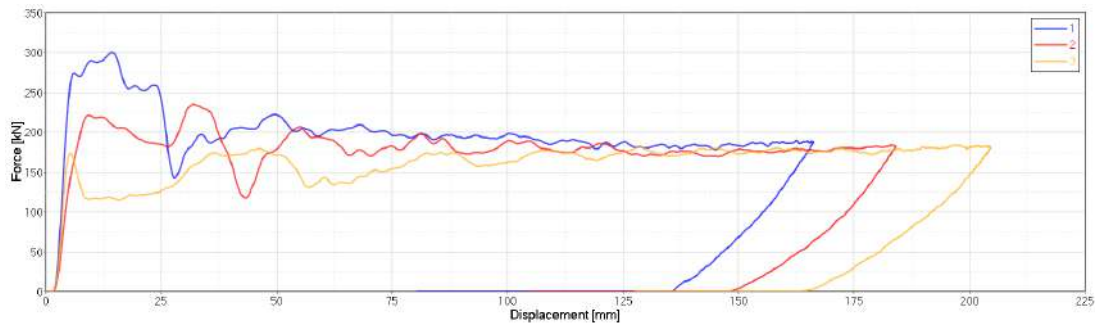


Figure 5.19: Force-displacement curves from optimization 5 pareto front individuals.

In this optimization it was applied the multi-thickness strategy to the misaligned quadricular shape beam. Comparing to optimization 4, the same behavior was observed in the results. The improvement in crash performance was always followed by a mass increase, in relation to the optimization 3 individuals. We can observe that individuals 2 and 3 practically do not present a peak of force in their curves shown in figure 5.19. Here, the beam with the best crash pole performance that can overcome all constraints among all optimizations was obtained, its CFE is 0.784. However, is the third heaviest beam when compared with the pareto fronts individuals of the last 4 optimizations.

5.6 Final Results

In the figure 5.20 all the pareto fronts of the optimizations are combined into one for an easier comparison of the different strategies and to choose a final solution for this work. This final pareto front is formed by individuals that are numbered from 1 to 7.

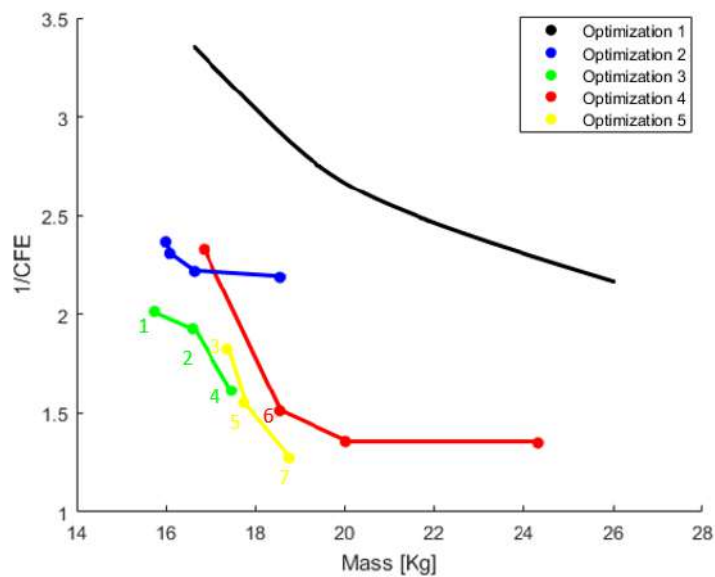


Figure 5.20: Final pareto front.

Comparing the pareto fronts, we can conclude that all applied strategies presented better results than

just rectangular shape beams, even allowing the variation of their width. We can also conclude by comparing the pareto fronts from the optimization 2 and 3 and from optimization 4 and 5 that the beams with the misaligned quadrangular shape dominate almost all aligned quadrangular shape ones. It is possible to conclude as well, that the strategy of forcing the first beam width division to be thicker always presented heavier results. However, with a substantial improvement in crash performance comparing aligned with aligned quadrangular shape beams and misaligned with misaligned quadrangular shaped beams.

The non-dominated individuals are numbered in figure 5.20 from 1 to 7. If the objective was to obtain the lightest beam or the highest CFE we should choose the beam 1 or 7 respectively. But the goal here, is obtain the best balance between the two objective functions. Therefore, the final solution will be beams 2, 3, 4, 5 or 6.

Although individual 2 (CFE=0.519, mass=16.60kg) is 6.5% lighter than individual 4 (CFE=0.619, mass=17.48Kg), if we compare the crash performance, individual 4 presents an increase in CFE of about 19%. The same happens with individual 3 (CFE=0.548 mass=17.38kg). For almost the same mass, individual 4 presents an increase in CFE of about 11.5%. Individual 4 is also less intrusive than individuals 2 and 3.

If we compare individual 5 (CFE=0.644, mass=17.75kg) with the individual 6 (CFE=0.661, mass=18.55kg), we notice that individual 6 presents an increase of 2.6% in CFE. But this improvement is just achieved by increasing its mass by 4.5%. In addition, individual 5 is less intrusive than individual 6. This leave us with two options, individual 4 or 5. Individual 5 presents an increase of about 4% in the CFE with just increasing its mass by 1.5% in relation to the individual 4. But the major difference between them is the maximum acceleration, individual 5 presents 23% less maximum acceleration than individual 4.

All things considered, the beam 5 is the chosen one. This beam is the individual number 2 of optimization 5. A quadrangular shape beam with the squares misaligned and with the strategy of forcing the first width division to be thicker than the rest of the beam. It is formed by 2 divisions in height, 6 in width, thickness1 with 2mm and thickness2 with 5mm.

Figures 5.21, 5.22, 5.23 and 5.24 were all computed from the performed simulations on the chosen beam. Figure 5.21 shows the static test result, where the displacement in Z direction is measured for all nodes, presenting lower values than 1mm.

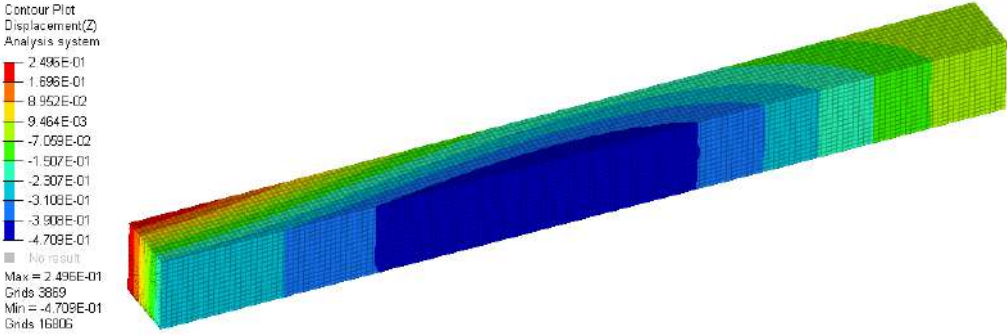


Figure 5.21: Displacements in Z direction - static test.

In figure 5.22 is represented the curve force-displacement with the maximum and average force

evidenced where the proximity between the two forces can be observed. Comparing this curve with figure 2.2 it can be concluded that this curve matches the optimal curve in crashworthiness.

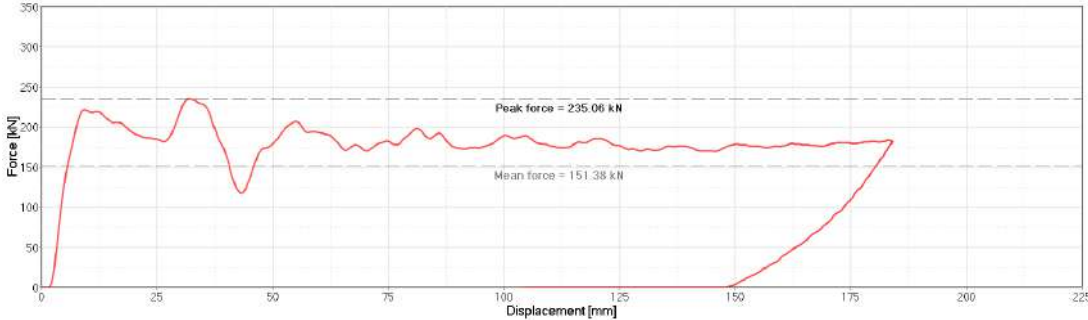


Figure 5.22: Force-displacement curve from the chosen beam.

Figure 5.23 shows the result of the crash pole test evidencing the differences between before and after the collision.

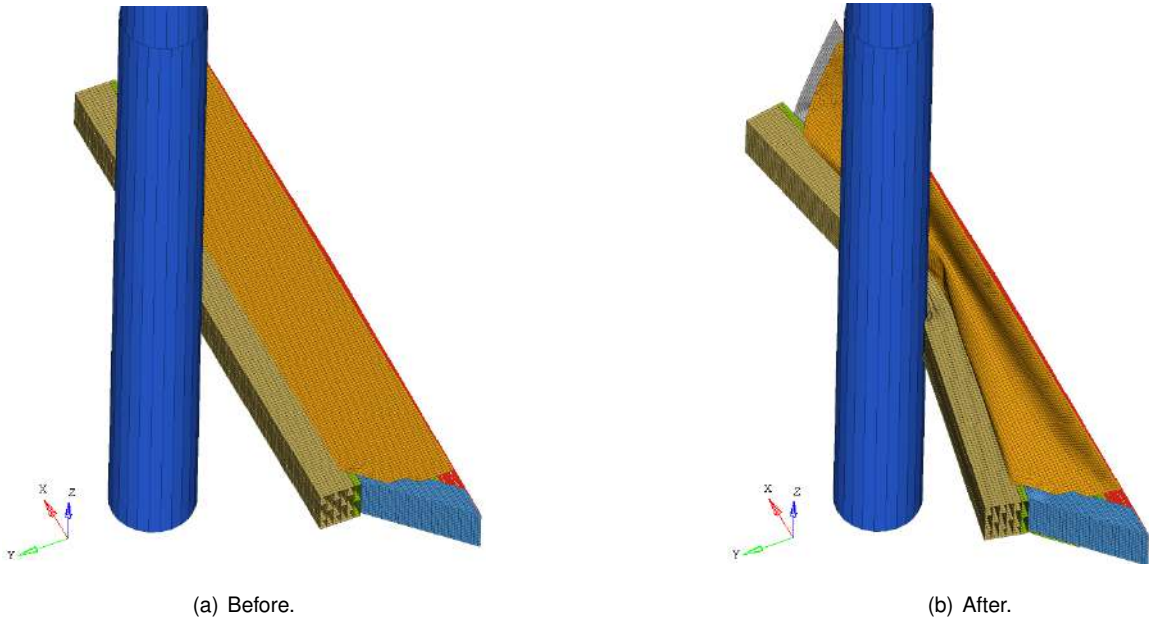


Figure 5.23: Pole test results on the chosen beam.

In figure 5.24 we can observe the beam with the auxiliary components hidden, where the plastic strain in the traction zone is measured, presenting lower values than failure strain.

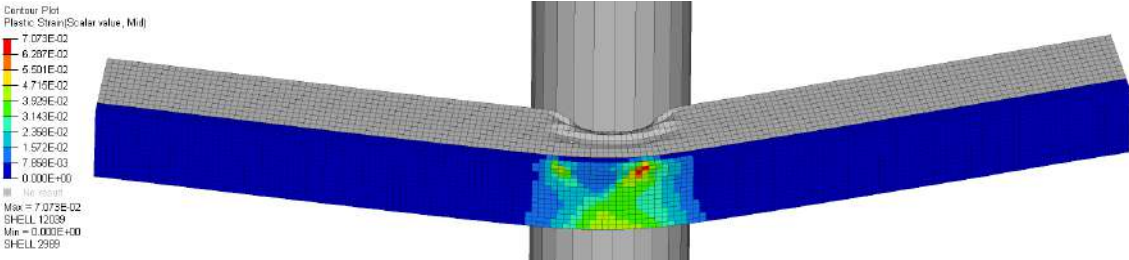


Figure 5.24: Plastic strain with just the beam visible, in its traction zone.

Chapter 6

Conclusions

The main objective of this project was to design a side beam chassis that must fulfill requirements of stiffness and crashworthiness. The work developed was integrated in the Be2.0 project. This is an on-demand vehicle for share use that can be driven by a human operator or autonomously. Powered 100% electric this car will be a M1 class vehicle with Portuguese engineering.

To develop this beam, two robust numerical models were created, inserted in a multi-objective optimization program based on a genetic algorithm. This program searches for the best pole crash performance and the lightest beam, subject to non-linear constraints (HIC_{15} , acceleration, intrusion, torsional deflection, displacement in Z direction and Von Mises equivalent stress.).

This chassis will have new applications such as smaller or larger cars, mini buses or cargo vehicles. For this reason, it was very important to develop a powerful and flexible tool that can easily redesign and recalculate a new beam for other applications. This resizing can be achieved by only changing the input parameters of the optimization cycle such as mass, width, height, material, etc.

In order to add value to this work, and simultaneously to develop an optimized beam for this vehicle, several beam shapes and strategies were implemented. The implementation of quadricular shape beams, with squares aligned or misaligned, as well as the strategy of forcing the first width division to be thicker than the rest of the beam, proved to be a success. The results were obtained with increasingly better crash performance with lighter beams.

All the collected data allow evaluation how the different types of structure behave in the pole test and how the evaluated parameters influence this behavior.

6.1 Deliverables and Achievements

The major deliverables were:

- Multi-objective optimization program based on a genetic algorithm, which automatically returns an optimized beam;
- A versatile optimization program that allows to change the objective functions, dimensions, beam shapes, materials, parameters to optimize and others, was developed;

- Two robust numerical models were build, a non-linear explicit and a linear static;
- A database that allows evaluation of how the different types of beam shapes behave and how the optimized parameters influence this behavior.

The major achievements included:

- An optimized beam for application in Be2.0 that fulfills all project requirements, such as materials, fabrication, dimensions, stiffness and crashworthiness. This design structure meets the initial goals from the Euro NCAP pole test;
- Beams with quadricular aligned and misaligned shapes allowed for lighter structures with better crash performance, than beams only composed by one rectangle;
- The implemented multi-thickness strategy, forcing the first width division to be thicker than the rest of the beam, proved to be beneficial in crash performance;
- The single thickness strategy allowed for lighter beams than the multi-thickness strategy;
- Beams with quadricular misaligned shape allowed for lighter structures and with better crash performance, than beams only composed by a quadricular aligned shape.

6.2 Future Work

A 150mm security distance for the intrusion, between the beam and the batteries, was considered a fixed value for this work because the batteries were already set. However, it would be interesting to study the relation between the increase of vehicle's range, with the decrease of pole crash performance. This assumption is based in the idea that by increasing the size of batteries a higher range, but with less space for intrusion, could be achieved.

Due to the large costs of building a structure like this, validation tests were not possible to be conducted. In future works, these tests could be carried out.

Due to the early stage development of this vehicle, it was not yet possible to carry out a crash test with the car equipped with the proposed side beam chassis. It would be interesting to study how the beam behaves in the car. In that model, it would be possible to put a dummy and to calculate the performance in chest, abdomen, pelvis and head. It would also be possible to verify if the HIC_{15} results are correlated with the ones obtained in this project.

Bibliography

- [1] The Guardian. All Volvo cars to be electric or hybrid from 2019. <https://www.theguardian.com/business/2017/jul/05/volvo-cars-electric-hybrid-2019>. [Accessed February 2018].
- [2] The Guardian. france to ban sales of petrol and diesel cars by 2040. <https://www.theguardian.com/business/2017/jul/06/france-ban-petrol-diesel-cars-2040-emmanuel-macron-volvo>. [Accessed February 2018].
- [3] G. Genta and L. Morello. *The Automotive Chassis*. Springer, 2009.
- [4] M. Gitlin. Lithium side effects and toxicity: prevalence and management strategies. *International Journal of Bipolar Disorders*, 4(1):27, 2016.
- [5] WGLT. Rivian reveals 'skateboard' chassis at michigan conference. <http://www.wglt.org/post/rivian-reveals-skateboard-chassis-michigan-conference#stream/0>. [Accessed September 2018].
- [6] J. N. Reddy. *An Introduction to Finite Element Method*. R.R. Donnelley & Sons Company, 2nd edition, 1993.
- [7] C. Bisagni. Crashworthiness of helicopter subfloor structures. *International Journal of Impact Engineering*, 27(10):1067–1082, 2002.
- [8] P. Xue, M. Ding, C. Qiao, and T. Yu. Crashworthiness study of a civil aircraft fuselage section. *Latin American Journal of Solids and Structures*, 11(9):1615–1627, 2014.
- [9] CEiiA about us. <https://www.ceiia.com/about-us>. [Accessed March 2018].
- [10] European Alternative Fuels Observatory. European vehicle categories. <http://www.eafo.eu/content/european-vehicle-categories>. [Accessed September 2018].
- [11] Drover Rideshare. The tesla gigafactory. <https://www.droverrideshare.com/blog/gigafactory>. [Accessed August 2018].
- [12] Autocar. New Jaguar I-Pace's battery electric vehicle technology at a glance. <https://www.autocar.co.uk/car-news/motor-shows-la-motor-show/new-jaguar-i-pace%E2%80%99s-battery-electric-vehicle-technology-glance>. [Accessed August 2018].

- [13] S. Nikolaevich, A. Valerievich, G. Igorevich, S. Alexandrovich, and S. Alexandrovich. Advanced materials of automobile bodies in volume production. *European Transport*, 10(56):1–27, 2014.
- [14] L. W. Cheah. *Cars on a Diet: The Material and Energy Impacts of Passenger Vehicle Weight Reduction in the U.S.* PhD thesis, Massachusetts Institute of Technology, USA, 2010.
- [15] The Alumium Association. History of aluminum. <http://www.aluminum.org/aluminum-advantage/history-aluminum>. [Accessed March 2018].
- [16] A. Isenstadt, J. German, P. Bubna, M. Wiseman, U. Venkatakrishnan, L. Abbasova, P. Guillen, N. Moroz, D. Richman, and G. Kolwich. Lightweighting technology development and trends in u.s. passenger vehicles. Working Paper, The International Council on Clean Transportation, 2016.
- [17] C. Ungureanu, S. Das, and I. Jawahir. The Minerals, Metals & Materials society. Life-cycle Cost Analysis: Aluminum versus Steel in Passenger Cars, 2007.
- [18] U.S. Department of Energy. Lightweight Materials 2016 Annual Report, 2016.
- [19] D. MacKenzie, S. Zoepf, and J. Heywood. Determinants of u.s. passenger car weight. *The International Journal of Vehicle Design*, 65(1):73–93, 2014.
- [20] S. Macey and G. Wardle. *H-Point: The Fundamentals of Car Design & Packaging*. Art Center College of Design and Design Studio Press, 1nd edition, 2009.
- [21] HYDRO. HS6110 alloy. <https://www.hydroextrusions.com/en-US/why-aluminum/the-material/the-right-alloy/hs6110-alloy/>. [Accessed March 2018].
- [22] European Aluminium Association. Properties and Selection: Nonferrous Alloys and Special-Purpose Materials, 1990.
- [23] ASM International. Aluminum and Aluminum Alloys, 2015.
- [24] A. International. *Metals Handbook - Properties and Selection: Nonferrous Alloys and Special-Purpose Materials*, volume 2. 10nd edition, 1990.
- [25] W. D. Pilkey and D. F. Pilkey. *Peterson's Stress Concentration Factors*. John Wiley & Sons, 3rd edition, 2008.
- [26] J. Happian-Smith. *An Introduction to Modern Vehicle Design*. Butterworth-Heinemann, 1nd edition, 2002.
- [27] A. F. Hughes, D. C. Iles, and A. Malik. *Design of Steel Beams in Torsion*. The Steel Construction Institute, 2011.
- [28] L. Andersen and S. R. Nielsen. Elastic beams in three dimensions. fLecture Notes. Aalborg University, Denmark, 2008.
- [29] P. G. M. Rebelo. Design study of a side intrusion beam for automotive safety. Master's thesis, Instituto Superior Técnico, Portugal, 2016.

- [30] T. Tang, W. Zhang, H. Yin, and H. W. State. Crushing analysis of thin-walled beams with various section geometries under lateral impact. *Thin-Walled Structures journal*, 102:43–57, 2016.
- [31] F. Djameluddin, S. Abdullah, A. K. Ariffin, and Z. M. Nopiah. Multi objective optimization of foam-filled circular tubes for quasi-static and dynamic responses. *Latin American Journal of Solids and Structures*, 12(6):1126–1143, 2014.
- [32] T. M. E. Nunes. Multi-objective design optimization of a frontal crash energy absorption system for a road-safe vehicle. Master's thesis, Instituto Superior Técnico, Portugal, 2017.
- [33] T. Tang, Y. Gao, L. Yao, Y. Li, and Jian. Development of high-performance energy absorption component based on the structural design and nanocrystallization. *Materials and Design*, 137: 214–225, 2018.
- [34] S. Darwish, A. Gemeal, and H. Hussein. Finite element side crash test for first saudi car. *International Journal of Engineering and Innovative Technology*, 3(6):65–66, 2013.
- [35] United Nations Economic Commission for Europe. Concerning the Adoption of Uniform Technical Prescriptions for Wheeled Vehicles, Equipment and Parts which can be Fitted and/or be Used on Wheeled Vehicles and the Conditions for Reciprocal Recognition of Approvals Granted on the Basis of these Prescriptions – Addendum 94: Regulation No.95, 2014.
- [36] European New Car Assessment Programme - Side Pole. <https://www.euroncap.com/en/vehicle-safety/the-ratings-explained/adult-occupant-protection/side-pole/>. [Accessed July 2018].
- [37] European New Car Assessment Programme - Side Pole. Oblique Pole Side Impact Testing Protocol, 2017.
- [38] European New Car Assessment Programme - Side Pole. Euro NCAP Rating Review 2018, 2018.
- [39] European New Car Assessment Programme - Side Pole. Assessment Protocol – Adult Occupant Protection, 2018.
- [40] F. P. Beer, E. R. Johnston, and J. T. Dewolf. *Mechanics of Materials*. McGraw-Hill, 4th edition, 2006.
- [41] M. Grazka, J. Janiszewski, L. Kruszka, E. C. D. Forni, and G. Riganti. Identification methods of parameters for johnson-cook constitutive equation – comparison. *Applied Mechanics and Materials*, 566:97–103, 2014.
- [42] X. Wang and J. Shi. Validation of johnson-cook plasticity and damage model using impact experiment. *International Journal of Impact Engineering*, 60:67–35, 2013.
- [43] U.S. Department of Transportation. Failure Modeling of Titanium 6Al-4V and Aluminum 2024-T3 With the Johnson-Cook Material Model, 2003.

- [44] SEWESoft. Strain measurement. <https://www.dewesoft.com/pro/course/strain-measurement-1>. [Accessed March 2018].
- [45] S. S. D. V. Ganeshan. Converting dynamic impact events to equivalent static loads in vehicle chassis. Master's thesis, Chalmers University of Technology, Sweden, 2017.
- [46] Altair Engineering. Radioss Theory Manual, 2009.
- [47] Altair University. Crash Analysis With RADIOSS - A Study Guide, 2015.
- [48] A. C. Marta. Aircraft optimal design - MSc course notes. Instituto Superior Técnico, Portugal, 2015.
- [49] MathWorks. MathWork help. <https://www.mathworks.com/help>. [Accessed July 2018].
- [50] C. Eksin. Application of genetic algorithms to analysis and policy design in system dynamics. Master's thesis, Istanbul Technical University, Turkey, 2005.
- [51] K. Deb. Multi-objective optimization using evolutionary algorithms: An introduction. Indian Institute of Technology Kanpur, India, 2011.
- [52] B. Placzankis. General corrosion resistance comparisons of medium- and high-strength aluminum alloys for DOD systems using laboratory-based accelerated corrosion methods. Army Research Laboratory, 2009.
- [53] J. Davis, editor. *Corrosion of Aluminum and Aluminum Alloys*. ASM International, 1999.
- [54] S. Semiatin, editor. *ASM Handbook - Metalworking: Bulk Forming*, volume 14A. ASM International, 2005.
- [55] Dassault Systèmes. CATIA. <https://www.3ds.com/products-services/catia/>. [Accessed July 2018].
- [56] Altair Hyperworks. Altair product showcase. <https://altairhyperworks.com/APS.aspx>, . [Accessed July 2018].
- [57] Altair University. some remarks about hourglass. https://altairuniversity.com/learning-library/iv_some-remarks-about-hourglass/, . [Accessed July 2018].
- [58] SAE International. SAE J211-1 (1995): Instrumentation for Impact Test, Part 1, Electronic Instrumentation, Date of Action: 2007.
- [59] S. Seo, D. Sim, and J. Min. The study of side structure optimization of the SUV for new side NCAP tests. Ssangyong Motor Company.
- [60] J. Davis, editor. *Tensile Testing*. ASM International, 2nd edition, 2004.
- [61] V. Infante. Private conversation, Instituto Superior Técnico, Portugal. September 2018.
- [62] MakeitFrom. Material properties database. <https://www.makeitfrom.com/>. [Accessed March 2018].

Appendix A

6xxx Alloy Properties

Table A.1: 6xxx alloy properties [24][62]

Alloy	E [GPa]	E-break [%]	G [GPa]	Shear Yield [MPa]	UTS [MPa]	Tensile Yield [MPa]	Density [g/cm ³]	U Resilience [MJ/m ³]
6005-T5	68	9,5	26	170	290	270	2,7	27
6005-T61	68	12	26	210	310	280	2,7	36
6005-T6	68	11	26	210	300	250	2,7	30
6005A-T5	69	8,6	26	170	290	250	2,7	24
6005A-T6	69	9	26	170	280	230	2,7	24
6005A-T61	69	9,1	26	180	300	270	2,7	26
6008-T6	69	9,1	26	170	290	220	2,7	24
6012-T6	69	9,1	26	190	320	260	2,9	28
6013-T6	69	9,1	26	240	410	350	2,8	36
6013-T651	69	3,4	26	240	410	350	2,8	13
6014-T6	69	9,1	26	150	260	200	2,7	22
6016-T6	69	11	26	170	280	210	2,7	29
6018-T6	69	9	26	170	290	230	2,9	24
6018-T6510	69	9,1	26	180	300	220	2,9	25
6018-T6511	69	9	26	170	290	230	2,9	24
6023-T6	69	11	26	220	360	300	2,8	39
6023-T6510	69	11	26	210	360	310	2,8	38
6023-T6511	69	11	26	220	360	300	2,8	39
6025-H36	70	3,4	26	140	240	210	2,8	7,8
6061-T51	69	7,8	26	160	270	230	2,7	20
6061-T6	69	10	26	210	310	270	2,7	30
6061-T62	69	8,7	26	190	320	270	2,7	26
6061-T651	69	11	26	210	320	270	2,7	33
6061-T6510	69	9,1	26	180	300	270	2,7	26
6061-T6511	69	9	26	170	290	270	2,7	26
6061-T652	69	3,4	26	190	280	250	2,7	9,2
6063-T6	68	11	26	150	240	210	2,7	25
6063-T62	68	9,1	26	150	250	210	2,7	22
6063-T66	68	11	26	150	250	230	2,7	27
6063-T8	68	9	26	150	260	240	2,7	23
6063-T83	68	7,3	26	150	260	240	2,7	18
6063-T832	68	8,2	26	190	300	270	2,7	24
6063A-T6	68	8	26	150	260	200	2,7	19
6065-T6	68	11	26	190	310	270	2,8	34
6065-T8	68	4,6	26	230	390	350	2,8	17
6065-T9	68	4,5	26	230	400	380	2,8	18
6066-T4	70	16	26	200	340	200	2,8	47

6066-T451	70	17	26	200	360	210	2,8	52
6066-T4510	70	13	26	190	310	190	2,8	36
6066-T4511	70	14	26	190	310	190	2,8	37
6066-T6	70	9,5	26	240	390	350	2,8	36
6066-T62	70	7,8	26	230	390	330	2,8	29
6066-T651	70	11	26	240	440	360	2,8	42
6066-T6510	70	7,8	26	230	390	350	2,8	29
6066-T6511	70	8	26	230	390	350	2,8	30
6070-T6	70	8,6	26	240	380	350	2,7	32
6070-T62	70	5,6	26	220	370	350	2,7	20
6081-T6	69	9	26	180	310	270	2,7	27
6082-T5	69	9	26	180	300	260	2,7	26
6082-T6	69	9,8	26	220	330	270	2,7	30
6082-T61	69	9,1	26	190	310	220	2,7	26
6082-T6151	69	9	26	180	310	230	2,7	25
6082-T62	69	7,9	26	180	310	270	2,7	24
6082-T651	69	6,3	26	190	320	270	2,7	19
6082-T6511	69	13	26	220	340	320	2,7	43
6105-T5	68	9	26	170	280	270	2,7	25
6106-T6	69	9,1	26	170	290	220	2,7	24
6110-T9	70	2,2	26	290	500	500	2,8	11
6110A-T4	70	18	26	220	360	250	2,8	58
6110A-T5	70	11	26	250	430	410	2,8	47
6110A-T6	70	11	26	280	470	430	2,8	52
6151-T6	69	5,7	26	200	340	280	2,7	18
6151-T652	69	1,1	26	190	330	270	2,7	3,5
6162-T5	68	6,8	26	170	290	260	2,7	19
6162-T5510	68	6,7	26	170	290	270	2,7	19
6162-T5511	68	6,8	26	170	290	260	2,7	19
6162-T6	68	9	26	170	290	270	2,7	26
6162-T6510	68	9,1	26	180	300	270	2,7	26
6162-T6511	68	9	26	170	290	270	2,7	26
6182-T6	70	6,8	26	190	320	270	2,7	21
6261-T5	69	9,1	26	170	290	240	2,7	24
6261-T6	69	9	26	180	300	260	2,7	26
6262-T6	68	10	26	190	320	270	2,8	31
6262-T62	68	9	26	190	320	270	2,8	28
6262-T651	68	10	26	190	320	270	2,8	31
6262-T6510	68	10	26	170	290	270	2,8	29
6262-T6511	68	10	26	180	300	270	2,8	29
6262-T8	68	4,6	26	230	390	350	2,8	17
6262-T9	68	5	26	240	390	360	2,8	19
6262A-T6	68	11	26	190	310	270	2,8	34
6262A-T8	68	4,5	26	220	390	360	2,8	17
6262A-T9	68	4,6	26	240	410	370	2,8	18
6351-T5	69	9,1	26	180	300	260	2,7	26
6351-T6	69	11	26	200	310	270	2,7	33
6463-T6	68	11	26	150	230	200	2,7	25

Appendix B

Initial Populations

Table B.1: Initial population for optimization 2

Individual	Height Divisions	Width Divisions	Thickness [mm]
1	2	2	1
2	2	3	4
3	3	2	4
4	7	4	2
5	4	7	2
6	3	3	4
7	9	9	1
8	7	3	2
9	5	2	3

Table B.2: Initial population for optimization 3

Individual	Height Divisions	Width Divisions	Thickness [mm]
1	2	2	1
2	2	4	3
3	2	2	4
4	7	3	2
5	3	3	3
6	9	9	1
7	4	3	3
8	5	2	3
9	5	6	2

Table B.3: Initial population for optimization 4

Individual	Height Divisions	Width Divisions	Thickness1 [mm]	Thickness2 [mm]
1	2	2	1	4
2	2	4	2	7
3	4	3	2	6
4	7	3	2	5
5	2	7	2	6
6	3	3	3	4
7	3	4	2	7
8	5	2	3	5
9	5	4	1	9

Table B.4: Initial population for optimization 5

Individual	Height Divisions	Width Divisions	Thickness1 [mm]	Thickness2 [mm]
1	2	2	1	4
2	2	4	2	6
3	7	3	2	4
4	2	7	2	6
5	3	3	3	4
6	9	9	1	8
7	4	3	2	6
8	5	2	3	5
9	5	6	1	4

Appendix C

CAD Drawings

1 2 3 4

A

A

B

B

C

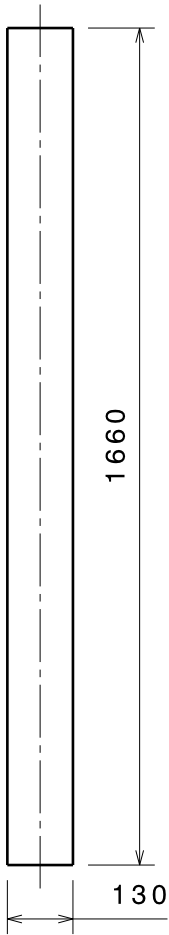
C

D

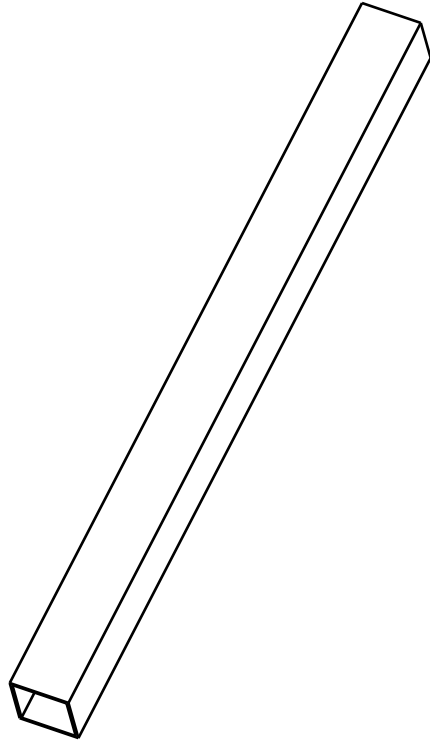
D

E

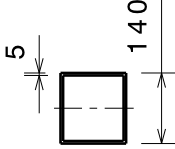
E



Front view



Isometric view



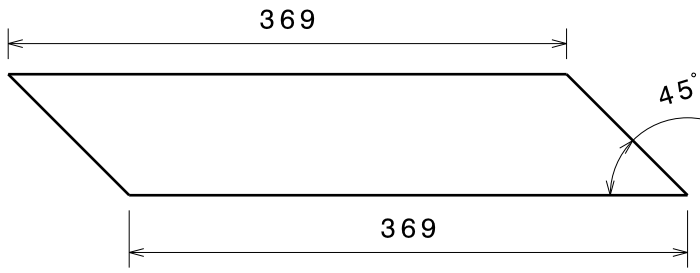
Top view

Notes:

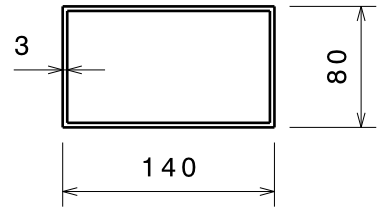
Manufacturing: Extrusion
Quantity: x1

DIM.	ISO 2768 mK	Roughness:		Shape:	ISO E
Material:	Al 6110A-T6			Scale:	1:15
Project: Master Thesis					
Catia V5 R20		Date	Name	Title: Beam	
	Drawn	27/9/2018	Pereira	Part-No.:	
	Checked	27/9/2018	-	-	
	Approved	27/9/2018	-		
www.Ceiiia.com	2D Version	A0101	Released	27/9/2016	Sheet Size A4 Pag. 1 / 1

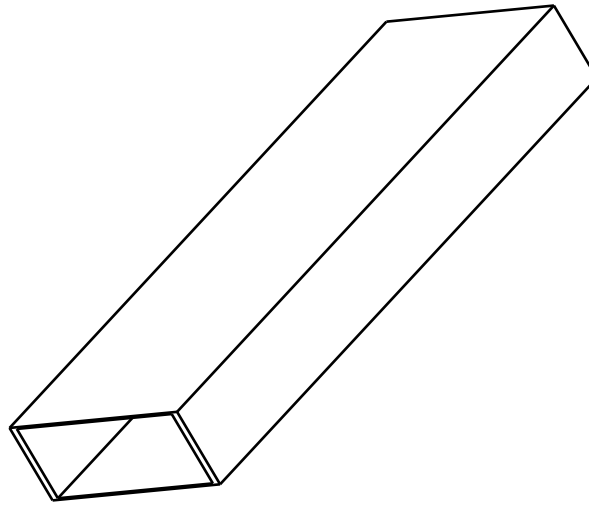
1 2 3 4



Front view



Left view

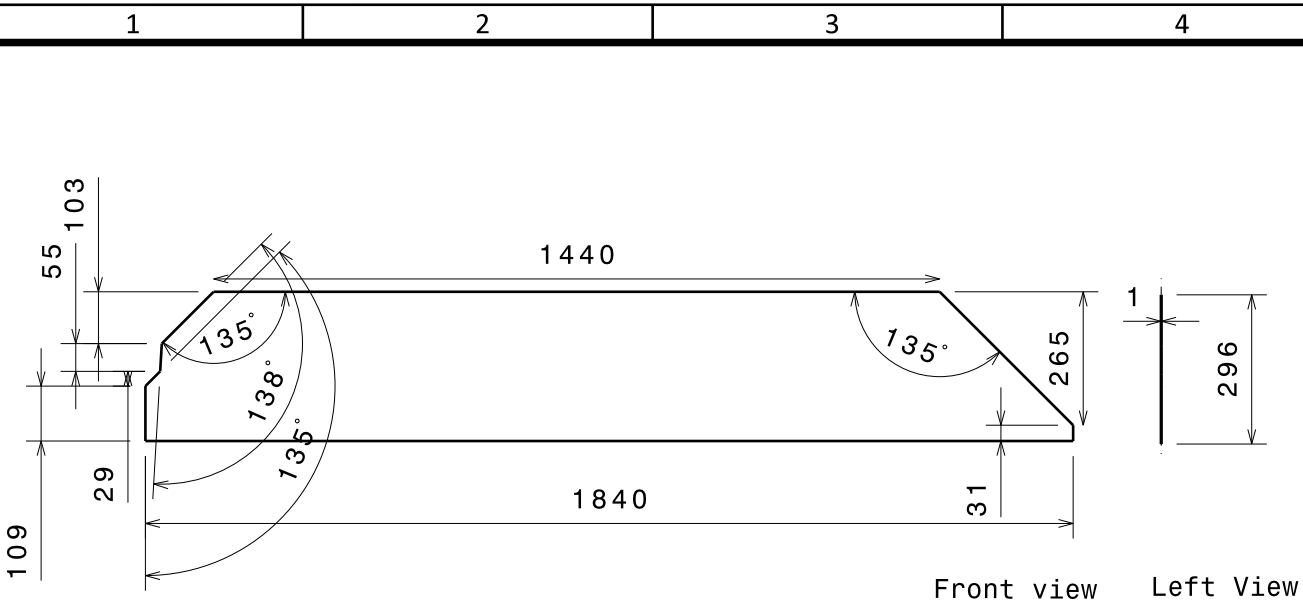


Isometric view

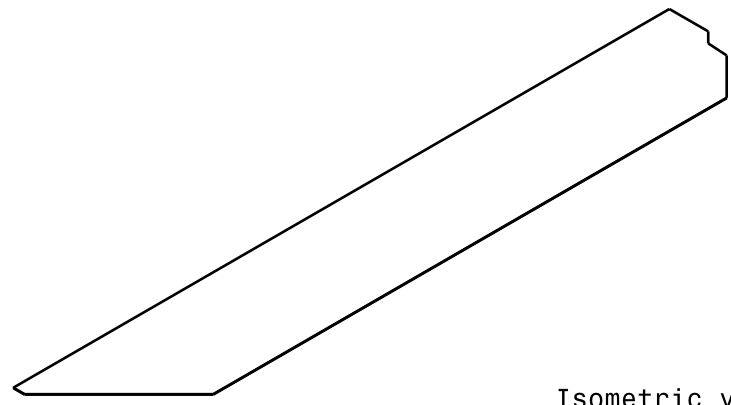
Notes:

Manufacturing: Extrusion
Quantity: x2

DIM.	ISO 2768 mK	Roughness:		Shape:	ISO E
Material:	Al 6061-T6			Scale:	1:5
Project: Master Thesis					
Catia V5 R20		Date	Name	Title: Support	
 PUSHING MOBILITY. www.CeiiA.com	Drawn	27/9/2018	Pereira	Part-No.:	
	Checked	27/9/2018	-	-	
	Approved	27/9/2018	-	-	
2D Version	A0101	Released	27/9/2016	Sheet Size	A4 Pag. 1 / 1



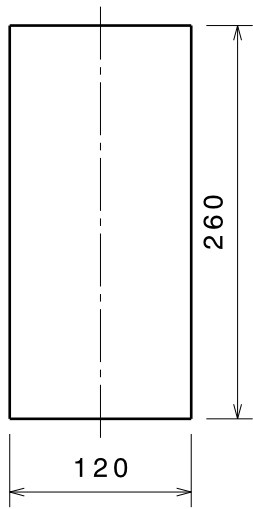
Front view Left View



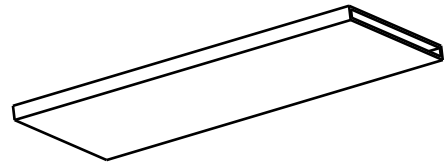
Isometric view

Notes: Manufacturing: Rolled
Quantity: x1

DIM.	ISO 2768 mK	Roughness:		Shape:	ISO E
Material:	Al 6061-T6				Scale: 1:15
Project: Master Thesis					
Catia V5 R20		Date	Name	Title: Floor	
	Drawn	27/9/2018	Pereira	Part-No.:	
	Checked	27/9/2018	-	-	
	Approved	27/9/2018	-	-	
www.CeiiA.com	2D Version	A0101	Released	27/9/2016	Sheet Size A4 Pag. 1 / 1



Bottom view



Isometric view

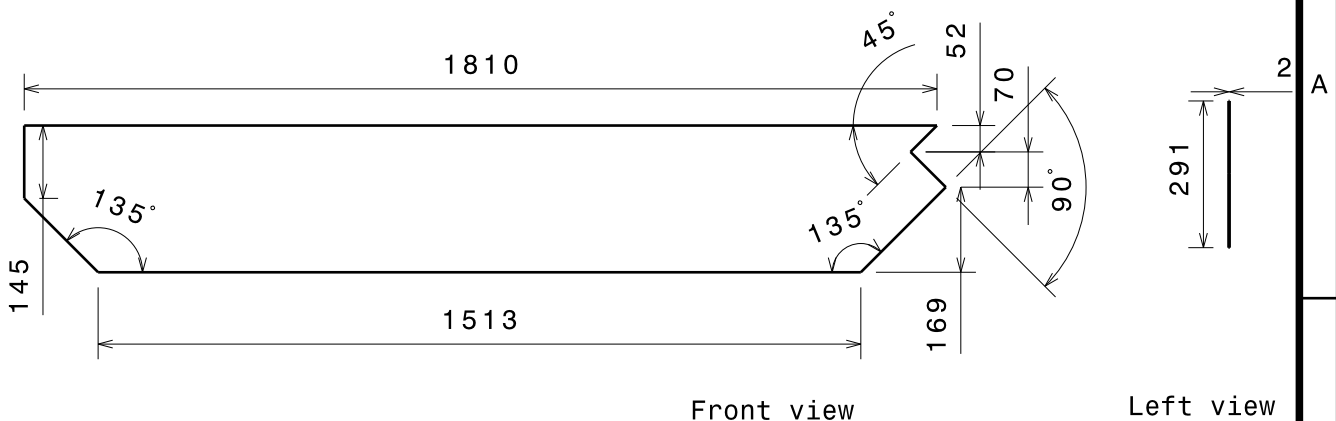


Front view

Notes:

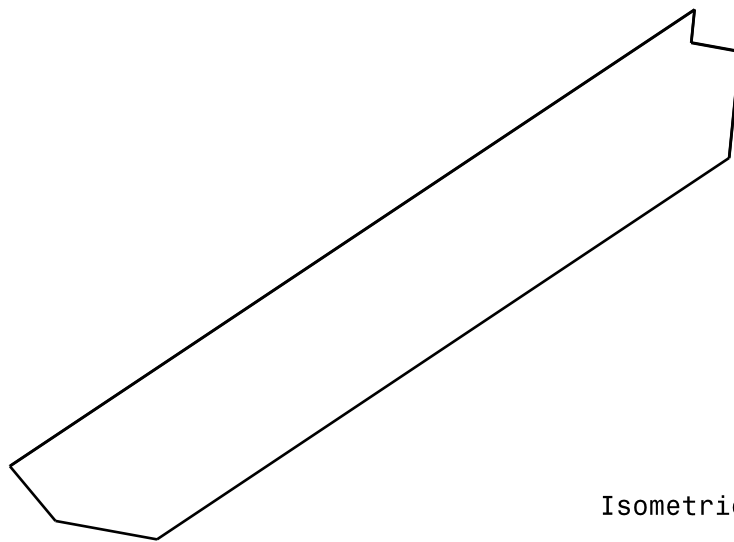
Manufacturing: Extrusion
Quantity: x3

DIM.	ISO 2768 mK	Roughness:		Shape:	ISO E
Material:	Al 6061-T6			Scale:	1:5
Project: Master Thesis					
Catia V5 R20		Date	Name	Title: Floor support	
 PUSHING MOBILITY. www.CeiiA.com	Drawn	27/9/2018	Pereira	Part-No.:	
	Checked	27/9/2018	-	-	
	Approved	27/9/2018	-	-	
2D Version	A0101	Released	27/9/2016	Sheet Size	A4 Pag. 1 / 1



Front view

Left view



Isometric view

Notes:

Manufacturing: Rolled
Quantity: x1

DIM.	ISO 2768 mK	Roughness:		Shape:	ISO E
Material:	Al 6061-T6			Scale:	1:15
Project: Master Thesis					
Catia V5 R20		Date	Name	Title: Undershield	
	Drawn	27/9/2018	Pereira	Part-No.:	
	Checked	27/9/2018	-	-	
	Approved	27/9/2018	-	-	
www.CeiiA.com	2D Version	A0101	Released	27/9/2016	Sheet Size A4 Pag. 1 / 1

1

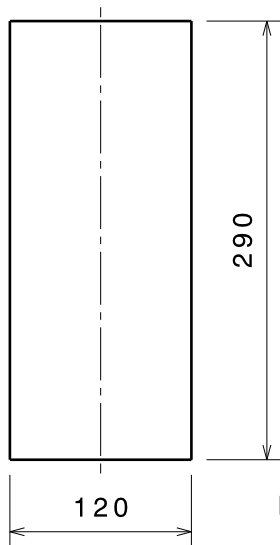
2

3

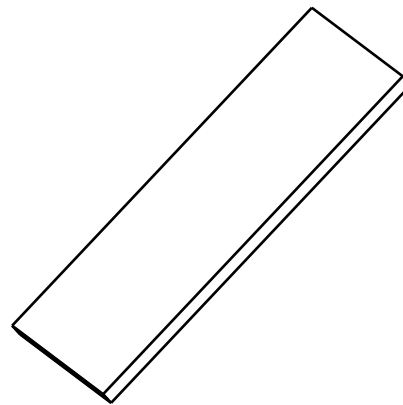
4

A

A



Front view



Isometric view

B

B

C

C



Top view

D

D

Notes:

Manufacturing: Extrusion
 Quantity: x3

DIM.	ISO 2768 mK	Roughness:		Shape:	ISO E
Material:	Al 6061-T6			Scale:	1:5
Project: Master Thesis					
Catia V5 R20		Date	Name	Title: Undershield support	
 PUSHING MOBILITY. www.CeiiA.com	Drawn	27/9/2018	Pereira	Part-No.:	
	Checked	27/9/2018	-	-	
	Approved	27/9/2018	-		
2D Version	A0101	Released	27/9/2016	Sheet Size	A4 Pag. 1 / 1

E

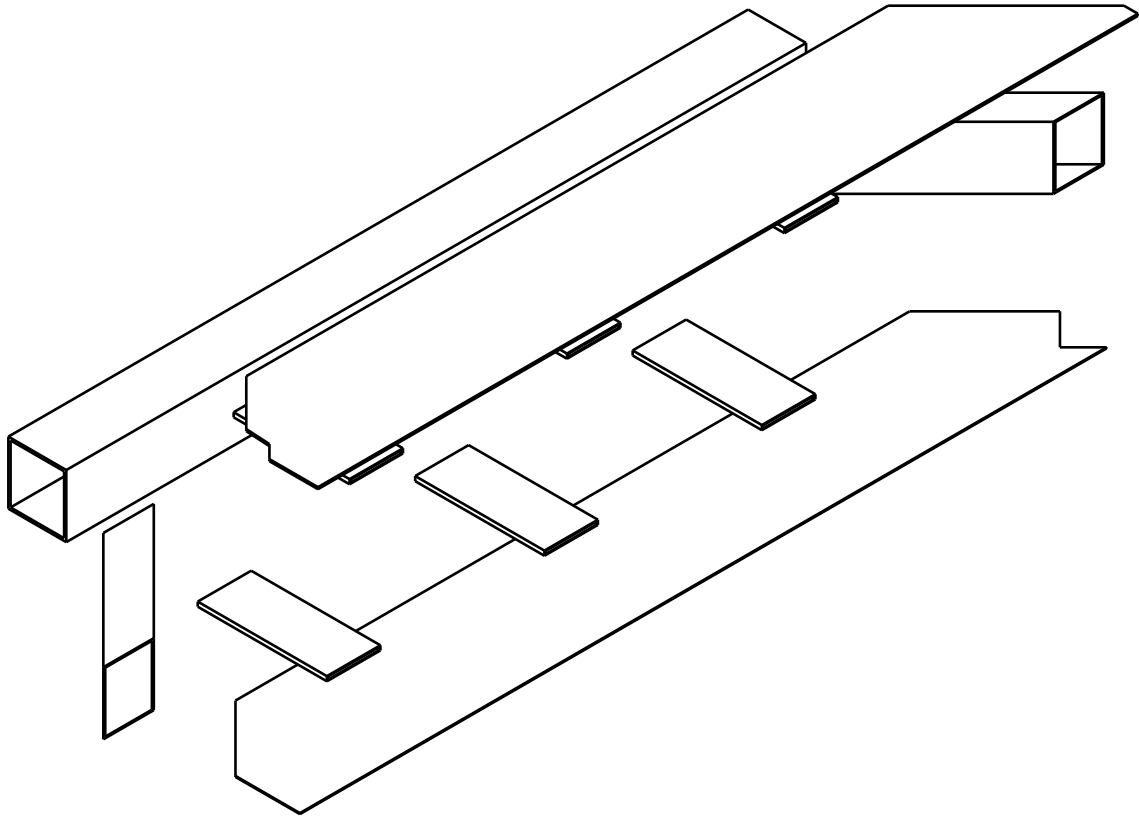
E

1

2

3

4



Expanded view

Notes:

Manufacturing: -
Quantity: x1

DIM.	ISO 2768 mK	Roughness:		Shape:	ISO E
Material:	-				Scale: 1:12
Project: Master Thesis					
Catia V5 R20		Date	Name	Title: Structure	
 PUSHING MOBILITY. www.CeiiA.com	Drawn	27/9/2018	Pereira	Part-No.:	
	Checked	27/9/2018	-	-	
	Approved	27/9/2018	-	-	
www.CeiiA.com	2D Version	A0101	Released	27/9/2016	Sheet Size A4 Pag. 1 / 1